PRECISION ENGINEERING CENTER

2010 ANNUAL REPORT
VOLUME XXVIII
March 2011

Sponsors:	Lockheed Martin Corporation
	Minnesota Mining & Manufacturing Company (3M)
	National Institutes of Health (NIH)
	National Science Foundation (NSF)
	Strategic Research Initiatives (NCSU)
	Vistakon, Division of Johnson & Johnson Vision Care, Inc.
Faculty:	Thomas Dow
	Ronald Scattergood
	David Muddiman
	Jeff Eischen
	Dave Hinks
	Keith Beck
Graduate Students:	Brandon Lane Guillaume Robichaud
	Erik Zdanowicz Zachary Marston
Undergraduate Students:	Darrell LaBarbera Neil VonHolle
Staff:	Kenneth Garrard
	Alexander Sohn
	Monica Ramanath
Consultants:	Karl J. Falter
	Amir Pirzadeh, Tisfoon Ulterior Systems
	Andy Fanning, Fanning Technical Services
	Robert Smythe, R. A. Smythe, LLC

Table of Contents

SUMMARY

The goals of the Precision Engineering Center are: 1) to develop new technology in the areas of precision metrology, actuation, manufacturing and assembly; and 2) to train a new generation of engineers and scientists with the background and experience to transfer this technology to industry. Because the problems related to precision engineering originate from a variety of sources, significant progress can only be achieved by applying a multidisciplinary approach; one in which the faculty, students, staff and sponsors work together to identify important research issues and find the optimum solutions. Such an environment has been created and nurtured at the PEC for 29 years and the 100+ graduates attest to the quality of the results.

The 2010 Annual Report summarizes the progress over the past year by the faculty, students and staff in the Precision Engineering Center. During the past year, this group included 3 faculty, 7 graduate students, 2 undergraduate students, 2 full-time technical staff members and 1 administrative staff member. This diverse group of scientists and engineers provides a wealth of experience to address precision engineering problems. The format of this Annual Report separates the research effort into individual projects but there is significant interaction that occurs among the faculty, staff and students. Weekly seminars by the students and faculty provide information exchange and feedback as well as practice in technical presentations. Teamwork and group interactions are a hallmark of research at the PEC and this contributes to both the quality of the results as well as the education of the graduates.

A brief abstract follows for each of the projects and the details of the progress in each is described in the remainder of the report.

1. **Polaris 3D Development**
   The development of the Polaris 3D, a non-contacting spherical coordinate system measuring machine, has continued with further improvements in probing and error correction. A new chromatic aberration optical probe using an LED light source with adjustable intensity output has provided more flexibility to measure a wider variety of surface materials while improving signal-to-noise ratio. New techniques for compensating for spindle radial error motion and alignment errors between the part and measurement spindle are discussed. .

2. **Measuring Transparent Surfaces with Polaris 3D**
   Techniques for measuring transparent surfaces have been explored on Polaris 3D. The low reflectivity of such surfaces presents unique challenges for finding the surface, but with advanced optical probe hardware and new techniques, accurate measurement of glass, acrylic, and other transparent surfaces are possible. In addition to measuring the shape of the

first surface, thickness measurement looking through to the second surface was explored. While such a measurement is possible, details related to the index of refraction and surface shape introduce difficulties that will make implementation very difficult. The solution that solves the issue is to flip the part over and measure the other side.

3. **Flora II Upgrades and Performance Testing**
The Fast Long Range Actuator (FLORA II) was developed to machine non-rotationally symmetric surfaces on a ultra-precision lathe with a diamond tool. FLORA was designed to have a much longer range than piezoelectric based fast tool servos and significantly higher bandwidth than a slow slide servo. Excellent actuator performance was previously demonstrated, but the user interface needed a major overhaul to improve its efficacy. For this reason, the actuator and its controls have been upgraded and improved and FLORA II is now fully integrated into the diamond turning machine. Specifically, the safety circuits, control system and user interface have been re-engineered and software has been added to translate a surface shape into the motion program needed to machine that surface.

4. **Integrated Prescan Optics for Laser Printers**
An integrated two-element reflective optical system for a laser prescan unit has been designed and fabricated. The optical system was machined from a single piece eliminating the need for assembly and alignment of the two mirrors. However, in their correct orientation in the optical system, neither mirror is rotationally symmetric about any axis. The FLORA II fast tool servo in conjunction with an ultra-precision DTM was used to create the mirror surfaces. Matlab software was developed to decompose a multi-element optical system into a best fit asphere (followed by the DTM) and a non-rotationally symmetric surface (followed by the FLORA II). The shape of the resulting surfaces as measured with the Polaris 3D is presented.

5. **Development of an Air Amplifier as a Focusing Device for Electrospray Ionization Mass Spectrometry**
Mass spectrometry (MS) is an analytical method used to identify molecules and complex proteins based on their mass-to-charge ratio. It is extensively used in analytical chemistry, cancer research, drug testing, explosive detection, etc. However, to be measured, molecules first must be transferred into gas phase and ionized. Electrospray ionization is the dominant technique currently used but only about 1% of ions generated will be measured by the mass spectrometer. This is mainly due to the loss of ions between electrospray source and the instrument inlet due to their charge repulsion and the lack of a focusing method. This NIH funded project is a joint effort combining precision machining and computational fluid dynamics, an aerodynamic focusing device has been designed, fabricated and demonstrated.

6. Effects of Varying EVAM Parameters on Chemical Tool Wear

Reported benefits of applying micrometer-scale vibration to a diamond tool during precision diamond turning (DT) include a decrease in machining forces and wear of the diamond tool. Despite two decades of elliptical vibration-assisted machining (EVAM) research, few have addressed the details and reason for the reduced tool wear. A chemical tool wear model is presented to relate conventional DT tool wear to machining temperatures estimated from finite element models (FEM). This wear model is then applied to FE simulations of EVAM for different workpiece velocities, frequencies, and ellipse shapes. EVAM experiments varying frequency were then conducted and surface finish and tool wear were measured. Optical surface finish was achieved machining low carbon steel but tool edge measurements did not collaborate the reduced wear expected.

7. Visualization of Chip Shape and Machining Forces

The goal is this project was simultaneously measurement of cutting forces and chip shape during diamond turning of aluminum and steel workpieces. Measuring these two parameters have been done separately by a number of investigators, but performing them simultaneously will provide increased understanding of the chip pickup problem. Chip pickup occurs during machining of steel when the workpiece material becomes attached to the cutting tool resulting in higher tool forces and poor surface finish. Cutting and thrust forces were measured using a 3-axis load cell and video images of the chip through a microscope were recorded with depths ranging from from 7 to 25 μm. The chip images had sufficient visual clarity to see the chip formation and relate it to the forces measured.

8. Ultrasonic Vibration Assisted Machining

An ultrasonic elliptical vibration assisted machining (EVAM) device operating at 25 KHz was designed and tested by a summer undergraduate student funded by NSF. This device utilized a piezoelectric resonator called a sonotrode coupled to a parabolic horn to drive the diamond tool in an elliptical path. The resonant frequency and vibrational tool path was determined using finite element modeling and corroborated using an infrared displacement sensor. The device was used to machine 6061-T6 aluminum and C360 brass workpieces. The compliant mounting of the sonotrode and issues related to tool motion direction resulted in poor surface finish. However, the effort indicated the suitability of this type of actuator to increase the speed of the EVAM experiments above the 1-4 KHz range of the Ultramill.

9. Nanocoining of Optical Features

The goal of this research is to create surfaces with features smaller than the wavelength of light using a process called nanocoining. Nanocoining uses a nanostructured diamond die to imprint sub-micrometer features onto the surface of a mold. Because the die is small and the desired size of the mold is large, it must be done at very high speed – on the order of 50 KHz.

iii

The physical process of the nano-indentation is being investigated to understand how materials behave at the nano-scale and how multiple indentations will influence each other. A functional system will be produced by creating experimental indents at slow speed and comparing them to FEA results while simultaneously designing a resonant structure capable of achieving the required displacements at ultrasonic speeds. The ultrasonic actuator along with the ability to create nanostructured features are the key elements to producing optical quality surfaces efficiently.

1 POLARIS 3D DEVELOPMENT

Alex Sohn
Research Assistant
Kenneth P. Garrard
Senior Research Associate
Precision Engineering Center

The capabilities of Polaris 3D continue to be expanded. Further improvements in probing and error correction are described. A new probe using an LED light source with adjustable intensity output has provided more flexibility to probe a wider variety of surfaces while improving signal-to-noise ratio. New techniques that compensate for spindle radial error motion and spindle misalignment have also been implemented.
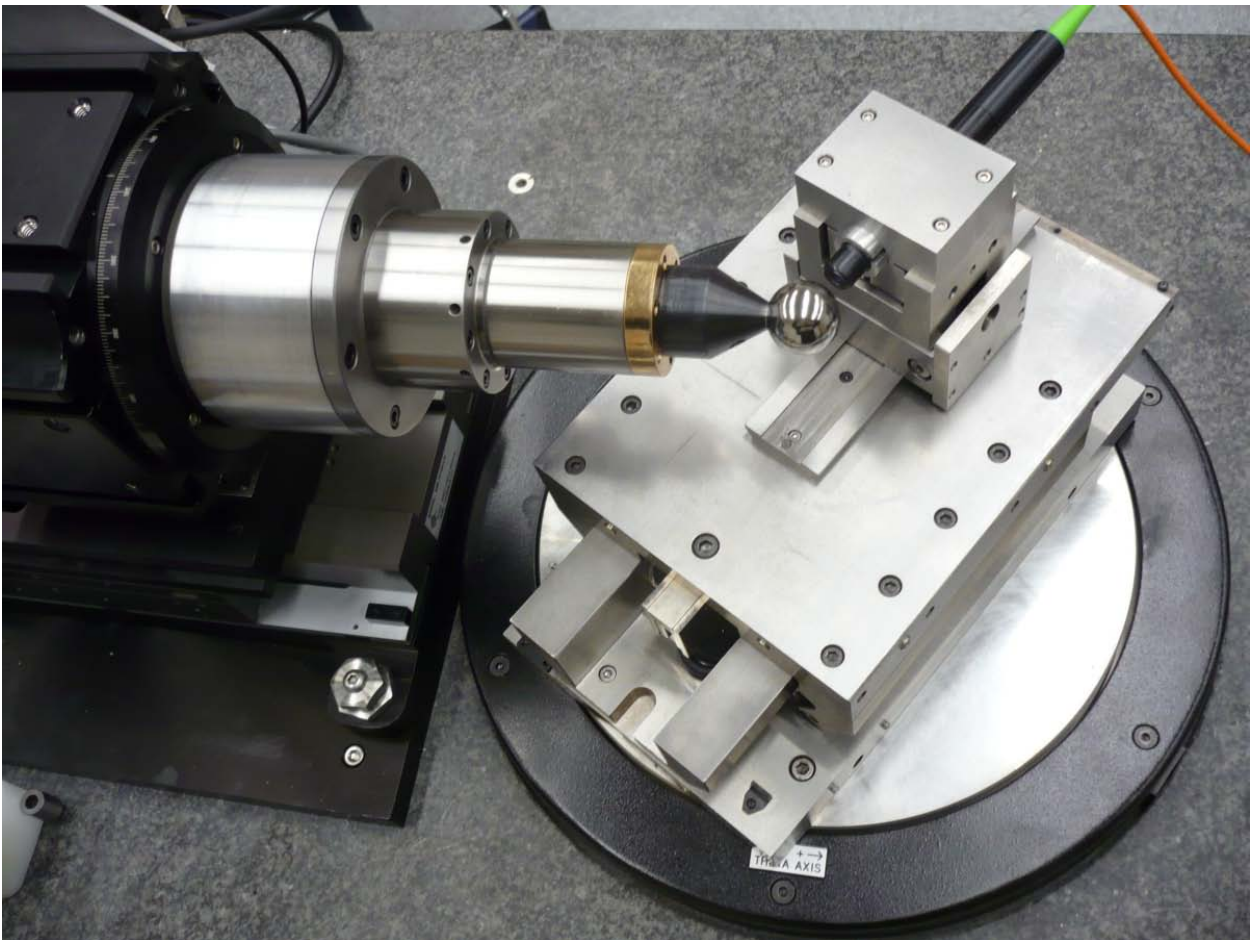
1.1 INTRODUCTION

The profilometer Polaris 3D measures curved surfaces in a spherical coordinate system. It was first developed as a 2D measuring machine with a contacting probe but over the past 2 years has been upgraded to measure 3D surfaces with non-contacting optical probe. The profilometer has a pair of axes that sweep the optical probe over the surface and a second set to position and rotate the part. Errors for each slide and spindle have been measured and compensation algorithms developed. Alignment techniques have also been developed to establish the origin of each axis with respect to the other axes. These algorithms for compensation of repeatable error motions and misalignment of axes were previously developed [1] but have now been improved and implemented in either the controller or the post-measurement data analysis software.

1.2 PROBE EVALUATION

A new Chromatic Aberration (CA) system (CHRocodile S) was loaned to the PEC by Precitec for evaluation. It used a LED light source and came with optical pens that have 300 µm and 600 µm range. They were tested along with the Stil CHR150-N CA system with a 300 µm range pen and a halogen light source owned by the PEC. A 300 µm range CHR 150-N has since been purchased by the PEC and has replaced the Stil system.

1.2.1 ANGLE OF INCIDENCE DEPENDENCE

All of the probes had some variation in distance measurement as a function of angle of incidence. The test for this error involves the use of a 12.7 mm diameter brass diamond turned flat with a flatness of 250 nm (PV). Once the probe has been aligned, the test flat is moved 50 µm from the origin with the R axis and the rotary table (θ axis) is rotated. Rotation produces a displacement, ρ, according to Equation (1).

$$\rho = 0.05 \left(\frac{1}{\cos \theta} \right) \tag{1}$$

With probe tracking disabled, data is collected while θ is rotated. The difference between the measured probe displacement and the displacement calculated from Equation (1) gives the measurement error as shown in Figure 1.
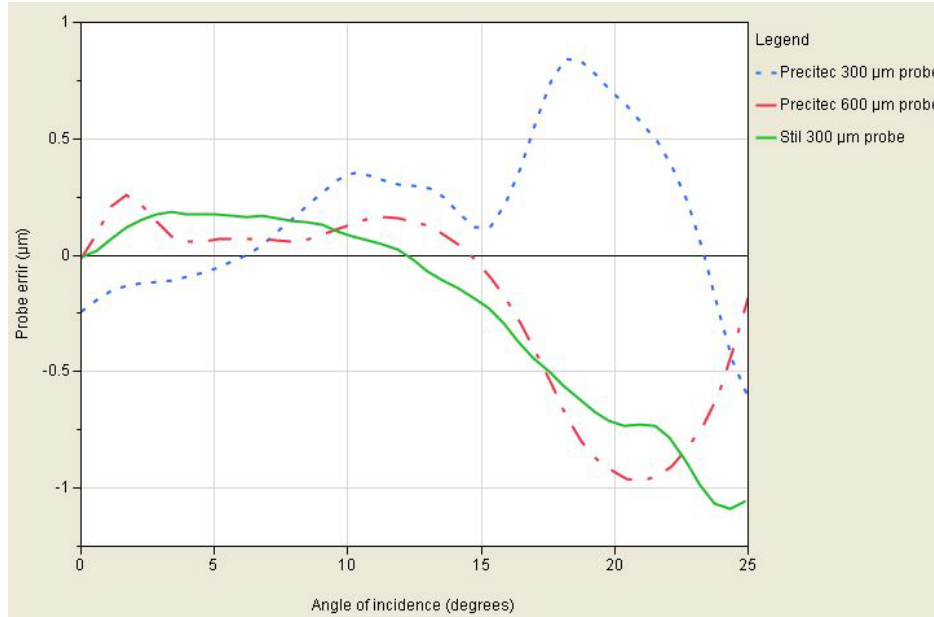
Figure 1. Measurement error for three probes vs. angle of incidence.

This error not only impacts measurements when the angle of incidence is significant, but also has an impact on the original probe alignment method [2]. This discovery has been the main motivation behind the improved probe alignment method (see Section 1.3.2) using a spherical artifact instead of a reference flat.

1.2.2 PROBE NOISE

Data was collected at 1.1 kHz for six seconds for each probe while incident on a brass flat with probe tracking disabled. RMS noise measurements from this test are shown in Table 1 for two probe manufacturers (Precitec and Stil) and two probe ranges (0-300 µm and 0-600 µm). The measurements reveal a substantially lower noise level for the Precitec probes that use an LED source.

Table 1. CA Probe Noise

Probe	Precitec CHRocodile S 600 µm range	Precitec CHRocodile S 300 µm range	Stil CHR150-N 300 µm range
RMS noise (nm)	27	24	66

Proprietary Release subject to the terms and conditions of the Precision Engineering Center Membership Agreement and North Carolina State University Office of Technology Transfer nondisclosure agreements.

1.3 ERROR COMPENSATION

1.3.1 RADIAL ERROR COMPENSATION OF THE SPINDLE

While specified to be less than ±100 nm at the spindle face, the combination of a large measurement offset from this face and a significant tilt error of the part spindle (φ axis) result in error motions in excess of 1 µm at the part location. The greatest impact of these radial error motions is in the x (horizontal) direction of the machine. This x-error ($e_{\varphi x}$), as measured by a capacitance gauge on a precision steel ball is shown in Figure 2 (left) along with a best fit 6th order Fourier series. The curve fit is used to implement the compensation. The residual from this curve fit is shown in Figure 3 (right) and fits the error to ± 150 nm.
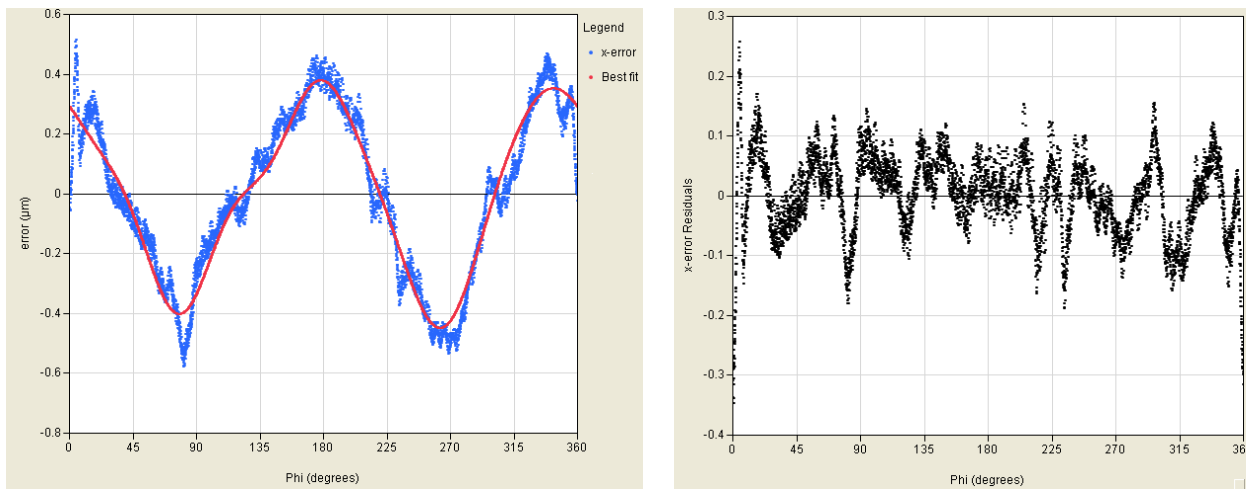

Figure 2. Radial error motion in the x direction of more than 1 µm with a best-fit Fourier series (left) and residual x-direction radial error after compensation (right)

Radial error motion is compensated by modifying R axis measured values as a function of the best-fit Fourier series and the rotary table angle (θ) using Equation (2).

$$e_{\varphi R} = e_{\varphi x} \sin \theta \qquad (2)$$

Equation (2) is subtracted from the each recorded R axis position to compensate for the radial error motion of the part spindle.

1.3.2 PROBE ALIGNMENT

Alignment of the optical probe with the R axis and rotary table (θ) is critical to the analysis of a measurement. The goal is to have the probe zero exactly at the origin of the polar coordinate

system formed by this linear and rotary axis pair. However perfect alignment is not necessary as the misalignment can be compensated in the analysis if the offset is known. A technique for measuring this misalignment with a reference flat was developed for the 2D Polaris machine [3] and further improvements were made for Polaris 3D [4]. However in light of angular probe dependence discussed above, a more robust technique has been developed.

The technique developed for the 2D system made use of the relationship between a radial (i.e., R direction) offset, angle, and observed displacement as given in Equation (1). The sensitivity of the so-called ρ error to probe noise and the angular dependence discussed limit the technique of using a reference flat. Instead a reference sphere is used to directly compare the R direction offset with the sphere radius. This could be done by taking two data points on opposite sides of the sphere and thus directly measuring the diameter of the artifact. A better technique is to measure the rotating sphere through 180° degrees of motion of the θ axis and perform a least squares fit to the result. The difference between the best fit radius and the known sphere size is the alignment offset. Note that the "reversal" technique for eliminating artifact errors is inherent in the data when measuring from equator to pole to equator as the sphere rotates. Therefore, this runout of the part on the spindle and any horizontal misalignment of the two rotating axes are canceled.

1.3.3 HORIZONTAL ALIGNMENT OF THE ROTARY AXES

The two rotating axes (φ and θ) must intersect at a right angle for the Polaris machine to form a true spherical coordinate system. However a small error can be compensated in the analysis code if the error can be accurately measured. When measuring a sphere on one side, say the pole toward the equator at +90°, a horizontal offset will make the sphere appear too small if the offset is positive and too large if it is negative. At the equator, the discrepancy in the radius seen by the probe of a known sphere or cylinder is proportional to the horizontal alignment offset. So this error can also be determined from two runout measurements of a spherical artifact (or cylinder) from rotary table orientations 180 degrees apart. The φ-θ alignment error is then given by Equation (3), where r_{+90} and r_{-90} are the two best fit radii determined from the runout measurements that were generated in the new technique for probe alignment discussed above.

$$e_{\varphi\theta} = \frac{r_{+90}}{2} - \frac{r_{-90}}{2} \tag{3}$$

Compensation for this error in subsequent measurements is done with new values for radial (R') position and angular position (θ') as shown in Equations (4) and (5).

$$R' = \sqrt{R^2 + e_{\varphi\theta}{}^2 - 2e_{\varphi\theta}r\cos\left(\theta + \frac{\pi}{2}\right)} \tag{4}$$

5

$$\theta' = \frac{R^2 - R'^2 - e_{\varphi\theta}^2}{-2e_{\varphi\theta}R'} \qquad (5)$$

1.4 RESULTS

Updates to the error measurement and compensation techniques for correcting φ axis radial spindle error motions and spindle axis misalignment on Polaris 3D have been completed to create accurate and repeatable measurements of a variety of surfaces with the CA optical probes. Figures 3 and 4 show measurement residuals for a 12.7 mm radius sphere measured over a small aperture (10 mm diameter) with and without error compensation. Figures 5 and 6 show the measurement residual for a 22 mm diameter measurement aperture of the same sphere. In both cases the best fit radius is within 300 nm of the accepted value of 12.7 mm which has an uncertainty of ±500 nm.
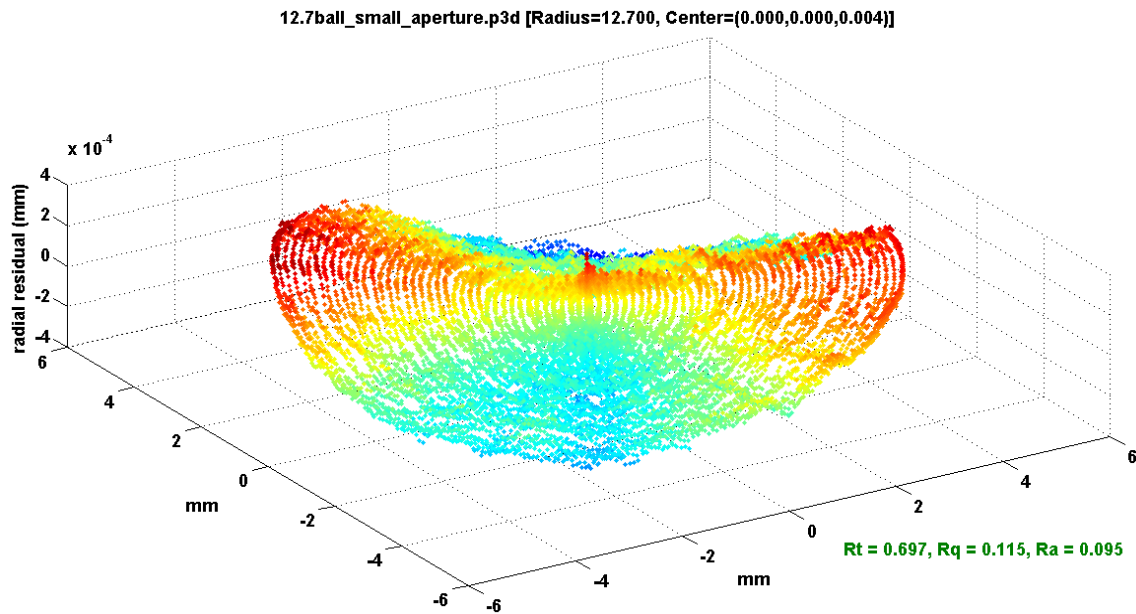

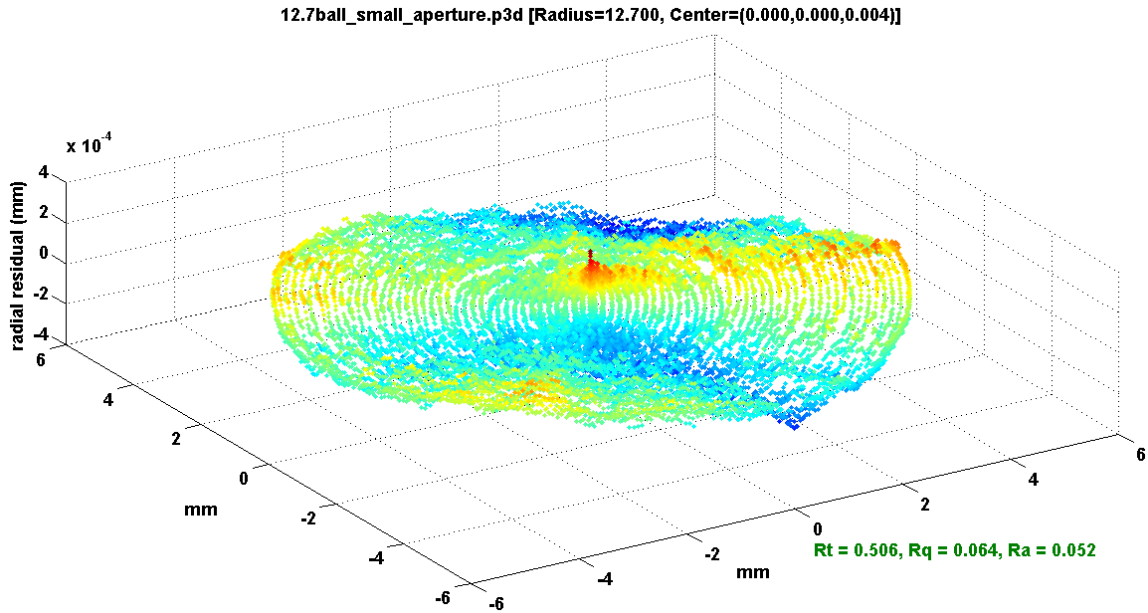**Figure 3.** 12.7 mm ball measured over a 10 mm aperture diameter without error compensation.

12.7ball_small_aperture.p3d [Radius=12.700, Center=(0.000,0.000,0.004)]

Rt = 0.506, Rq = 0.064, Ra = 0.052

Figure 4. 12.7 mm ball measured over a 10 mm aperture diameter with error compensation.

12.7ball_large_aperture.p3d [Radius=12.700, Center=(-0.000,0.000,0.004)]

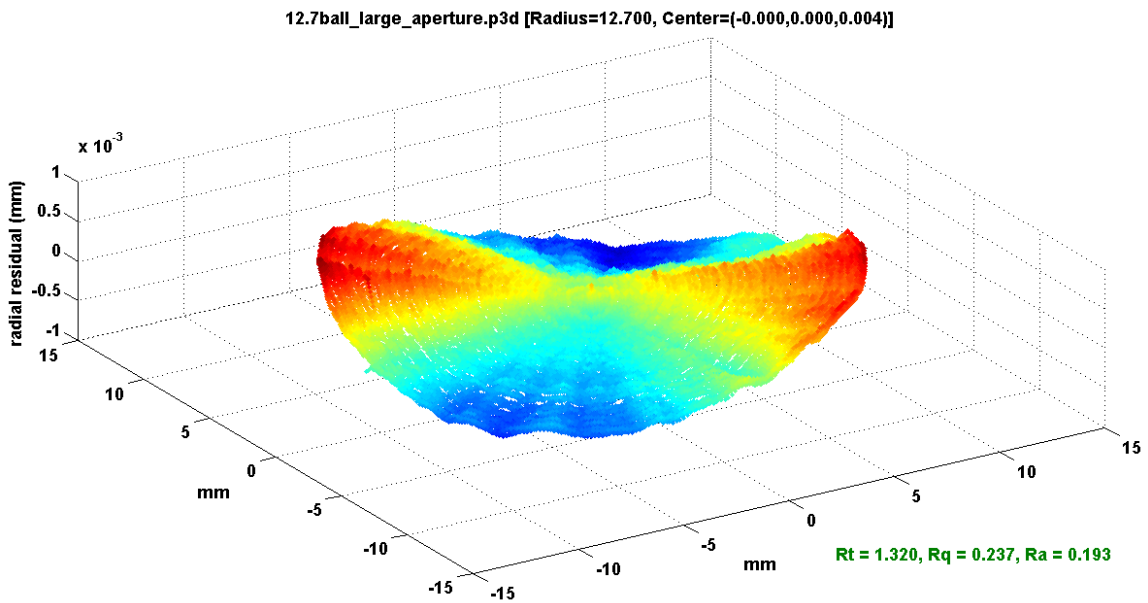Rt = 1.320, Rq = 0.237, Ra = 0.193

Figure 5. 12.7 mm ball measured over a 22 mm aperture diameter without error compensation.
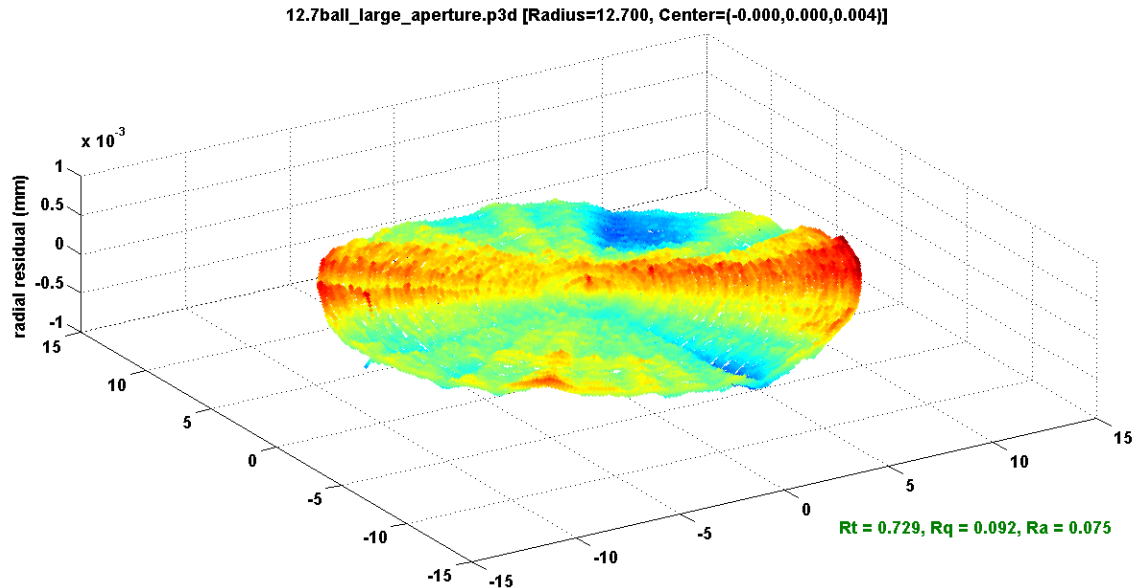
Figure 6. 12.7 mm ball measured over a 22 mm aperture diameter with error compensation.

1.5 CONCLUSIONS

As the accuracy requirements for Polaris3D continue to increase, better probes and increased error compensation must be implemented. The probe upgrade and compensation for φ axis errors and spindle misalignment have shown significant improvements to the instrument.

REFERENCES

1. Sohn, A. Polaris 3D Error Compensation. Precision Engineering Center Annual Report, 27, 1-23, North Carolina State University (2009).

2. Sohn, A. Polaris Mechanical Design and Alignment Procedures. Precision Engineering Center Annual Report, 26, 21-41, North Carolina State University (2008).

3. Sohn, A., Garrard, K. The Polar Profilometer Polaris. Precision Engineering Center Annual Report, 19, 1-16, North Carolina State University (2001).

4. Garrard, K. Polaris 3D Operation and Control. Precision Engineering Center Annual Report, 27, 24-46, North Carolina State University (2009).

2 MEASURING TRANSPARENT SURFACES WITH POLARIS 3D

Alex Sohn
PEC Staff

The measurement of transparent surfaces has been explored on Polaris 3D. The low reflectivity of transparent surfaces presents some unique challenges but when combined with advanced probe hardware and techniques, accurate measurement of glass, acrylic, and other transparent surfaces becomes possible. In addition to first surface measurement, thickness measurement is explored. Thickness measurement, while possible, introduces additional difficulties that have made implementation challenging.
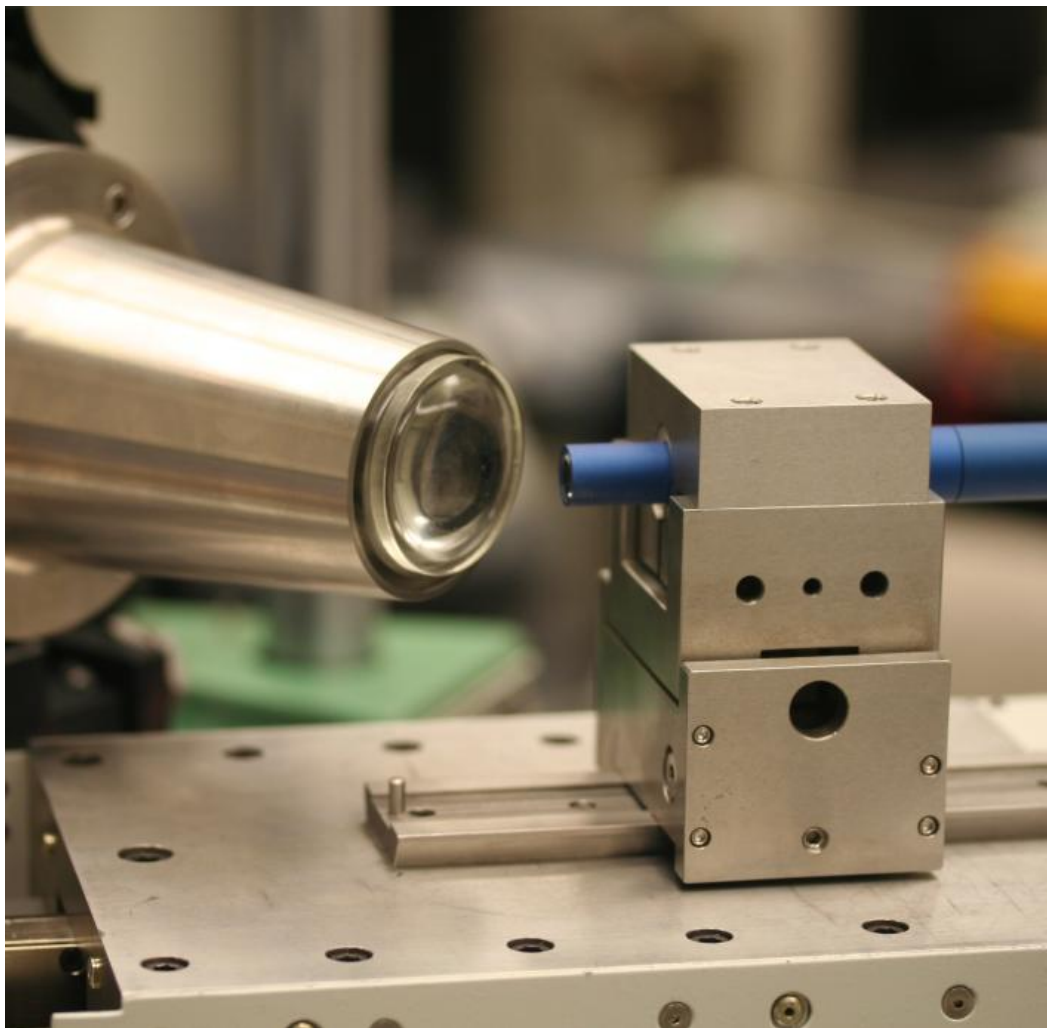
2.1 INTRODUCTION

Reflective optical surfaces have been measured with Polaris3D since its completion in 2008. Measurement of transparent surfaces using Polaris 3D opens a new field of applications, particularly in refractive optics measurement. Since the reflectivity of a typical transparent surface is much lower than a polished reflective surface, an optical probe must either use a more intense source or be more sensitive. Additionally, while first surface measurements can be made directly without compensation, there are some complications with respect to adjusting the sensitivity of the chromatic aberration (CA) probe.

Two different probes were considered, though in the end, only one was found suited to measuring transparent surfaces and was used for all measurements. Furthermore, it is possible to measure through transparent surfaces to measure second surfaces or thickness. This, however, becomes a more complicated endeavor as the optical path of the CA probe is modified by the first surface. The measurement of the second surface must therefore be compensated for the influence of the first surface.

2.2 PROBE CONSIDERATIONS

The main difference between measuring reflective and transparent surfaces is that the reflected intensity from the transparent surface is substantially lower. Compared to polished aluminum, which has a reflectivity of around 95%, the reflectivity of glass or many optical polymers with refractive indices of around 1.5 is about 4%. This means that the signal intensity is about 20 times lower when measuring a transparent surface. There are two ways of accommodating this disparity in intensity: 1) The intensity of the source can be increased or 2)the measured signal can be collected for a longer time. In the case of the CHRocodile S probing system, the sampling rate on the probe was reduced from 2 kHz to 320 Hz. This reduction in sampling rate increases the exposure time of each sample and hence, the measured intensity. Measured intensity for transparent plastic was typically around 35% at normal incidence (compared to 95% for specular brass). This was enough to permit probe following to function properly.

The probe used for all transparent surface measurements was the 300 µm range CHRocodile probe due to its higher sensitivity as compared to the 600 µm range CHRocodile probe or the 300 µm Stil CHR150-N probe.

2.3 SURFACE MEASUREMENTS

First surface measurements of molded plastic surfaces were performed to find the transfer function between the mold and the plastic lens created from that mold. Figure 1 compares the measurement of a diamond-turned convex spherical brass mold and a concave transparent plastic part. The astigmatic (nominal 9 mm radius of curvature) design surface was subtracted from both measurements, all values were inverted of the plastic design file and a design shrink factor was applied to the plastic data. Peak-to-valley numbers (0.614 μm for the mold vs. 0.850 μm for the plastic) do not differ significantly, signifying successful replication, though a defect (shown at the O.D. in the 1 o'clock position of Figure 1b) had to be excluded because its 15 amplitude obscured all other results.
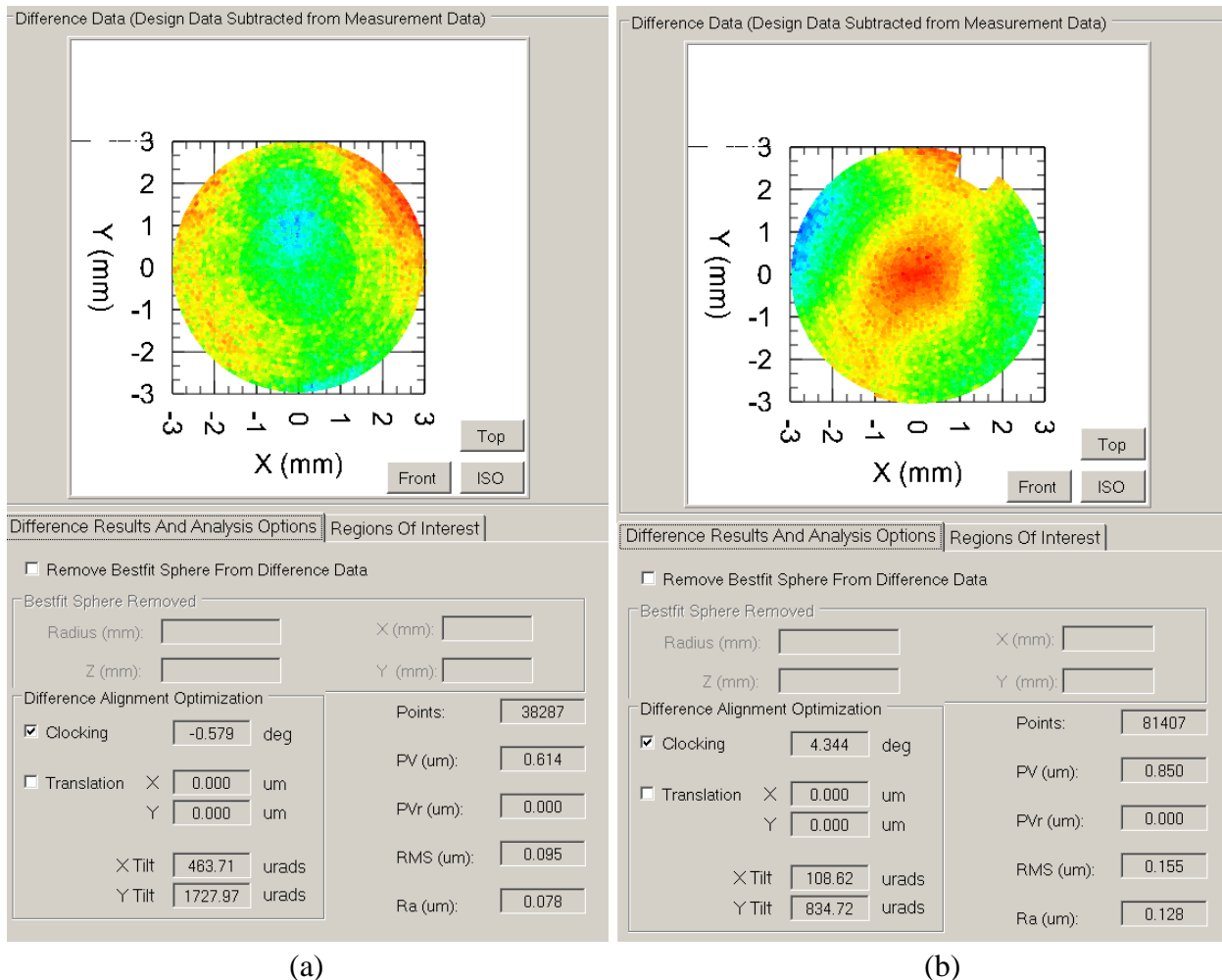

(a)   (b)

Figure 1. Measurement results for a diamond-turned brass mold (a) and transparent plastic part (b). Both results represent the residual error from the design surface.

2.4 THICKNESS MEASUREMENT

Thickness measurement with CA probes is possible in two different modes: Direct thickness measurement and indirect. Direct measurement is possible when the apparent thickness of the measured part lies within the measurement range of the probe and two spectral peaks are obtained simultaneously as shown in Figure 2. This method is useful in measuring thin windows or films. Addition of the thickness measurement to a first-surface measurement can produce the profile of the second measurement.
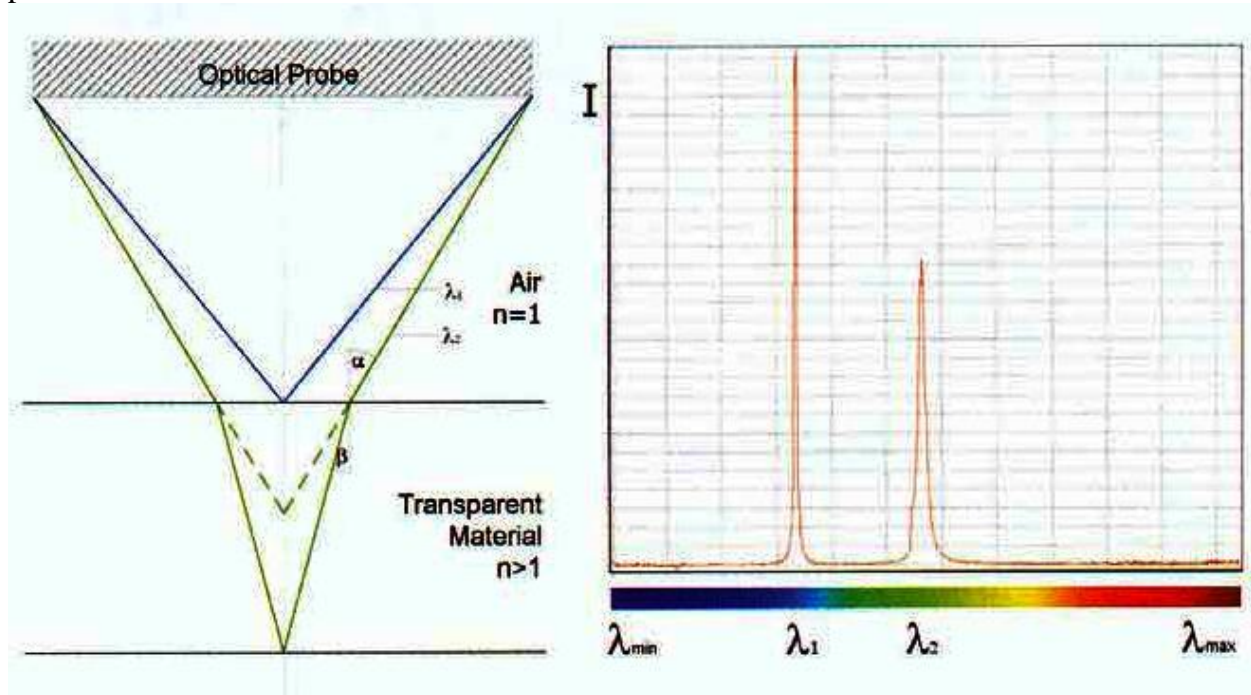

Figure 2. Direct thickness measuremnt using a CA probe [1].

Indirect thickness measurement is used when the apparent thickness of the part is greater than the probe's measurement range. This is the method used for measuring lenses or parts with a thickness greater than the 300 μm measurement range of the probe used. This indirect method involves measuring the first surface of the lens and then subtracting the second surface measurement from this data. Both thickness measurement techniques, however, are complicated by the fact that measurement of the second surface is perturbed by refraction at the first surface. The consequence of this is that the perturbation must be compensated.

A section measurement of a polystyrene (n=1.57) lens, for example, revealed the thickness to be 664 μm. With the probe, the thickness was measured at 398 μm. To compensate the impact of refraction, the aperture must be known, a quantity not given for the probe. The compensation's dependence on aperture is shown below and in Figure 3.
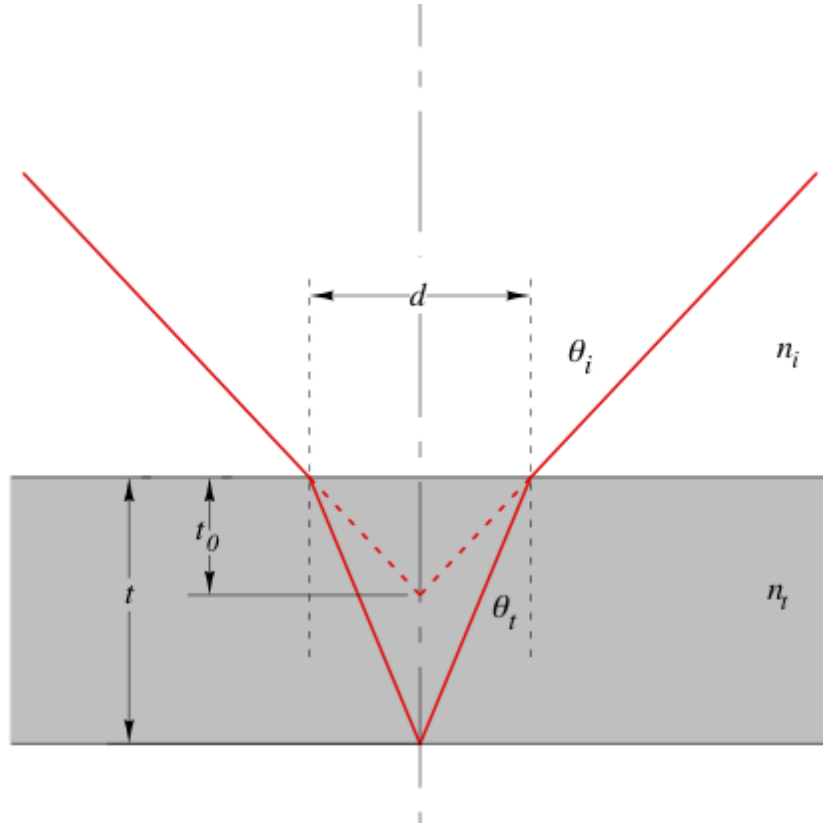
Figure 3. The measured thickness, t_0 is perturbed by refraction at the interface between the two refractive indices, n_i and n_t.

Snell's law,

$$n_i \sin \theta_i = n_t \sin \theta_t \tag{1}$$

where n_i is the refractive index of the incident medium and n_t is that of the transmitted medium. Likewise, θ_i and θ_t are the incident and transmitted angles, respectively. From the geometry shown in Figure 3,

$$\tan \theta_i = \frac{d}{t_0} \tag{2}$$

$$\tan \theta_t = \frac{d}{t} \tag{3}$$

where t_0 is the measured thickness of the part, t is the actual thickness and d is the aperture diameter on the surface of the part.

Solving for t_0:

$$t_0 = d \left[\tan \left\{ \sin^{-1}[\tan^{-1}(d/t)] \right\} \right]^{-1} \tag{4}$$
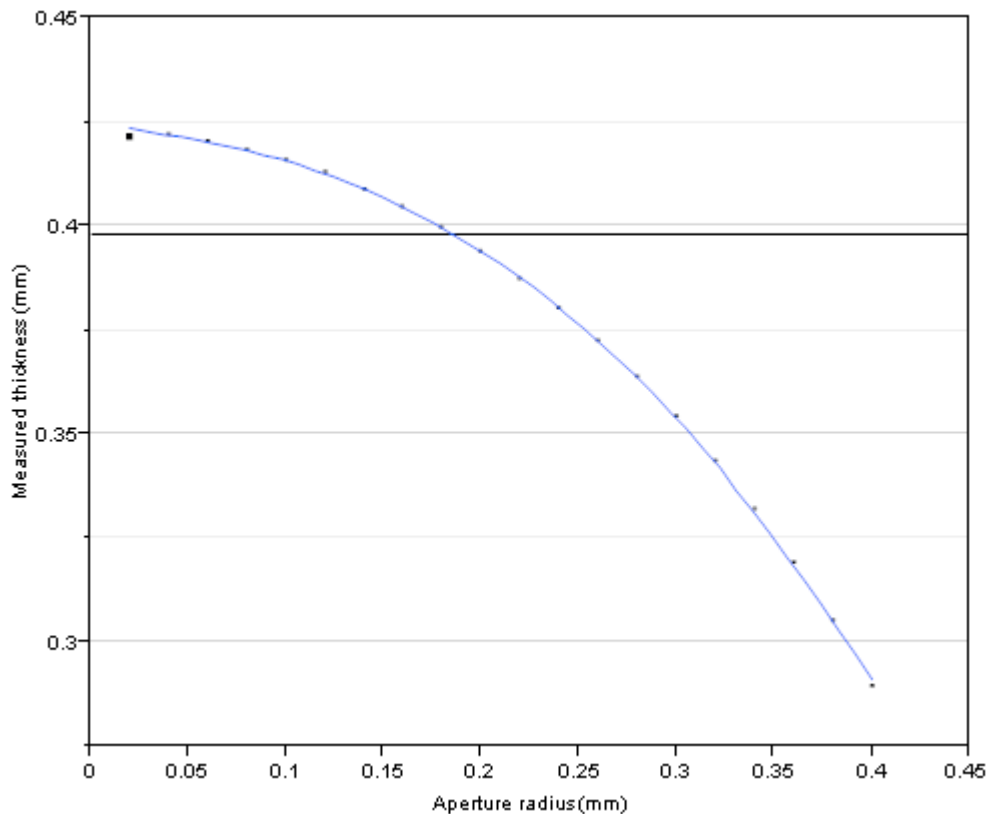
13

Figure 4. Plot of measured thickness vs. aperture radius given a refractive index of 1.5. The measured thickness of 0.398 mm is indicated with a line, the intersection with the curve shows the apparent aperture size.

Equation 4 is evaluated for a range of aperture sizes and plotted in Figure 4 to show how the measured thickness varies with aperture. This would indicate that the dominant contribution comes from an aperture of approximately 0.18 mm, though contributions from the entire aperture means this is more likely just an average. Consequently, the spectrum for measuring through a planar or quasi-planar surface at normal incidence would be broader than one measured through air only. This is illustrated by the spectra of the first and second surfaces shown in Figures 5 and 6, respectively. Figure 5 shows the spectrum of a first-surface reflection with a full width at half-max (FWHM) measurement of approximately 30 nm whereas Figure 6 shows a FWHM of nearly twice that number.
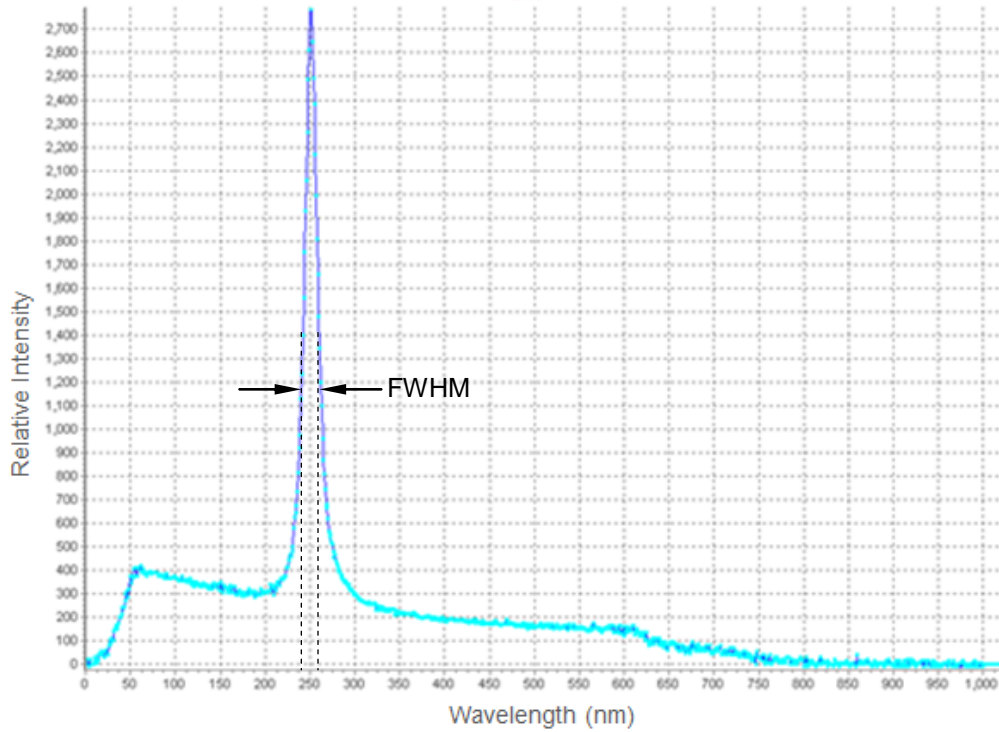
Figure 5. Spectrum plot of the signal from the first surface of a transparent plastic part. FWHM is approximately 30 nm.
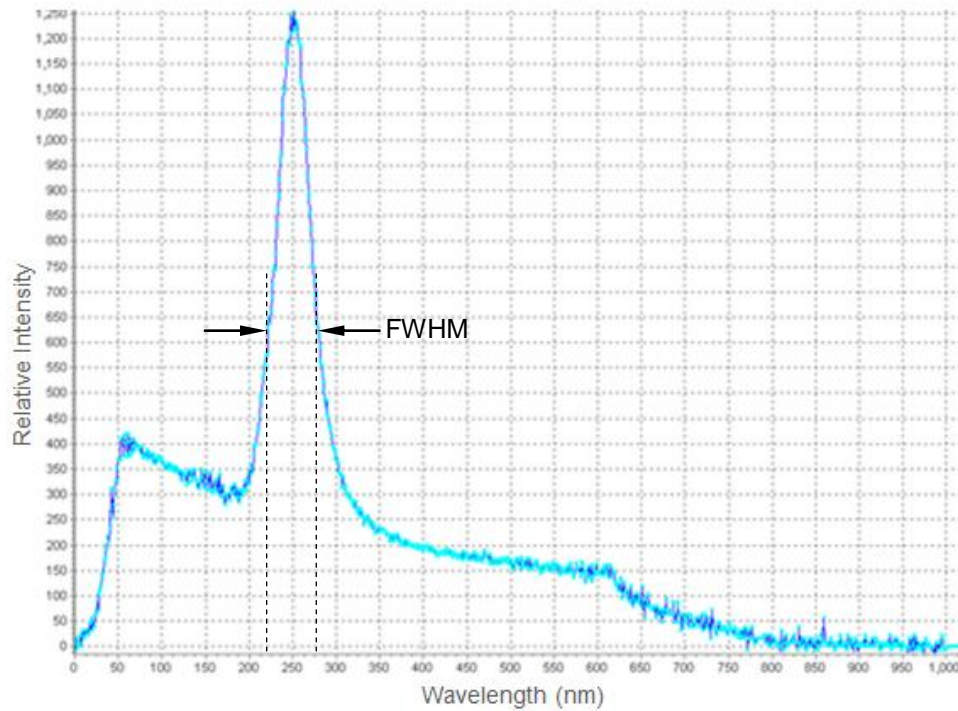

Figure 6. Spectrum plot of the signal from the second surface of a transparent plastic part. Note the broader peak. FWHM is approximately 60 nm.

Given that the probe aperture is fixed for any given probe, the ratio of aperture to thickness and, hence, the angle of incidence and angle of refraction should be constant for quasi-planar surfaces. Using the plot in Figure 4 to find d/t and Equations 2 and 3 to find θ_i and θ_t a compensation formula to find t when only t_0 is known can be written as:

$$t = t_0 \frac{\tan \theta_i}{\tan \theta_t} \tag{5}$$

or

$$t = t_0 k , \tag{6}$$

where k is a correction constant that is measured for each material. In the case of polystyrene, it is 1.668. Other materials will vary.

This compensation holds only at normal incidence where the radius of curvature of the surface is large compared to the thickness (~100 times greater). The impact of first surface curvature and non-normal incidence on thickness measurement still has to be evaluated. It is, however, clear that the impact on the measured thickness is significant. For example, the center thickness of a curved plastic window with concentric 1st and 2nd surface radii of approximately 9 mm was measured using Polaris 3D. The apparent thickness was measured from both directions with the result being 434 µm when the convex side was the 1st surface and 407 µm when the concave side was the 1st surface. This result underscores the importance of finding a compensation algorithm for this error by virtue of the fact that the difference between the two measurements is 27 µm.

2.4 CONCLUSIONS

The capability for Polaris 3D to measure transparent surfaces was clearly illustrated. First surface measurements showed that the first surface of a refractive optical element can be measured just as well as that of a highly reflective element. The only modification to the setup for measuring transparent surfaces is to lower the CA probe sampling rate by about a factor of 10. Measurement of a second surface transparent part is possible as well, though matters of refraction at the 1st surface must be dealt with to obtain accurate measurement results for second surface profile and thickness.

REFERENCES

1. Michelt, Berthold and Schultze, Jochen, *The new Chrocodile M4*, Glas Ingenieur, 16, pp35-37 (2006).

3 FLORA II UPGRADES AND PERFORMANCE TESTING

Thomas A. Dow
Faculty
Kenneth Garrard
Senior Research Associate

The Fast Long Range Actuator (FLORA II) was developed to machine non-rotationally symmetric surfaces on a lathe with a diamond tool. FLORA was designed to have a much longer range than piezo based fast tool servos and significantly higher throughput than the slow slide servo technique. Excellent actuator performance was previously demonstrated but the user interface needed a major overhaul to improve it efficacy. Over the past year the actuator and its controls have been upgraded and improved and FLORA II is now fully integrated into a diamond turning machine. Specifically, the safety circuits, control system and user interface have been re-engineered and software to reduce a surface design into the motion program specifications needed for machining the surfaces is available.
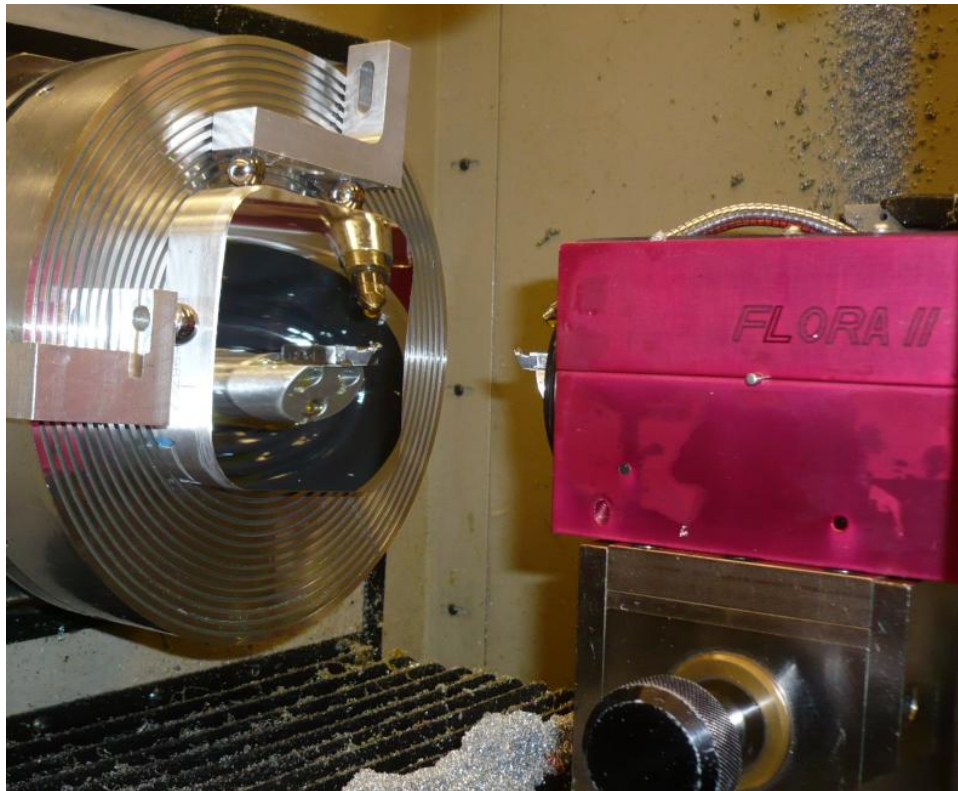
3.1 INTRODUCTION

The fabrication and measurement of non-rotationally symmetric (freeform) optical surfaces have long been goals of the PEC. The 3D Polaris discussed in Sections 1 and 2 provides a unique way to measure these parts which can be fabricated using a variety of fast tool servos powered by piezoelectric actuators or linear motors.

A project funded by NSF beginning in 2007 was aimed at developing a new servo design. The goal was a light but rigid mechanical design with a high-performance control system to improve the surface finish and figure error of the surfaces created. The NSF project was performed by two graduate students, Qunyi Chen, a PhD graduate, and Erik Zdanowicz, a MS graduate. At the conclusion, the new actuator design – FLORA II – was working and a DSP based controller operating at 20 KHz was built to control it. However, as with many of these student projects, the final result was usable but not user friendly. The effort reported here describes the improvements to the FLORA II system that enhance the user interface, simplify the operation and provide a variety of data entry options.   Also described are fabrication results for a tilted flat test part and an off-axis biconic mirror.

3.2 FLORA II IMPROVEMENTS
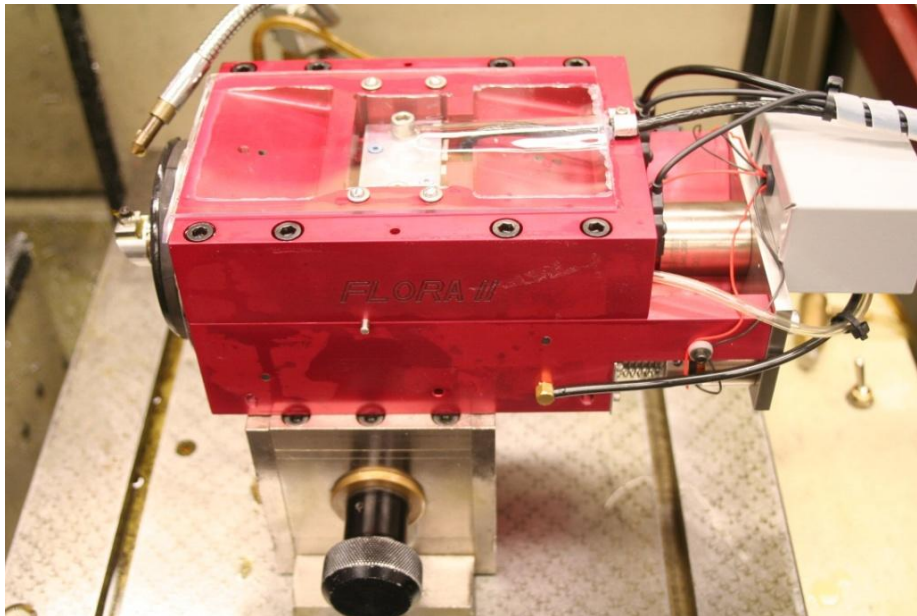
3.2.1 FLORA II STRUCTURE

Figure 1. FLORA II actuator on micro-height adjustor

The FLORA II actuator (**F**ast **LO**ng **R**ange **A**ctuator) developed over the past several years at the PEC under NSF funding has been used to produce several outstanding optical surfaces over the past year. The current implementation of this servo is shown in Figure 1. Recent changes include:

- the limit switch system and emergency stop have been improved,
- new wiring has been installed,
- a new cover to protect the encoder has been fitted and
- the counterbalance system has been integrated into the controller.

3.2.2 USER INTERFACE

The PMDi control system has been upgraded with a user interface that provides important new functionality to start the actuator, find the encoder home reference, communicate with the host DTM and load data files for freeform surface fabrication. A screen shot of the user interface is shown in Figure 2.

Figure 2. FLORA II user interface

The updated graphical user interface (GUI) was a major effort performed by Ken Garrard based on a design initially provided by PMDi that was customized by Qunyi Chen and Erik Zdanowicz. The GUI is programmed in Microsoft Visual Studio using C# and provides the user with information on the status of the FTS and DTM (relative positions, offsets, etc.) in the top half and provides buttons in the bottom half to initiate actions of interest such as home the axis, emergency stop, load a program, etc. The buttons can be active or inactive (grayed out) depending on a block diagram of other actions possible once in that condition. Real-time data acquisition is available at any integer multiple of the servo update rate. Data can be streamed to the PC hard drive indefinitely, i.e., until the disk is full. Programming a robust interface is a very time consuming effort as the consequences of each action must be thought out and ways to recover from response/errors must be defined. A state-machine approach was used to enumerate all the possible interactions between the operator, software, hardware and the allowable transitions.
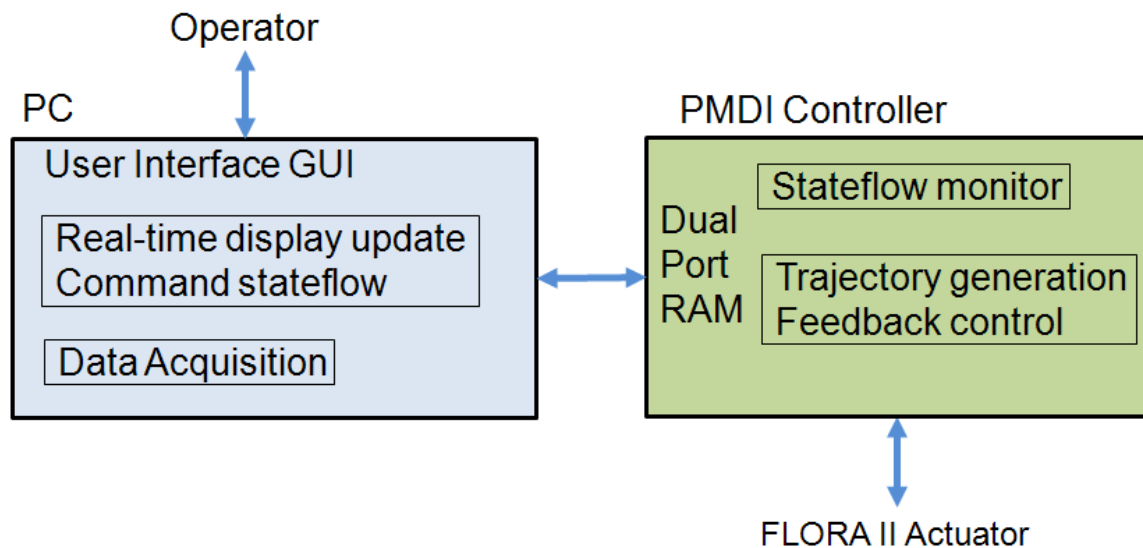

Figure 3. Control system components.

The layout of key system components of the FLORA II control system is shown in Figure 3. The operator communicates with the user interface GUI which interprets button clicks, typed data inputs and mouse movements. The asynchronous functionality is provided by C# and the Windows .NET environment, linking screen objects with handler functions. Two additional, independent threads of execution are implemented: one to refresh the real-time display with operational data and send new commands to the control system and the other is a high-priority task dedicated to data acquisition. All communication between the PC and the PMDI controller is through dual port RAM located on the PMDI DSP board. Every millisecond, the DSP executes a stateflow monitor task to interpret and perform commands requested by the GUI. The monitor task also reports the status of previous commands and ensures a graceful transition

20

between states (e.g., power-up, open-loop homing, manual jog, automatic program execution, program abort, emergency stop, etc.). The DSP also executes the trajectory generator and servo control task every 50 μsec. This high priority task

- interrupts the monitor task,
- reads the current axes positions,
- generates position, velocity and acceleration set points for the actuator,
- calculates a new control loop output and
- updates the voltage to the servo amplifiers for the main actuator piston and counter-balance voice coils.

The controller generates position, velocity and acceleration command signals for the servo loop as a function of the spindle and axes positions of the DTM. A bilinear interpolation function is implemented to represent any surface as a plaid, but not necessarily uniformly spaced, 2D grid of set points. Velocity and acceleration are calculated with balanced finite differencing. Interpolation of tool position at an arbitrary point, P_k, inside the data grid is illustrated in Figure 4.
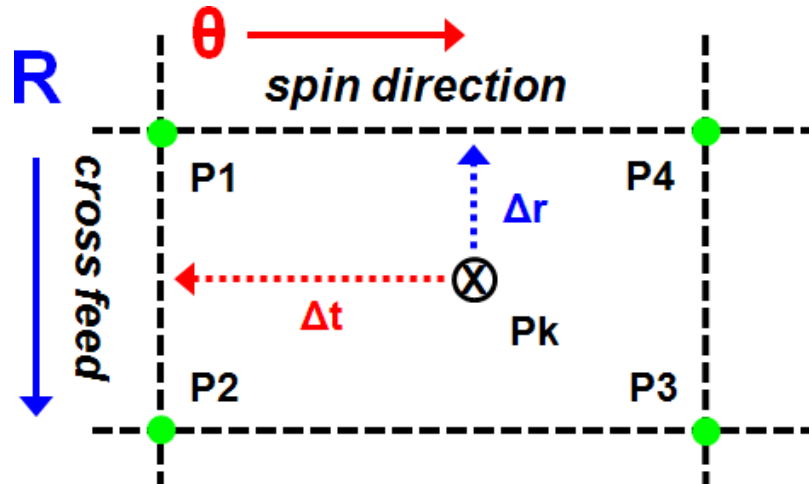

Figure 4. Bilinear interpolation of position.

The position set point is calculated from P1 to P4 as,

$$P_k = P1 \times (1-\Delta r) \times (1-\Delta t) + P2 \times \Delta r \times (1-\Delta t) + P3 \times \Delta r \times \Delta t + P4 \times (1-\Delta r) \times \Delta t \qquad (1)$$

Equation (1) can be used to interpolate velocity and acceleration as well if grids containing those quantities were available. However to minimize the RAM required, a balanced finite difference is used to estimate V1 to V4 and A1 to A4. Note that V1 and V2 require position points earlier (to the left) from the grid and V3 and V4 require points from the right in the grid. Similarly estimating accelerations A1 to A4 are made by expanding the region of the grid to 12 points.

The final values for velocity and acceleration must be scaled according to the spindle speed and cross feed velocity, which are continuously updated by the controller. Note that at each servo update cycle the next point, P_{k+1}, is at most one grid position away from current location and the intermediate results from the previous cycle can be used to reduce the computational load.

3.3 MACHINED OPTICAL SURFACES

3.3.1 FLAT BRASS TEST PART

A 12 mm OD flat brass sample was machined with the FLORA II holding position. The shape of the machined surface is shown in Figure 5. With a spindle speed of 600 rpm, feed rate of 1 mm/min and tool nose radius of 2.393 mm, the theoretical finish is 0.04 nm. While the finish did not achieve this value, it was equivalent to a fixed tool holder - 11 nm PV and 2 nm RMS.
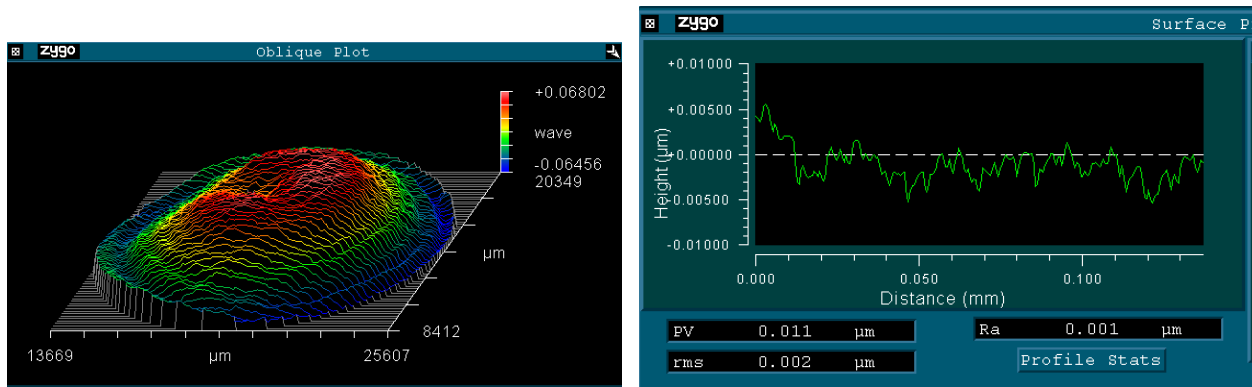

Figure 5. 12 mm Brass flat with 11 nm PV figure error and 2 nm RMS surface finish

3.3.2 TILTED FLAT

To provide a test of the dynamic response of the FLORA II, a tilted flat was machined in brass. For this test the surface shape in cylindrical coordinates is a linearly increasing cosine wave described by Equation (2),

$$z(r,\theta) = A\frac{r}{W}\cos\theta \qquad (2)$$

where A is the wave amplitude, W is the workpiece radius, r is the radial position of the tool and θ is the spindle angle in radians. Because the contact angle between the tool and the workpiece changes as a function of spindle rotation, a correction must be made for the tool nose radius, T_r, as given by Equation (3).

22

$$z_t(\theta) = \left| T_r \left(\sqrt{1 + \left(\frac{A}{W} \right)^2 \cos^2 \theta} - 1 \right) \right| \tag{3}$$

This correction is a twice/revolution command with a magnitude on the order of 1 µm for the ± 500 µm range of motion for this particular tilted flat. The command calculated by the FLORA II trajectory generator is thus the surface shape plus the tool radius correction (Equation (4)).

$$z_p(r,\theta) = z(r,\theta) + z_t(\theta) \tag{4}$$

The FLORA II feedback controller with encoder position sensing and velocity and acceleration feed-forward minimizes the following error. The velocity and acceleration for the tilted flat are functions of the radial position, the spindle angle and the spindle rotation speed and are given by Equations (4). A counterbalance system is used to reduce the influence of the FLORA II piston inertia on the DTM axes. The feed-forward commands (acceleration and velocity) are also sent to the open loop counterbalance pistons on the FLORA II (shown in the lower back in Figure 1). The counterbalance system reduces the machine error motion at 10 Hz to a value less than 10 nm.

$$z_v(r,\theta) = -A \cdot \frac{r}{W} \cdot \frac{d\theta}{dt} \sin(\theta)$$

$$z_a(r,\theta) = -A \cdot \frac{r}{W} \cdot \frac{d^2\theta}{(dt)^2} \cos(\theta) \tag{5}$$
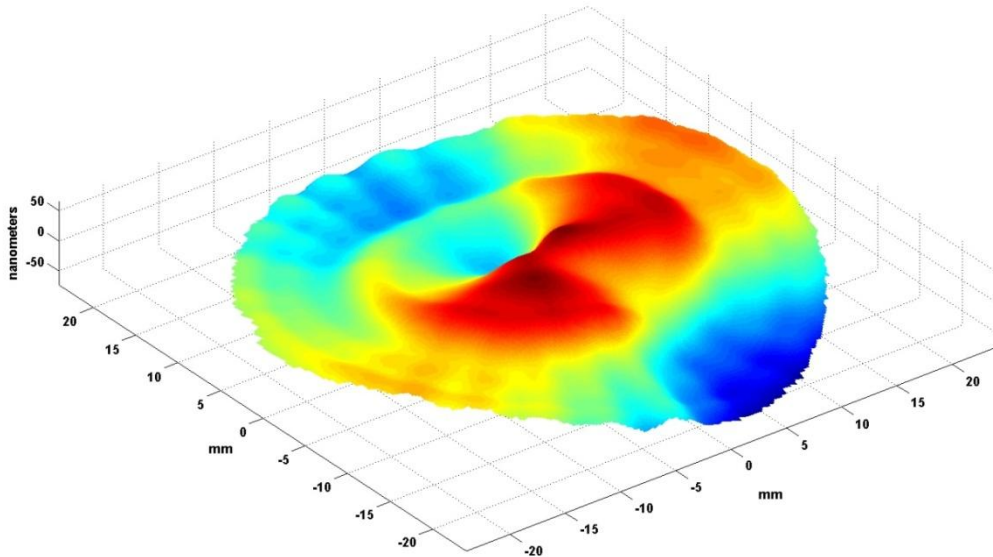

Figure 6. Less than 100 nm figure error was generated on a 50 mm diameter tilted flat brass workpiece machined at 600 rpm with a PV tool motion of 1 mm.

For the tilted flat, the position command as well as the velocity/acceleration feed-forward and tool radius correction can be generated in real-time using Equations (5). For a more general surface shape however, these need to be generated based on the desired shape which may come from an optics design and may not have a specific equation.

The reason for machining a tilted flat was to demonstrate the capability of the actuator to follow a 10 Hz sine wave with decreasing amplitude from OD to ID. Performance can be accessed by interferometric measurement of the machined part using a flat reference mirror. The form error shown in Figure 6 illustrates excellent fidelity in fabricating the tilted flat surface - the error is less than 100 nm for a command range of 1,000,000 nm at 10 Hz.
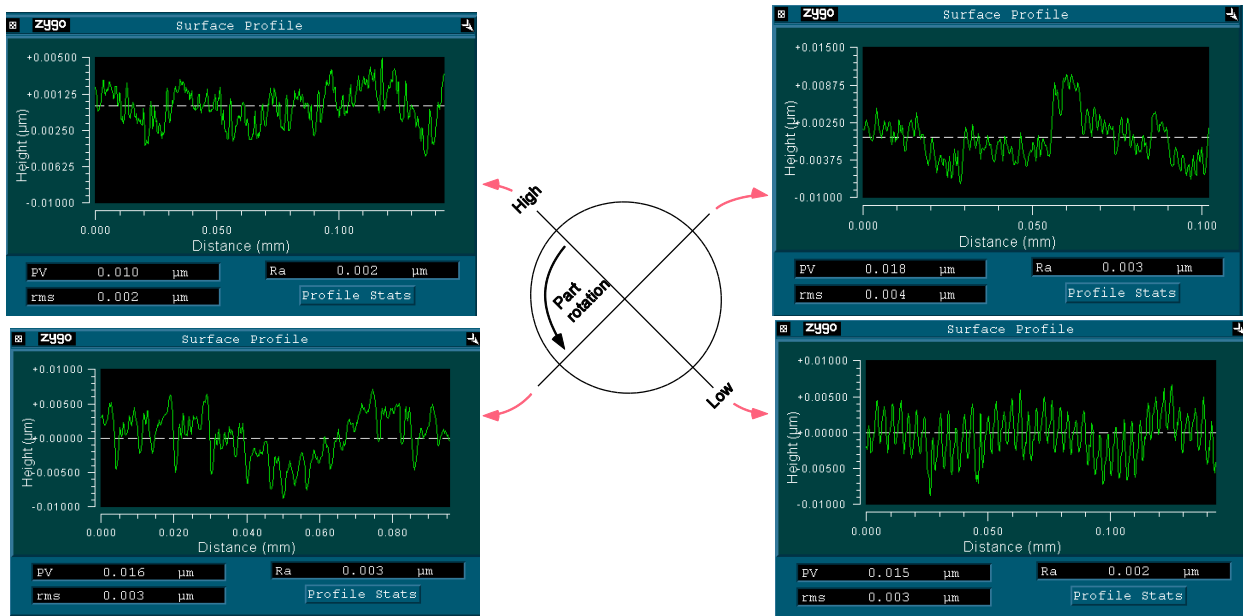

Figure 7. Surface roughness measured at 4 points on the outside edge of the machined brass tilted flat is less than 4 nm RMS. The main features are at the 3.3 µm/rev feed rate.

The surface finish using a long range fast tool servo generally degrades as the range of motion is increased. For the FLORA II this does not appear to be the case for a stroke up to 1 mm and a spindle speed of 600 rpm. The surface finish at 4 positions at the outside edge of the part is shown in Figure 7; the high (upper left) and low (lower right) points of the tilted flat where the velocity is zero as well as the points of maximum velocity (upper right and lower left) as the servo passes through zero stroke. The cutting conditions for the finish pass were 600 rpm spindle speed, 2 mm/min feed rate using a 2.393 mm radius tool and 1 µm depth of cut. The surface finish for all positions is from 2-4 nm RMS, which is excellent.

3.3.3 OFF-AXIS BICONIC REFLECTOR

The final optical surface in NASA's Infrared Multi-Object Spectrometer [1] is a 96x96x25 mm aluminum reflector which has a biconic shape. The aperture is decentered by (x_0,y_0)= (-2.01,227) mm. The flat back surface is defined to be parallel to the mean normal vector from the front surface, resulting in a tilt of 35.3° about the x axis. The aperture and optical axis are shown in Figure 8.
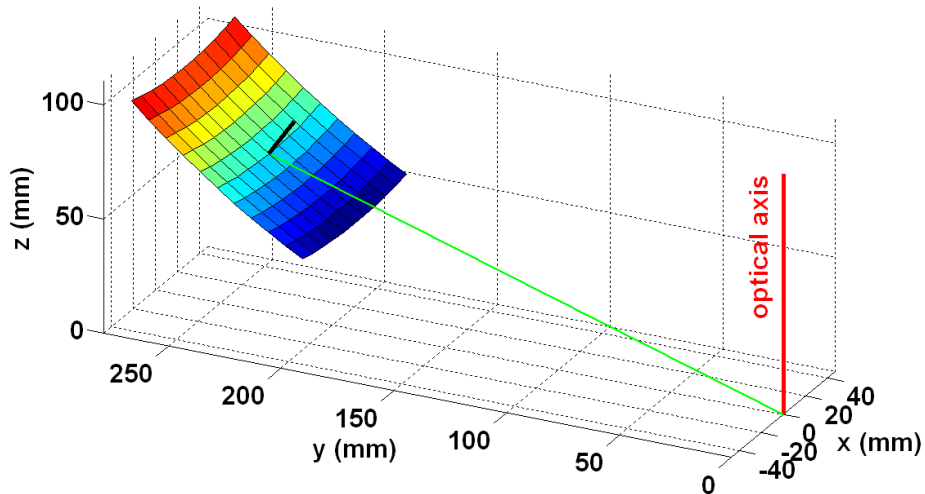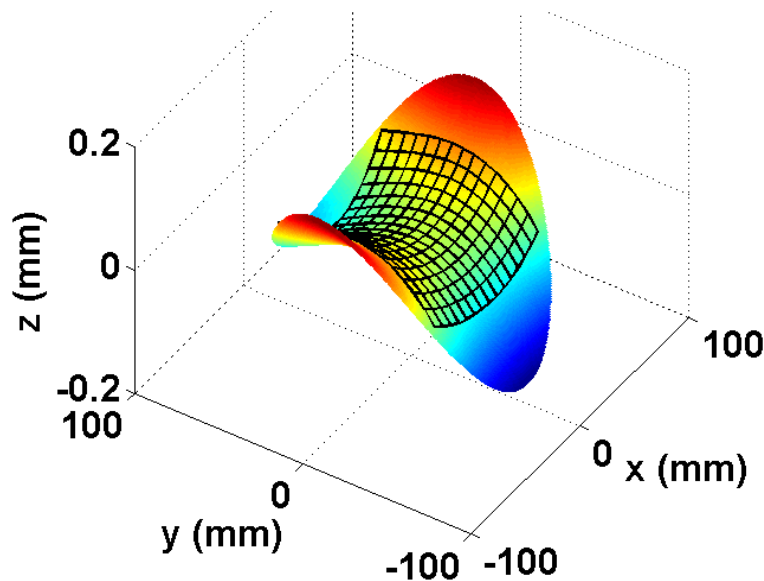

Figure 8. Biconic reflector surface.

Figure 9. NRS component of biconic after removing the best fit sphere with radius 373 mm.

25

A tool path for the biconic mirror was created by first removing the 35.3° tilt, translating the lowest point (i.e., smallest z value) to the origin. Next the surface data points were interpolated to a cylindrical mesh and tool radius compensation was performed. Finally, a least squares sphere was fit to the resulting surface to reveal the NRS component as shown in Figure 9. The range of FTS motion required is 288 µm. Within the defined clear aperture (shown as the mesh patch) the FTS range is 128 µm.
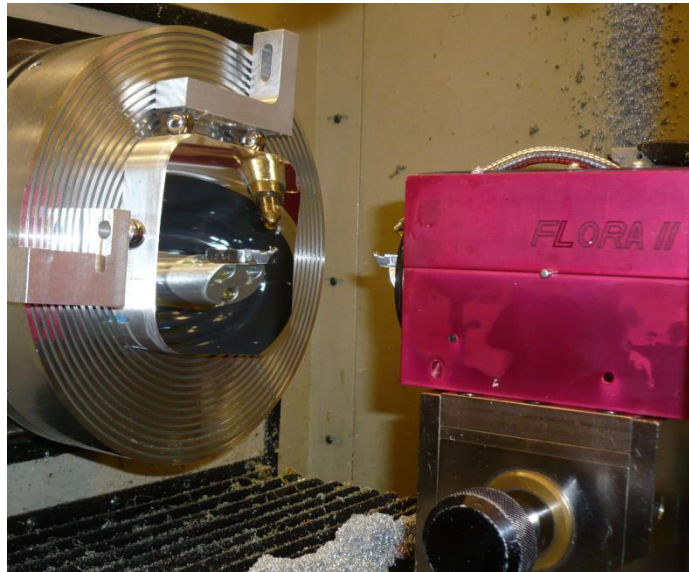
Figure 10. The Biconic Reflector M4 mounted on the ASG 2500 DTM. FLORA II is shown on right with the tool reflected in the mirror surface.

To test machining conditions, confirm tool centering and eliminate all systematic errors other than the fast tool servo, the best fit sphere with was first machined into the substrate. The figure error of this sphere was measured at 44 nm RMS and was considered satisfactory for proceeding with the biconic surface. The biconic mirror is shown in Figure 10 immediately after final machining with the FLORA II FTS.

CGH Form Measurement

Form measurement of free-form surfaces can be performed in a number of ways (e.g., Polaris 3D), but for this application a Computer

Figure 11. CGH fringe map showing the measurement area and the alignment ring.

26

Generated Hologram (CGH) was used. The CGH includes alignment fiducials to assure correct placement of the hologram in the interferometer. I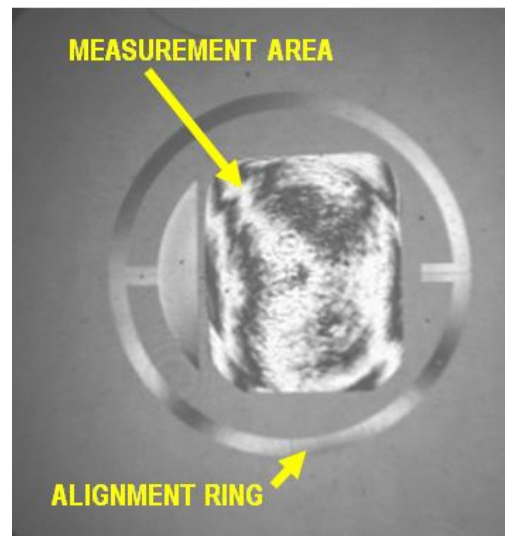nitial alignment for tip and tilt of the part substrate and the CGH plane is performed with a planar reference. Then a spherical CGH is placed in the converging beam of an F1.2 spherical reference. Lateral alignment and focus of the CGH mount is performed with this specially made holographic optic.
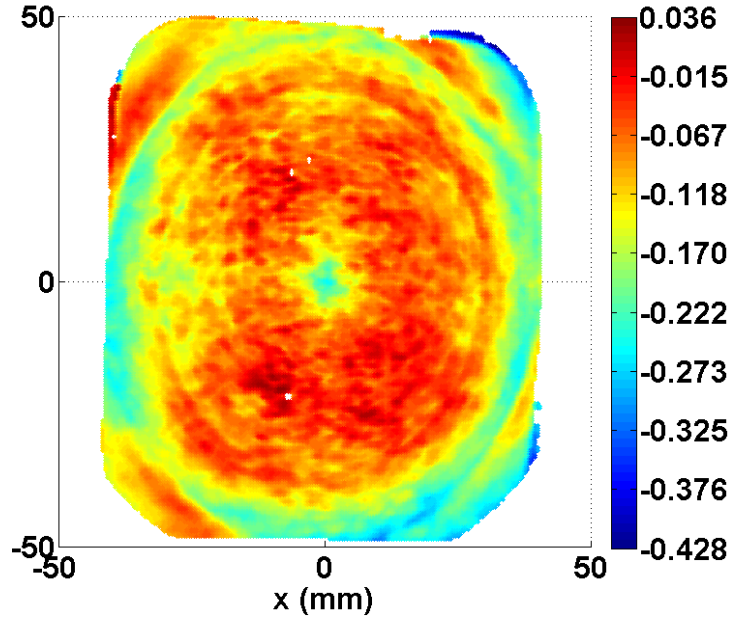
The CGH alignment to the interferometer is fine-tuned using the spherical reference ring around

Figure 12. CGH measurement with astigmatism removed by increasing the FTS gain. Residual RMS error is 43 nm.

the part measurement area as shown in Figure 11. Since the CGH is actually a diffraction grating, a 2 mm pupil is then placed at the focus and used to mask all but the first diffraction order. Finally, the part is aligned to the CGH in six degrees of freedom. This is an iterative process until a minimum error is found.

Results

The surface finish measured with a Zygo NewView 5000 SWLI was 3 nm RMS. RMS figure error was 127 nm and is dominated by astigmatism. The shape of the astigmatism is very similar to that of the FTS excursion shown in Figure 9. Applying a gain to the FTS motion of 1.005 removes the astigmatism and reduces the RMS figure error to 43 nm as shown in Figure 12. The gain change was performed in Matlab after importing the MetroPro measurement data file.

3.4 CONCLUSIONS

The FLORA II actuator has been fully integrated into the ASG 2500 DTM and used to machine non-rotationally symmetric surfaces with excellent surface finish and form fidelity. A graphical interface has been programmed that is user friendly and comprehensive – supporting all aspects of machine setup and operation. A data format and an interpolation code have been implemented for arbitrary surfaces of the form, $Z = F(r,\theta)$ and Matlab code for creating a FLORA input file has been developed.

REFERENCES

[1] Garrard K, Sohn A, Ohl R, Mink R, Chambers V. Off-Axis Biconic Mirror Fabrication. Proc. of the 3rd International Meeting of EUSPEN. 2002; 277-280.

4 INTEGRATED PRESCAN OPTICS FOR LASER PRINTERS

Alex Sohn
Research Assistant
Kenneth P. Garrard
Senior Research Associate
Precision Engineering Center

The design of a two element reflective optical system for a laser prescan unit has been completed. The optical system has been machined from a single piece eliminating the need for assembly and alignment of the two mirrors. However the mirrors in their correct orientation in the optical system are not rotationally symmetric about any axis. Matlab software has been developed to decompose a multi-element optical system into a best fit asphere and a non-rotationally symmetric surface. Tool path data for fabrication on the ASG 2500 Diamond Turning Machine augmented with a FLORA II fast tool servo are automatically generated by this software.
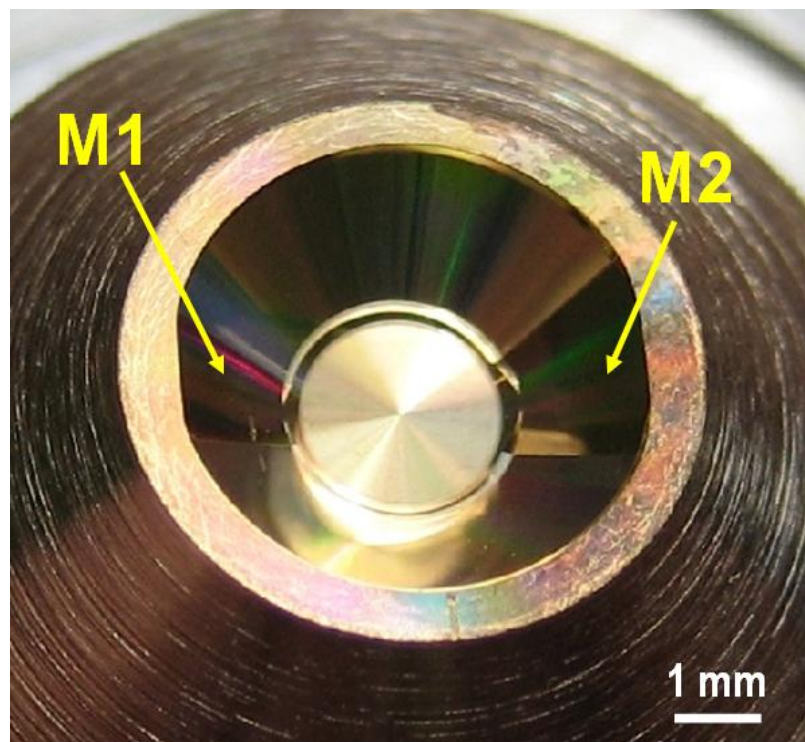
4.1 INTRODUCTION

One of the costliest and most challenging sub-systems in the manufacturing of lase print engines are the prescan optics. This group of components illustrated in Figure 1 conditions the laser beam from the exit aperture of a small diode laser and allows it to be directed to the surface of the paper and focused to a spot size as small as 10 µm. Typically, the prescan optics consists of the laser diode, a

Figure 1. Commercial laser prescan optical system.
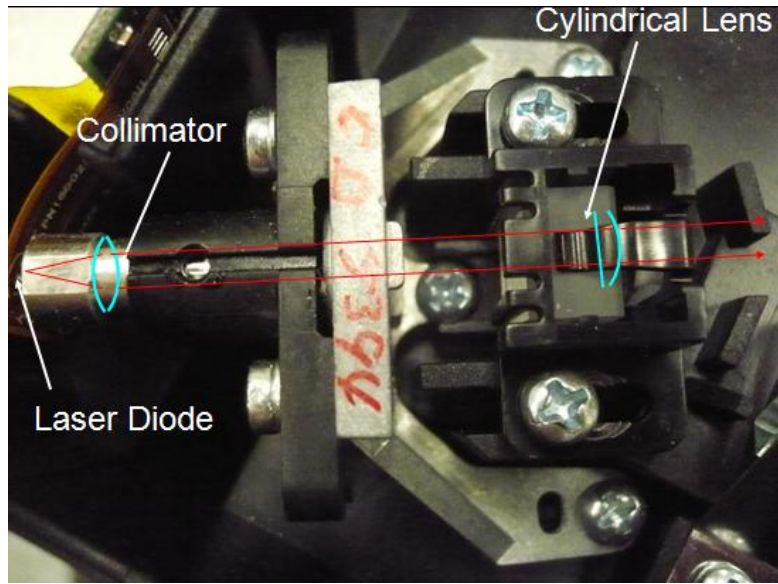
collimating lens to bring the laser beam as close as possible to collimate and a cylindrical lens to remove the astigmatism from the nearly collimated beam. The optics and their alignment add a significant cost to the final product, so the goal is to simplify the design and use materials that are less expensive to procure and manufacture.

A reflective optical system for a laser prescan unit has been proposed, designed and fabricated. This optical system can be machined from a single piece eliminating the need to assemble and align the two mirrors. However the optical surfaces in their final orientation are not rotationally symmetric about any axis. Matlab™ software for generating the tool path data needed to machine a prototype of this optical system using a fast tool servo has been developed. The optical system was machined on the ASG 2500 Diamond Turning Machine augmented with a fast, long-range tool servo (FLORA II) driven by a PMDi controller [1] (See Section 3).

4.2 OPTICAL SYSTEM DESIGN

The left side of Figure 2 shows the conventional system of Figure 1 in a schematic form. The collimating lens and the cylindrical lens are commonly made of optical glass and must be ground and polished. Cheaper polymer lenses cannot be used due mainly to the change in refractive index in the material with temperature. The printer must operate in an environment with a wide temperature range.
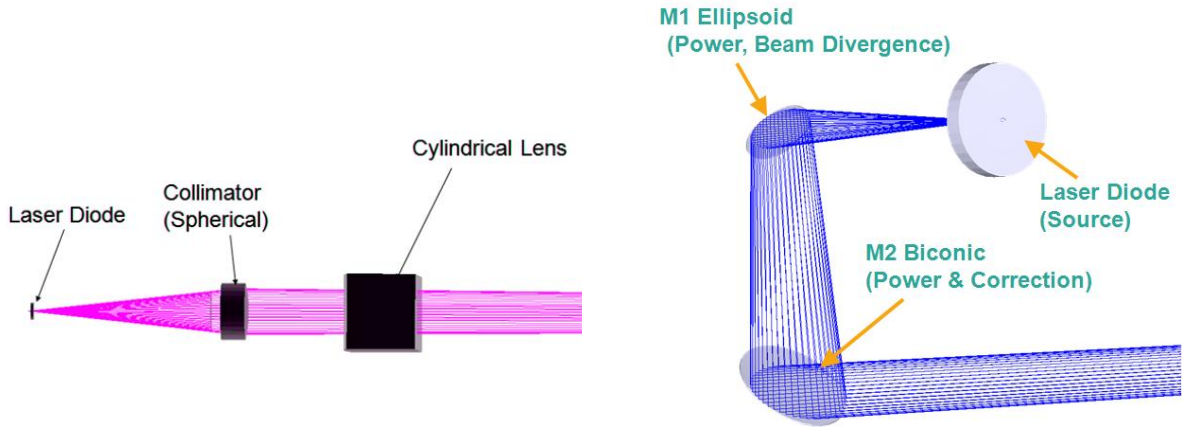
Figure 2. Conventional prescan lens design (left) and new 2-mirror reflective system (right).

If the lenses shown in Figure 2 are replaced with reflective optics, the refractive index of the material becomes irrelevant. Thus, molding polymer reflectors becomes a distinct possibility. One possible layout for such a design using reflective optics is shown at the right in Figure 2. The primary mirror is an ellipsoid and it removes most of the divergence from the beam while the secondary mirror removes whatever divergence remains as well as the aberrations due both to laser diode astigmatism and the off-axis placement of the primary mirror. Thus, the secondary mirror is biconic.
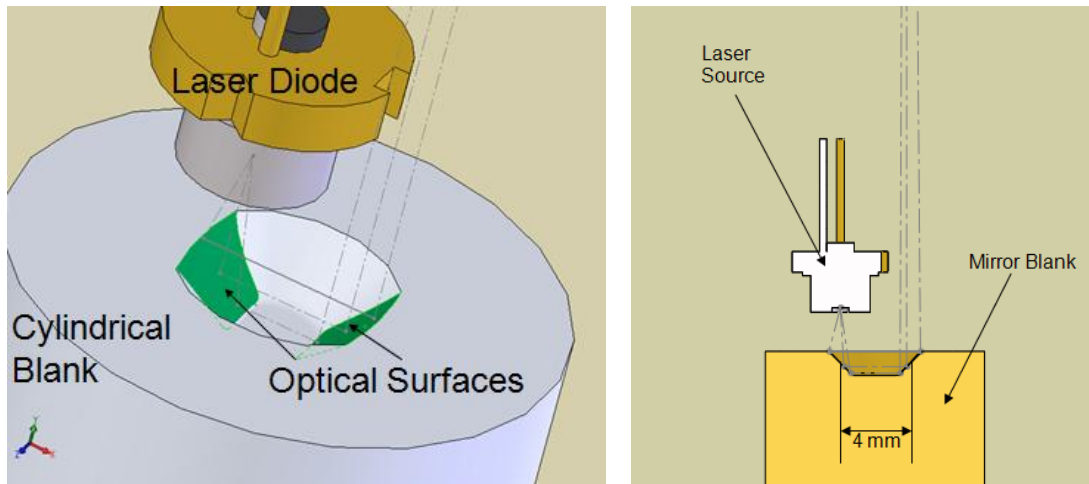
Figure 3. Solid model of mirror surfaces and beam path and a cross section of the system.

As a prototype, both mirrors were machined into the end of a small cylinder using the FLORA II fast too servo. As shown in Figure 3, the mirrors have a substantially larger radius than the radius of rotation and appear almost as two flat surfaces in a spherical parent surface. The cross section in Figure 3 shows the spacing of the mirrors and the laser source.

31

4.3 FABRICATION

Both optical surfaces can be machined in a single setup on a metal substrate guaranteeing the alignment of the two mirrors. As shown in Figure 4, the volume of material to be removed is quite small and the prototype can be fabricated without rough machining a spherical pocket or slot prior to performing the final machining operation. The diamond tool must be selected to reach into the pocket and machine the symmetric surface without touching the clearance face of the tool.
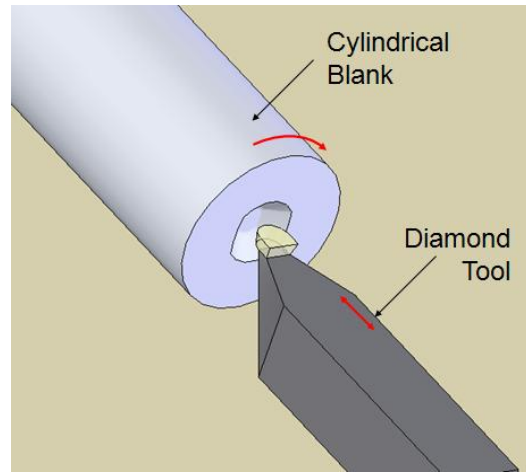
Figure 4. Machining layout.

4.3.1 GEOMETRIC ANALYSIS

Each mirror can be defined as a general biconic in Cartesian coordinates with Equation (1),

$$Z(x, y) = \frac{c_{XZ}(x - x_0)^2 + c_{YZ}(y - y_0)^2}{1 + \sqrt{1 - (1 + k_{XZ})(x - x_0)^2 c_{XZ}^2 - (1 + k_{YZ})(y - y_0)^2 c_{YZ}^2}} \tag{1}$$

where the origin is $(x_0, y_0, 0)$, c_{XZ} is the curvature in the XZ plane, c_{YZ} is the curvature in the YZ plane and k_{XZ} and k_{YZ} are the conic constants in the two orthogonal planes. The prototype design parameters are given in Table 1 and the apertures and their orientation with respect to each other are defined in Table 2.

Table 1. Surface parameters for prescan optics.

	Plane	Curvature (1/mm)	Conic constant
M1	XZ	1/30	1
	YZ	1/30	1
M2	XZ	1/13.905686	-2.396222
	YZ	1/34.682089	-60.00092

Table 2. Aperture definition of prescan optics.

	Aperture (mm)			Translation (mm)			Tilt (radians)		
	radius	x decenter	y decenter	x	y	z	x	y	z
M1	0.572995	0	0	0	2	0	pi/4	0	0
M2	0.916568	0	0	0	-2	0	-pi/4	0	0

Both surfaces are on-axis (i.e., no decenter) and M1 is an oblate ellipsoid of revolution while M2 is a non-rotationally symmetric surface of two very different hyperboloids. These two mirrors are shown in Figure 5. They have been translated to the correct separation but not tilted. Figure 6 shows M1 and M2 after tilting the mirrors along with a wireframe plot of an annular segment of the best fit sphere whose center is constrained to lie on the z axis (i.e., the axis of rotation during machining). The chief ray at the center of each aperture is shown as a dotted line and the center of the best fit sphere is shown as a dot. For this optical system a conical base surface provides a better fit, that is, the residuals have a smaller magnitude and the FTS excursion is reduced.

(a)   (b)
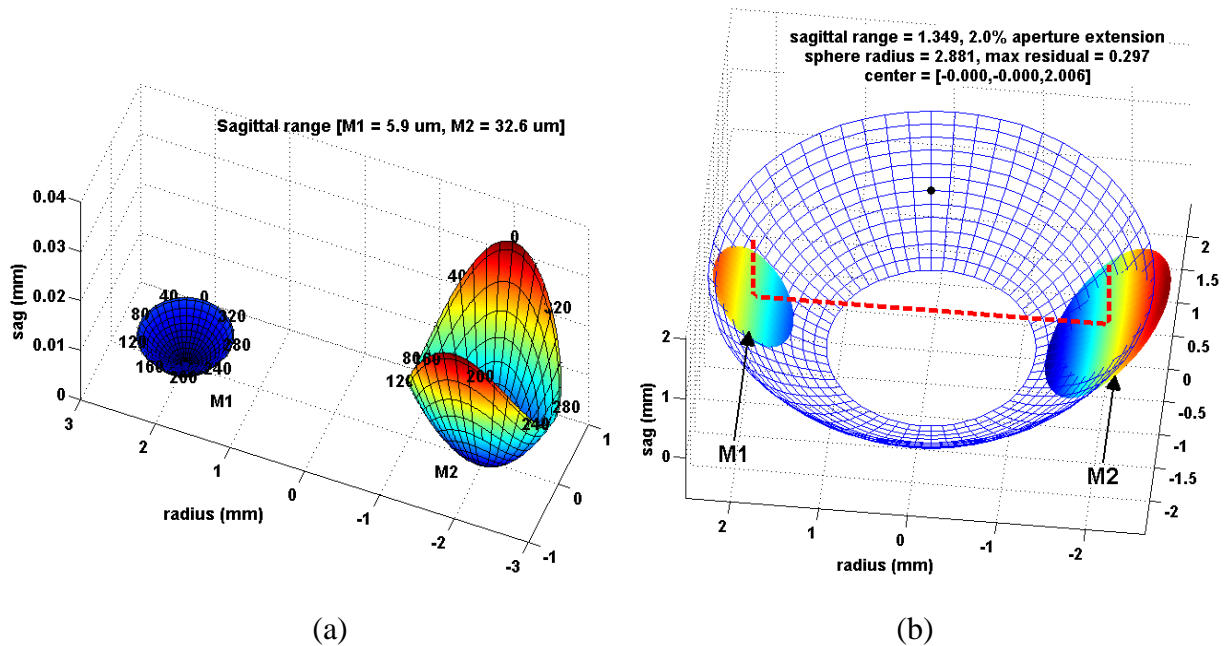
Figure 5. (a) The input mirror (M1) and the output mirror (M2) are shown as defined by Equation 1 and Table 1. (b) The laser prescan optical system with the mirrors in the correct orientation as defined by Table 2.

4.3.2 TOOLPATH GENERATION

The ASG 2500 diamond turning machine can be programmed to produce the spherical surface shown in Figure 7 while the FTS moves the tool in the sagittal direction as a function of the spindle rotation angle and the cross-feed axis position. The FTS motion plus the underlying sphere form the desired mirror surfaces. The mirror curvatures are much smaller than that of the best-fit sphere (i.e., they are "flatter" than the sphere), thus the shape of the FTS motion within the mirror apertures will be convex. The range of servo motion required is 297 µm.

33

Surface finish and form fidelity are likely to be improved if the range of FTS excursion is minimized. This can be done by machining an aspheric surface with the DTM. Compensation for the contact point along the radius of the tool must be included. This compensation is done along meridians from the axis of rotation to the edge of the workpiece. An asphere is then subtracted from the result to form a 2D lookup table of FTS positions as a function of radial and angular position. A part program for the ASG 2500 is created to machine the aspheric shape, which in this case is a 43.87° cone. A Matlab script has been developed to generate a lookup table for the FLORA II controller and the dSPACE Variform FTS controllers as well as the aspheric motion program for any two surface biconic optical system. This design file needed by the Polaris3D spherical profilometer [2] to measure the resulting part is also created. The steps in this algorithm are as follows:

1. Generate a circular aperture grid for each mirror, M1 and M2.
2. Calculate z positions for each (x, y) point within the apertures.
3. Translate and rotate the mirror surface data sets to their positions in the optical system.
4. Create a cylindrical coordinate grid for the optical system whose center is on the axis of rotation of the DTM spindle.
5. Find all data points on the cylindrical grid in the tilted elliptical apertures of M1 and M2.
6. Interpolate mirror surface data to the cylindrical coordinate aperture grid.
7. Extend the aperture masks to equal radii and uniform angles.
8. Perform tool radius compensation along each meridian in each aperture.
9. Interpolate compensated points onto a common radial grid.
10. Find the mid-range sagittal value at each radius.
11. Fit a radial polynomial to the mid-range data.
12. Form a table of residuals. This is the FTS excursion.
13. Create a motion program following the cross-section of the aspheric surface.
14. Output the FTS excursion formatted for the FLORA II controller.
15. Output a "design file" for the Polaris3D spherical measuring machine.

The aperture masks for M1 and M2 in the cylindrical coordinates of the optical system are ellipses. But the FTS control system requires a matrix of data to describe the motion of the tool. Each row contains height data at a radius and each column is at an angle. The rows and columns need not be equally spaced, but the matrix must be plaid; that is, all rows (radii) have a data point for each column (angle). Thus Step (7) extends the elliptical apertures to angular segments, shown as the boundaries of the wireframe surfaces in Figure 6. The pole represents the spindle axis for turning the optical system and the two shaded patches are the M1 and M2 mirror surfaces. The origin of the cylindrical coordinate system is (θ=0, r=0); however this is not necessarily the optimal location for the axis of rotation. The (x, y) center of a least squares sphere fit to the system data for the prescan optics has an origin 17 μm from (0,0). In this case,
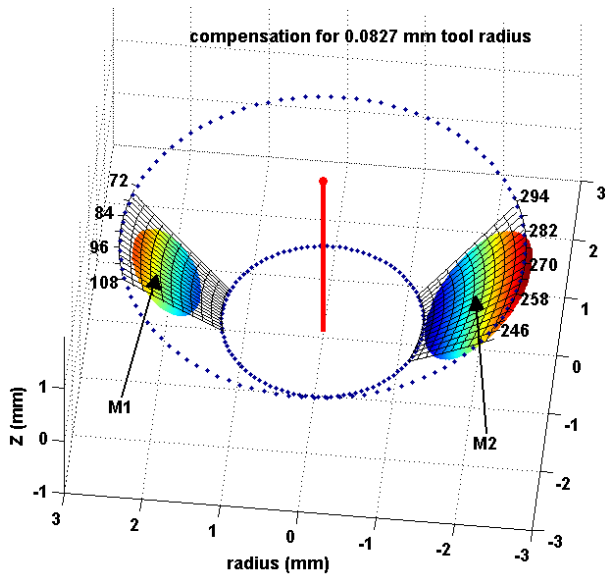
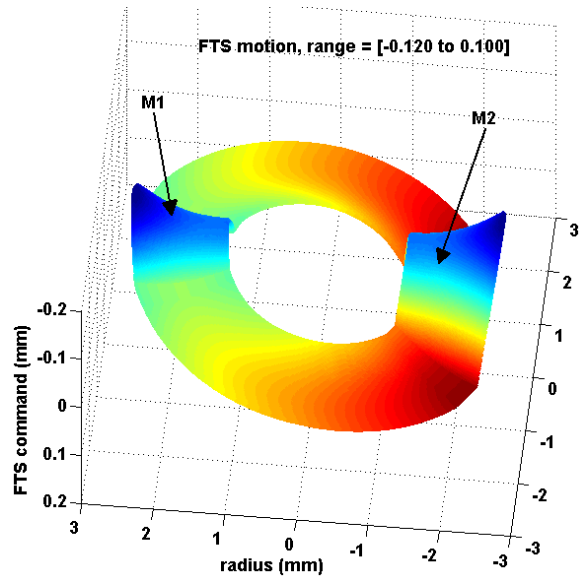**Figure 6.** Optical system with tool radius compensation.

Figure 7. FTS motion for monolithic prescan optics machining.

the FTS excursion is reduced by only a few micrometers by including this additional translation of the mirrors. To reduce the complexity of the system analysis and machining setup the origin was fixed at (0,0). In Step (11), the best fit asphere was found to be very close to conical for this optical system. Figure 7 also shows the effect of tool radius compensation along each meridian on the cylindrical aperture grid. The wire frame overlay gives at the position of the tool center when machining each mirror.

Subtracting the best fit asphere from the radius compensated tool positions shown in Figure 6 gives a table of FTS positions for machining the optical system. These positions are on a fine cylindrical grid with a maximum spacing of 16 µm between grid points. Figure 7 shows the complete FTS tool path within the radial aperture of the mirrors. The required tool excursion is 220 µm. The tool positions are extended 10° to either side of each aperture so that the FTS doesn't abruptly change direction at the edge of the desired clear aperture.

Figure 8. Combined optical system tool path.

The space between the mirrors in the azimuthal direction is a linearly interpolated surface that is added to the asphere swept out by the DTM axes.
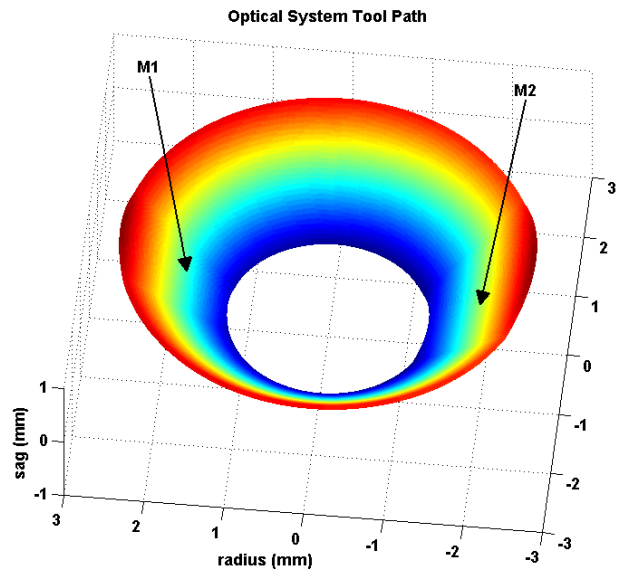
35

The FTS tool motion and the best fit asphere can be added to create the surface shown in Figure 8. This annular surface describes the location of the tool center when machining the prescan optical system.

4.4 RESULTS

The prescan optical system was machined using the FLORA II actuator mounted on the ASG 2500 DTM (see Figure 9). The FLORA II control system was programmed to perform bilinear interpolation over the cylindrical grid of sag values for the excursion shown in Figure 7. The controller positions the tool servo and two counter-balance masses using feedback and feedforward control and thus needs commanded position, velocity and acceleration. The interpolation grid was evenly spaced radii from 1.27 mm to 2.6 mm in increments of 16 µm. The angular spacing was uniform within the mirror apertures at 0.13°, which gives a maximum arc length of 6 µm between points. For this optical system, the best fit polynomial order was set to 1, so the aspheric surface swept out by the DTM was a cone. The cone angle is nearly 45°. The finish pass was cut at 80 rpm with a cross feed of 0.16 mm/min, yielding a feed of 2 µm per revolution. The tool radius was 82.7 µm.
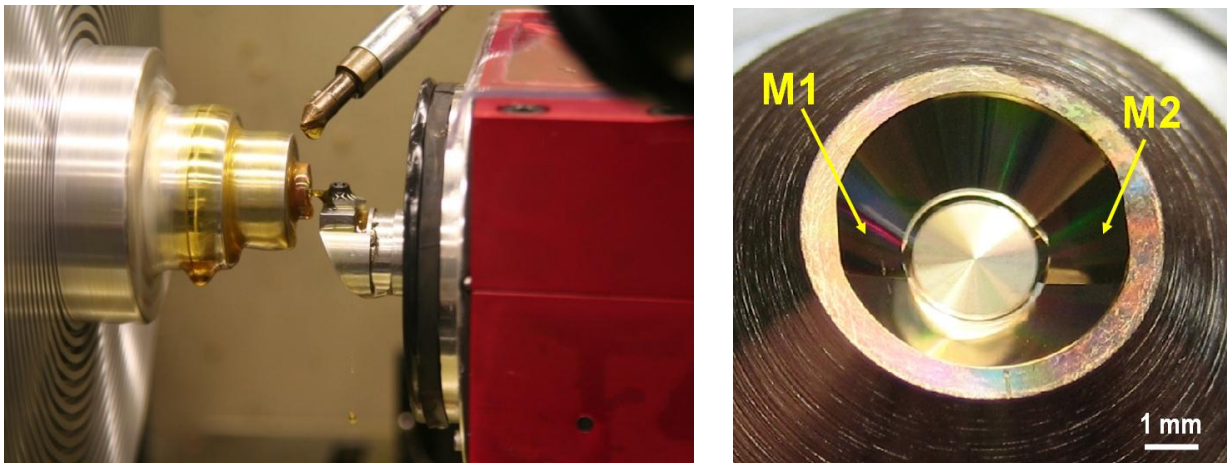

Figure 9. FLORA II machining prescan mirrors (left) and finished part (right).

Interestingly, the surface finish measurement shown in Figure 10 of the M2 mirror shows a repeating pattern at 35 µm which may be print-through from rough machining. While the surface finish is not stunning, 8 nm Ra is quite good considering the high accelerations of the servo at the aperture edges.
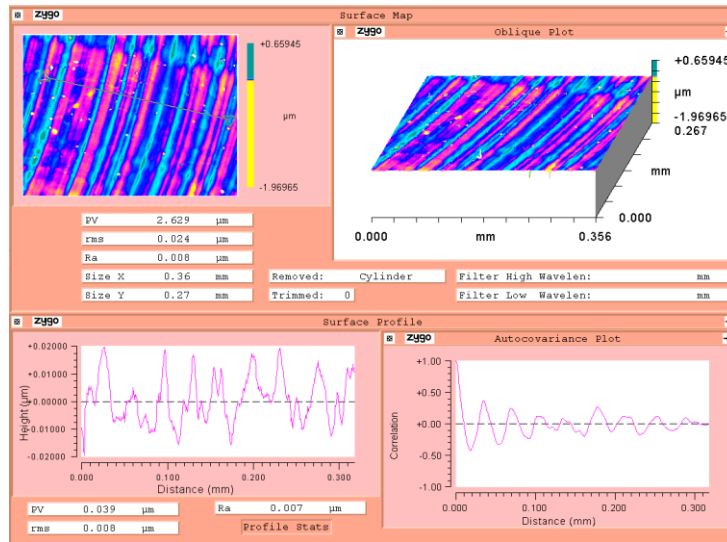
Figure 10. Surface finish measurement with Zygo NewView 5000 of the M2 biconic mirror.

The concave surface shown in Figure 9 was measured on Polaris3D (see Section 1) by parking the rotary table (θ) at +30°, spinning the part at 20 rpms and translating the Z axis (and the part) away from probe. With tracking engaged, the controller moves the R axis to keep the probe focused on the part. This setup allowed the probe to see the flat at the bottom of the part, the conical mirror surfaces and a portion of the upper rough machined flat. The diamond turned center flat is useful for alignment of the optic and to remove tilt before comparing the measurement data with the intended surface shape.

(a)   (b)
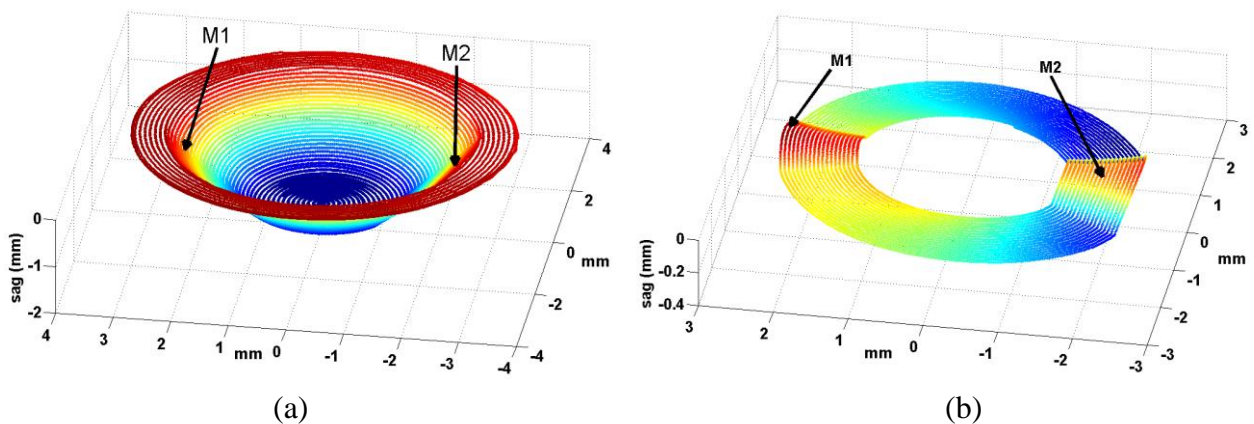
Figure 11. Form measurement of the optical system with Polaris3D. The raw measurement data is shown in (a) and the data after removal of the cone machined by the ASG 2500.

Figure 11 shows the measurement results. Figure 12(a) is a plot of the raw measurement data for the optical system. The 43.87° base cone was subtracted in Figure 8(b) indicating the tool motion away from the cone (toward the center of the part) needed to create the nearly flat mirror

37

surfaces. Figure 12 is a top down view of the error when the measurement is subtracted from the shape of the optical design shown in Figure 5(b). The result is an RMS error of 730 nm with the error largest on the outside and smallest on the inside. The result is a tilt angle that is 5 milliradians more than desired.
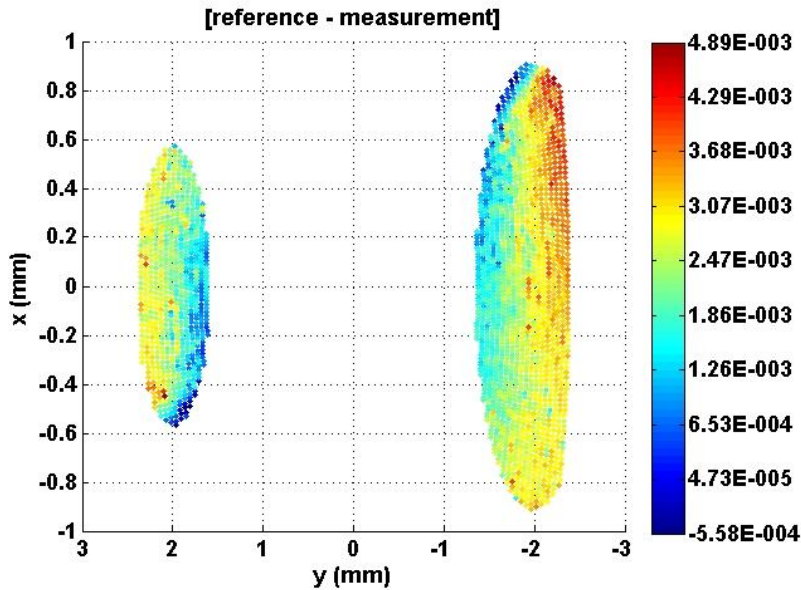
Figure 12. Optical system surface error in the mirror apertures.

4.5 CONCLUSIONS

The design and fabrication for a reflective prescan laser optical system has been completed. Tool path generation for an arbitrary biconic two mirror system has been coded in Matlab. The data tables needed to machine the mirrors with the FLORA II FTS control system are generated by this Matlab code. In addition, a motion program is output describing the best-fit rotationally symmetric asphere that is machined simultaneously by the ASG 2500 Diamond Turning machine. The optical system was machined and measured with Polaris 3D. The significance of the residual tilt angle error on the optical performance of the system has not been evaluated.

REFERENCES

1. Zdanowicz, E., Design of a Fast Long Range Actuator -- FLORA II. Master's Thesis, North Carolina State University, 2009.

2. Garrard, K. Polaris 3D Operation and Control. Precision Engineering Center Annual Report, 27, 27-46, North Carolina State University (2009).

5 FABRICATION AND TESTING OF AN AIR AMPLIFIER AS A FOCUSING DEVICE FOR ELECTROSPRAY IONIZATION MASS SPECTROMETRY

Guillaume Robichaud
Graduate Student
Thomas Dow
Dean F. Duncan Distinguished Professor
Department of Mechanical and Aerospace Engineering
Alex Sohn
Precision Engineering Center Staff

Mass spectrometry is an analytical method used to identify molecule and complex protein based on the ration of their mass and the number of charge they carry when measured. Application and use of mass spectrometry has been growing extremely fast during the last decade. It is currently extensively used in analytical chemistry, cancer research, drug testing, explosive detection, etc. To be measured, molecules first have to be transferred into gas phase and ionized. A technique of obtaining gas phase ion that has revolutionized mass spectrometry is called electrospray ionization, where gas phase ions are extracted from a solution flowing in a thin capillary using a powerful electrical field. However, it is estimated that less than 1% of ions generated by an electrospray ionization source will be sampled by the mass spectrometer. This is mainly due to the low transfer efficiency of ions between electrospray source and the instrument inlet. Through the joint effort of precision engineering and computational fluid dynamics, an aerodynamic ion focusing device has been designed and fabricated using a single point diamond turning machine. Several tests have been performed to evaluate the performances of the device.
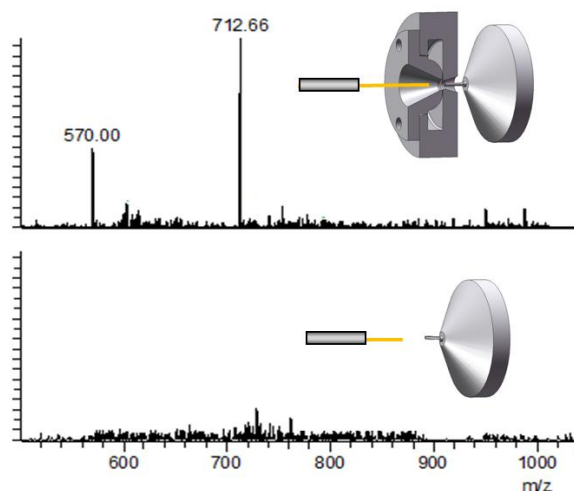
5.1 INTRODUCTION

Mass spectrometry is an analytical technique widely used in biochemistry to characterize and identify molecules and proteins. It is a fast growing science and plays a critical role in cancer and proteomic research. Modern mass spectrometers use electric or magnetic fields to differentiate gas phase molecules according to the relation between their mass and charge (m/z)[1]. The molecules of interest (analyte) are often in solution and therefore need to be transferred to gas phase and charged prior to be captured by the mass spectrometer. One of the preferred methods is the electrospray ionization technique (ESI) [1]. ESI-MS was developed by Yamashita and Fenn at Yale in 1984 [2] and allows a wide range of molecule size to be transferred directly to gas phase in line with the spectrometer. ESI is that it is a very soft ionization technique, meaning that energy added to the molecule is relatively low, allowing large molecules such as proteins to be transferred into gas phase without fragmenting. ESI-MS consists of a small capillary tube through which flows an analyte diluted in a buffer solution containing solvent and a small percentage of formic acid (charges). The intake needle of the mass spectrometer is positioned a few millimeters from the capillary exit and an electrical potential between the capillary and the mass spectrometer needle is applied as shown in Figure 1. The resulting electrical field will cause a thin jet of highly charged solution to be ejected from the ESI tip, from which gas phase ions will eventually arise as solvent evaporates. Creation of singular ions during electrospray depends upon a complex interaction between the size of the analyte molecule, the flow rate, the nature of the solvent, the intensity of the electrical field, the concentration of the analyte in the solvent and the temperature. However, the efficiency of the ESI-MS does not only depend on the ability to create gas-ions from liquid analyte but also greatly depends on the efficiency of the transmission of these ions to the mass spectrometer. It is estimated that less than 1% of the ions produced will be sampled by the mass spectrometer. Most of the loss is encountered during the transfer between the ESI capillary and the MS inlet, as ions of same polarity will be scattered by repulsive Coulombic force before they can reach the inlet of the mass spectrometer.

---

[1] The dimensionless mass-to-charge ratio (m/z) is used to characterize the mass spectrum, where m is the unified atomic mass (in Dalton) and z is the number of elementary charges.
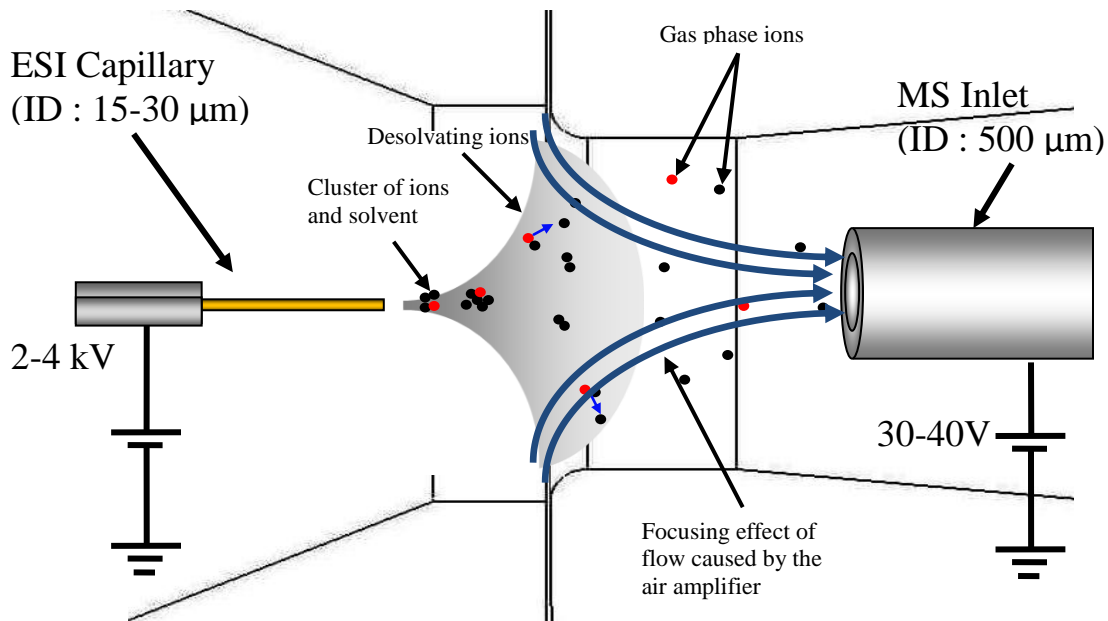
Figure 1. Electrospray Ionization with Air Amplifier

Efficiency of ESI-MS is critical because the size of the sample to be analyzed in applications such as medical research or forensics can be limited. Improving the efficiency or the sensitivity of the ESI-MS would lower the detection limit or the minimum sample size needed. This section addresses the design, fabrication and testing of a precision engineered air amplifier to aerodynamically focus the scattering ions toward the mass spectrometer inlet to increase the number of ions captured. It involved faculty and staff in mechanical engineering studying fluid flow and design/fabrication as well as faculty and staff in chemistry to study the efficiency in MS experiments.

5.2 THE AIR AMPLIFIER

Proof of concept showing signal improvement using an air amplifier has been made using a crude commercial device [3-6]. It was found that imprecise gap control and misalignment were impacting the performance and repeatability of the results. The Computational Fluid Dynamics Lab worked together with the Precision Engineering Center to develop an aerodynamic profile that provided suitable fluid flow and was suitable for fabrication. The first calculations of the gas dynamics of the flow within the air amplifier devices has been performed using an in-house computational fluid dynamics code called REACTMB. The air amplifier uses the Coanda effect[2] in order to create a low pressure zone that enables air entrainment into the air nozzle and eventually focus the ions that are generated by electrospray ionization into the mass

---

[2] Tendency of a fluid to stay attached to an adjacent curved surface

spectrometer, increasing the sensitivity of the instrument. Images from CFD model (Figure 2) shows the velocity profile of the pressurized N_2 curved by the Coanda effect (left) as well as the focusing effect on the electrosprayed ions (right).
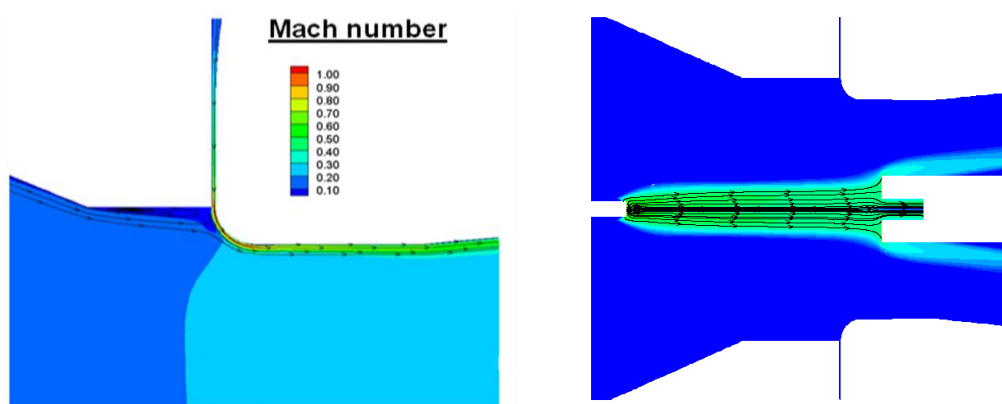
Figure 2. Aerodynamic model of the air amplifier (Left: Coanda profile. Right: Stream lines.)

5.2.1 1ST ITERATION OF AIR AMPLIFIER

According to the CFD model, the ideal annular gap was in the range of 50-70 µm and to ensure a uniform and radially symmetrical flow, the annular gap faces had to be parallel to < 1 µm. In addition, the surface finish of the Coanda surfaces had to be smooth and radially symmetric. Because the optimal annular gap was to be set experimentally, the first iteration of the air amplifier had an annular gap that can be modulated from 50 µm to 70 µm with three piezoelectric actuators illustrated in Figure 3.
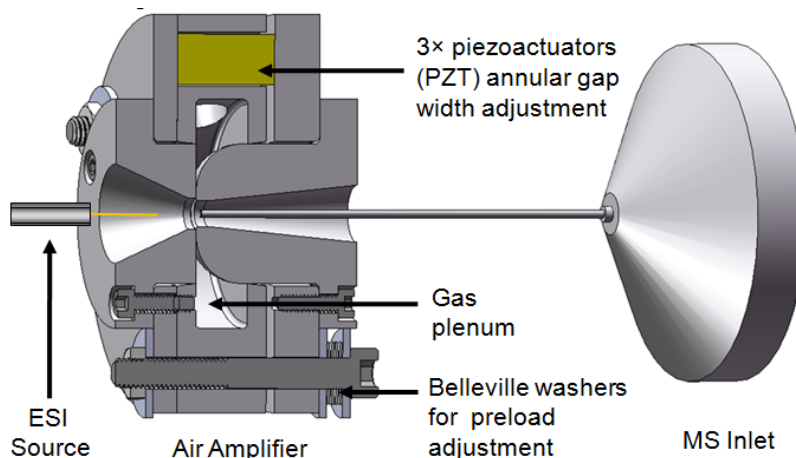
Figure 3. Section view of the 1st iteration of the air amplifier.

42

When high pressure air is introduced to the gas plenum, the air amplifier created a Venturi effect and static pressure has been measured along the flow axis for different pressure and annular gap position using a pitot tube. The minimum static pressure was measured 1 mm downstream of the annular gap, revealing the existence and location of a focal point. Moreover, increasing the annular gap width had the same effect on the flow profile as increasing the plenum pressure.

Several mass spectrometry experiments were performed to evaluate the effect of the air amplifier on the signal abundance. On a mass spectrum, signal abundance is reported for each m/z value and is proportional to the number of ion detected for that range. Signal abundance is often reported in term of the relative abundance or the percentage of the most abundant ion. Absolute abundance is dimensionless and depends on parameters specific to the instrument. Absolute abundance is a valid figure of merit to compare sets of measurements taken on the same instrument under different operating conditions – such as with and without the air amplifier. To systematically explore the experimental space defined by the many variables that can affect the performance of the air amplifier (position, plenum pressure, annular gap width, solvent composition, ESI voltage, etc), fractional factorial design was used to find the significance of each. The results showed that signal improvement could not be obtained under all condition but were significant at higher solvent flow rates and larger ESI capillary tips (up to 34 folds of improvement in this case [7]).

5.2.2 2ND ITERATION DESIGN AND FABRICATION

Based on the results of the first design, a second design of the air amplifier has been fabricated. The objectives were to reduce the cost and to make the device more compact; that is, to reduce as the length of the mass spectrometer inlet tube (see Figure 4). A longer capillary tube decreases significantly the efficiency of the ion transfer in the mass spectrometer as the opportunity for ions to collide and neutralize with the capillary increases. As desolvation of ions in gas phase typically continues in the MS inlet tube (typically kept at 200-250 ℃), another hypothesis suggest that the cooling of the ions in the extended capillary tube could slow down the desolvation process and therefore reduce the number of gas phase. Also, a less expensive and more compact air amplifier is now possible since it was demonstrated that the piezoelectric actuators are not necessary.
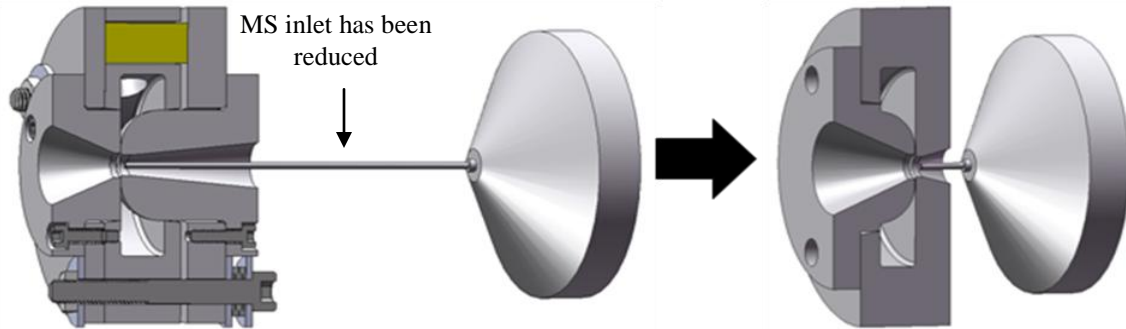
43

Proprietary Release subject to the terms and conditions of the Precision Engineering Center Membership Agreement

and North Carolina State University Office of Technology Transfer nondisclosure agreements.

Figure 4. Reduction of MS inlet tube length

As in the first design, the CFD model was used to test different aerodynamic profiles and different configurations. Since there was no indication that a change in the Coanda profile would result in significant signal improvement, aerodynamic outline of the Coanda profile and annular gap remained unchanged. Only the length of the inlet and outlet cones would change to allow a shorter MS inlet tube. A CFD model was also used to verify the effect of these changes in geometry on the signal and also how close the air amplifier could be positioned with respect to the MS inlet before starting to obstruct the flow. With the new design, it will now be possible to reduce the MS tube length by up to 80% (134 mm to 23 mm). Also, new design only has one insert, such that the outlet cone is now machined directly in the base plate. Not only does this also allow a shorter outlet cone,, but it also eliminates the risk associated with the misalignment of that insert. To keep the plenum size the same, the upstream cone length had to be extended. Observation of pitot tube measurement performed on the first iteration indicated that the length of the upstream (intake) cone had little influence on the air flow profile. This hypothesis was also confirmed by the CFD model. Extensive work has been made by the AECFD laboratory to include the charged particles in the model so that ion abundance can be predicted. The model did not predict a significant drop in abundance due to the shorter outlet cone. However, the charged particle model had not been fully validated at this time so it was decided to fabricate an air amplifier that had removable outlet cone sections so that effect of cone length can be determined experimentally.
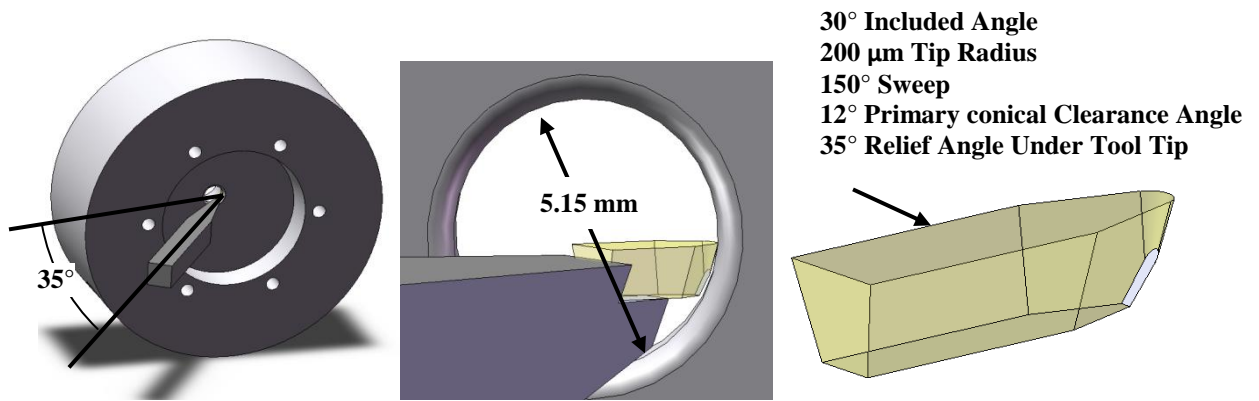
30° Included Angle
200 μm Tip Radius
150° Sweep
12° Primary conical Clearance Angle
35° Relief Angle Under Tool Tip

Figure 5. Simulation used to design custom made diamond tool and determine tool setup

In the second iteration of the air amplifier the Coanda radius is machined directly in the base of the device as shown in Figure 5. As access to this radius is limited, a custom diamond tool had to be designed and machining simulation had to be performed using Solidworks® to ensure that there would not be any interference between the tool holder and the part during machining of the Coanda radius. Also shown on this figure, the tool was required to have a small included angle and a large sweep angle to be able to machine the entire radius (90°) and also reach the back of the bore. The clearance under the tool tip also had to clear the lower part of the tool while machining the 5.15 mm OD. Additional lapping was required to create a relief angle under the tool to ensure that this clearance was achieved. In the first iteration, because of the presence of the piezoelectric actuators that had to be installed and shimmed, the final height of the insert that set the annular gap had to be measured using a coordinate measurement machine (CMM). In this case, the tool position given by the axis encoder of the diamond turning machine has been used to measure precisely the part heights and set the annular gap to 50 μm.

5.2.3 SECOND ITERATION TESTS

Static pressure measurements for the second iteration of air amplifier were performed using a compound pressure transducer with a range of ±5 psig (±5 V) together with a LVDT for position measurement. With this setup it was possible to measure with greater resolution and accuracy the static pressure as a function of the position in the air amplifier. In a first series of measurements, the static pressure profile was measured for different cone lengths. Results are presented in Figure 6. First, it can be observed that the location of the focal point remains relatively unchanged (1-2 mm downstream of the annular gap) for different cone lengths. It can also be observed that the minimum pressure (maximum vacuum) decrease significantly as the cone length decreases. This phenomenon limiting the minimum cone length had been predicted by the CFD models. It is caused by recirculation of air that creates back pressure interfering with the flow in the air amplifier. This back pressure can be seen clearly in figure for the measurements performed with cone length of 11.85 mm and 17.85 mm.

45
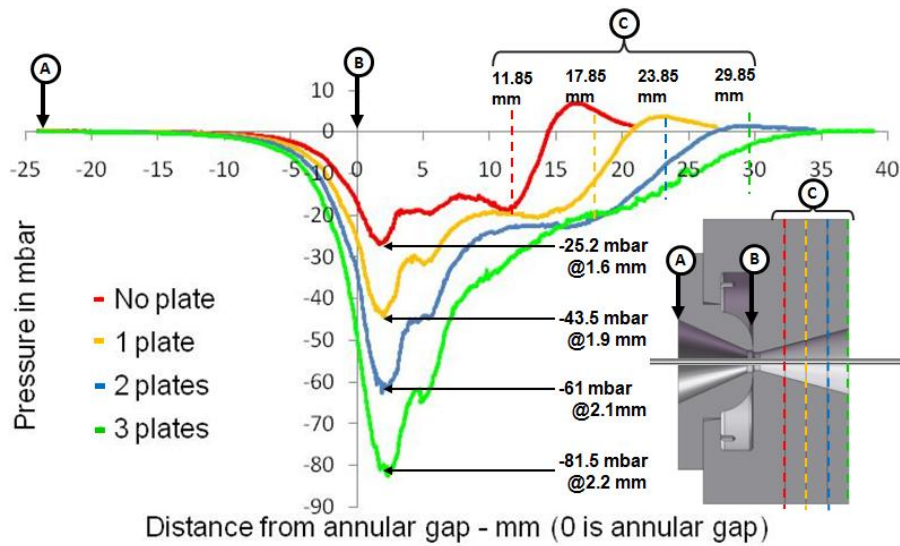
Figure 6. Static Pressure Measurement for 2nd iteration of air amplifier

One of the major issues with the commercial air amplifier that was used in previous experiments was the lack of radial symmetry of the air flow caused by its threaded annular gap adjustment that offered limited annular gap width control and poor parallelism. A non-radially symmetric air flow affects the capability of obtaining a precise and consistent aerodynamic focal point. To measure the symmetry of the flow, stagnation pressure has been measured at 1 mm from the outlet of the air amplifiers along the vertical and horizontal axis. These measurements have been performed on both the new precision engineered air amplifier and the threaded commercial version. 3D plots of the stagnation pressure as a function of the radial position are presented in Figure 7, where 0 mm is the central axis of the air amplifier. A significant improvement in radial symmetry can be observed.

Figure 7. Stagnation pressure measured 1 mm from commercial air amplifier outlet.

5.2.4 LTQ-FTMS TESTS

The LTQ-FTMS used for this series of experiment is a tandem mass spectrometer, meaning that it actually consist of two mass spectrometers in series. Only the front LTQ mass spectrometer was used for these experiments to minimize the possible signal loss caused by the internal ion transport. As mentioned earlier, one of the principal motivations for designing a second iteration of the air amplifier was to reduce the length of the MS inlet tube. A first experiment was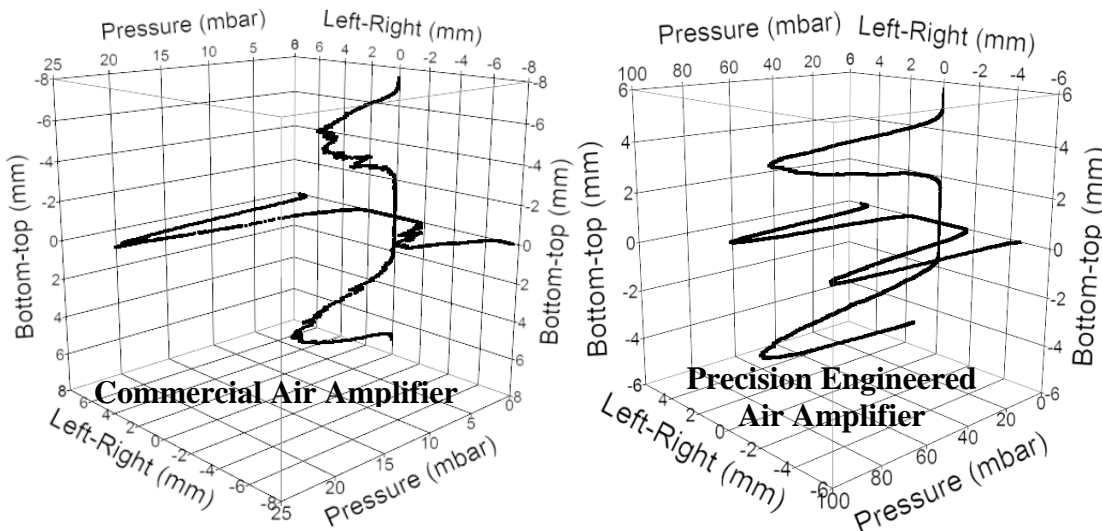 performed to quantify the signal loss due to the extended capillary alone. To do so, signal was collected with both the regular 3 mm MS inlet and the extended 43 mm inlet (no air amplifier) under the same conditions. Ion abundance decreased by about 3 folds when using the extended MS inlet of 43 mm is used.

The 43 mm MS inlet length is only necessary if all air amplifier cone lengths are used. If cone extension lengths are removed, the MS inlet extended length can be reduced to 23 mm. It was already shown in previous section that outlet cone length had a significant impact on the flow inside the air amplifier.

To quantify the effect of the air amplifier on the ion abundance, measurements were performed under the exact same conditions, varying only the cone length of the air amplifier. As it can be seen in Figure 8, reducing the air amplifier cone length does not reduce the air amplifier signal. For that reason, the remaining of the experiments will be performed without the cone length extension (total cone length of 11.85 mm) and the mass spectrometer inlet extension of 23 mm.
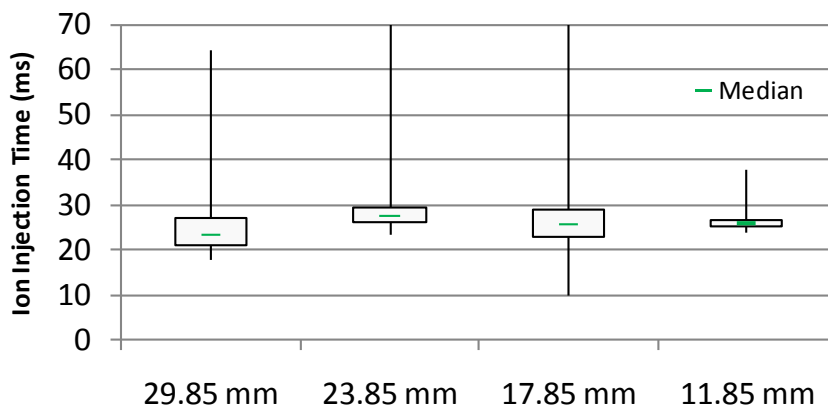
Figure 8. Ion injection time as a function of air amplifier cone length

As mentioned earlier, one of the hypotheses to explain signal loss due to an extended capillary was the impact that the non heated capillary could have on the desolvation of the analyte. In order to test this hypothesis, a wire element was used to generate additional heat to the extended capillary as shown in Figure 9.
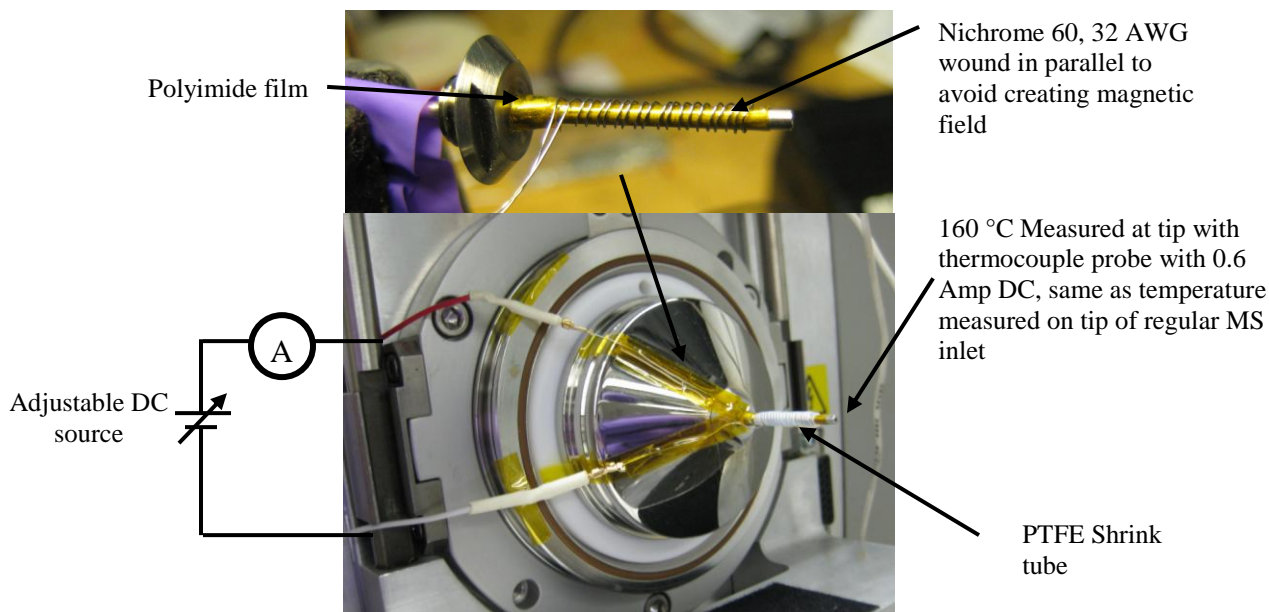
Figure 9. Experimental setup to heat MS inlet capillary

Several experiments have been performed with different heat inputs and results showed that no additional improvement could be obtained by heating up the capillary as shown in Figure 10. Results actually showed a slight loss in signal when additional heat was applied. If analyte is already completely dissolved, providing additional heat energy to the molecule will cause

48

additional analyte fragmentation. A trivial solution to resolve this issue would be to reduce further the length of the MS inlet capillary with the air amplifier to minimize the opportunity for ions to neutralize.
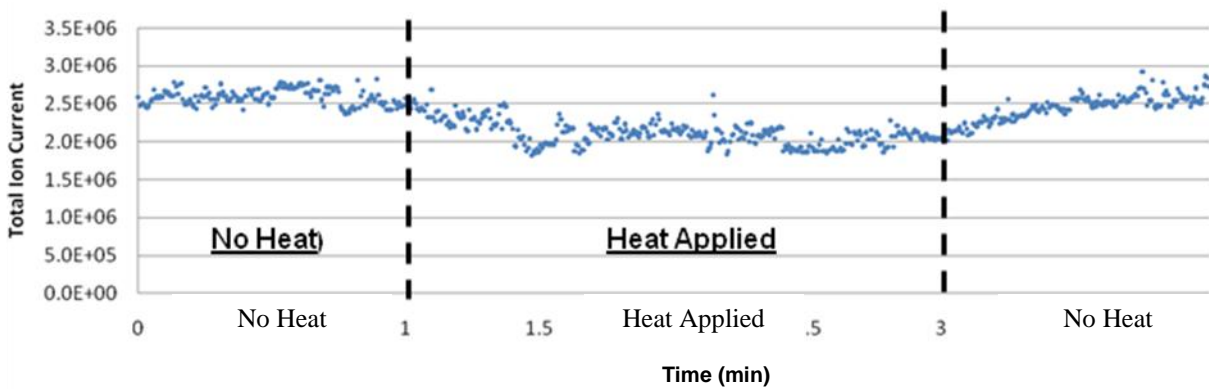
Figure 10. Effect of extended capillary temperature on ion abundance

Full factorial design experiments have been performed to validate the results found with the first iteration of the air amplifier and explore additional experimental space (smaller ESI gaps). Experiments were performed with 500 nM concentration Cytochrome-C (equine) in a 100% H_2O / 0.2% formic acid buffer. The purpose was to verify the effect of the following variables: the ESI gap (1-3-6 mm), the flow (1-2 µL), the presence of the air amplifier (ON-OFF) and the ESI capillary size (30-100 µm). The different combinations tested are presented in Table 1. Note that experiments have been performed in a random sequence. Results are presented in Figure 11.

Table 1. Full factorial performed on the second iteration of the air amplifier

	ESI gap (mm)	Flow (µL/min)	AA	cap size (µm)		ESI gap (mm)	Flow (µL/min)	AA	cap size (µm)
1	1	1	Off	30	13	1	2	Off	100
2	1	2	Off	30	14	1	1	Off	100
3	3	1	Off	30	15	3	1	Off	100
4	3	2	Off	30	16	3	2	Off	100
5	6	1	Off	30	17	6	2	Off	100
6	6	2	Off	30	18	6	1	Off	100
7	1	2	On	30	19	1	1	On	100
8	1	1	On	30	20	1	2	On	100
9	3	1	On	30	21	3	1	On	100
10	3	2	On	30	22	3	2	On	100
11	6	2	On	30	23	6	2	On	100
12	6	1	On	30	24	6	1	On	100

Figure 11. Full Factorial Design experiment results (sum of 19^+, 9^+ and 8^+ of Cyt-C)

Those results are in accordance with what was discovered with the first iteration of the air amplifier, i.e. that very little improvement was obtained with 30 µm ID ESI capillary. On the other hand significant improvement is also obtained at 100 µm ID ESI capillary, where no signal can be o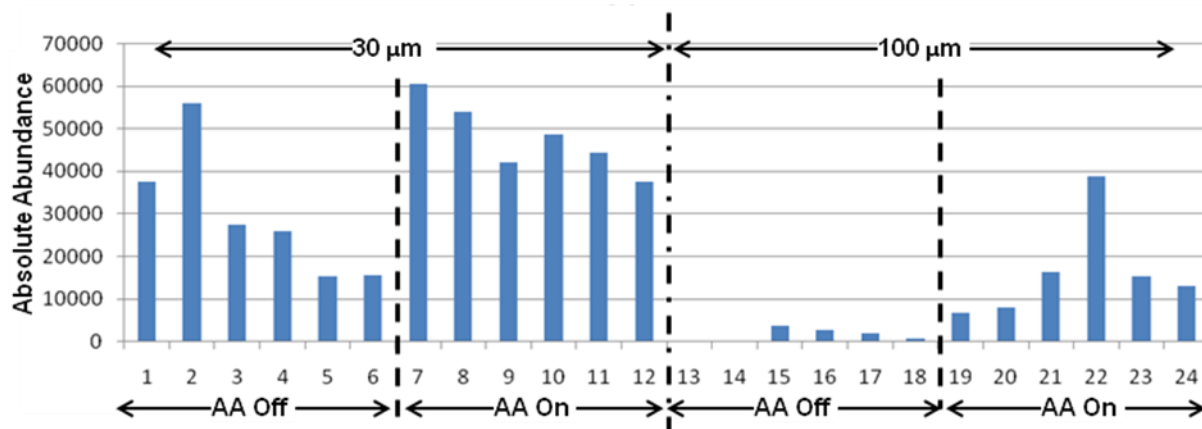btained without the air amplifier. This signal improvement at larger tip opens the door to electrospray at higher flow as maximum flow in a 30 µm capillary is 3 µL/min and flow as high as 10 µL/min are possible with the 100 µm capillary tip. However, the greater is the flow rate, the larger is the radius (r) of initial droplets formed during electrospray as showed by the following equation (1) where ρ is the fluid density, Q is the flow rate and γ the surface tension of the fluid.

$$r \propto \left(\rho Q^2 \gamma\right)^{\frac{1}{3}} \tag{1}$$

This increase in initial droplet size signifies that more desolvation is necessary for the droplet to release their gas phase ions. Therefore, even if an increase in flow means that more analyte is electrosprayed for every unit time, it will not necessarily translate into a stronger signal if the desolvation is not complete. To further explore this experimental space and show the effect of air amplifier on desolvation, ion abundance as a function of flow rate was measured at 2 different ESI distance (3 mm and 6 mm). As seen in Figure 12, an increase in flow rate at 3 mm does not translate into an increase in abundance. On the other hand, results at 6 mm ESI gap show that total ion current still increase linearly with flow rates up to 9 µL/min (maximum stable flow obtained with 100 µm tips). We expect signal to be lower as ESI distance increases, however increase in desolvation at larger ESI distance assisted by the air amplifier eventually compensate for the losses resulting from the greater ESI distance. These results confirm the effect of the air amplifier on the desolvation of the ions.
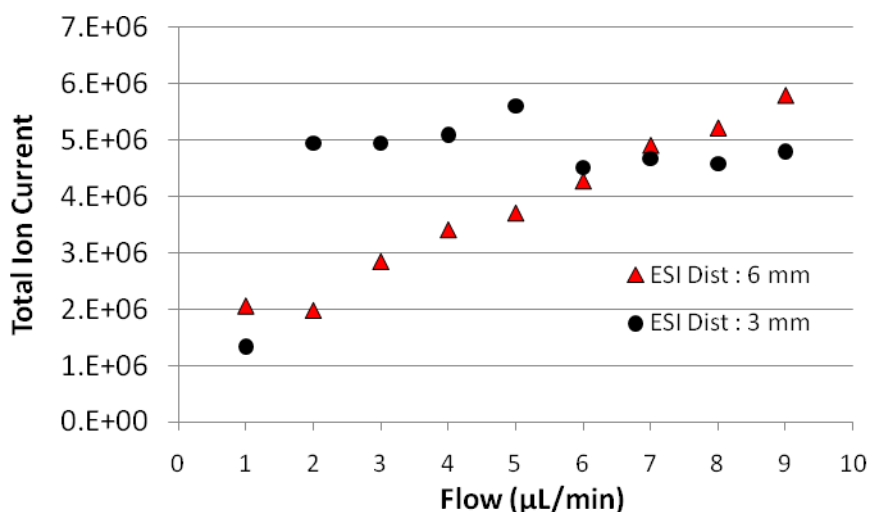
Figure 12. Total Ion Current as a function of flow rate at 3 mm ESI gap

5.3 CONCLUSIONS

A new iteration of the air amplifier has been designed and fabricated with a fixed annular gap of 50 μm and a shorter outlet cone to reduce signal losses caused by the extended capillary. Using fractional factorial design, variable having an impact on the performance of the air amplifier have been identified. The experimental space where the air amplifier is offering the best performance has been identified and significant signal improvement is obtained when using the air amplifier with larger electrospray capillary tip and 100% H2O buffer solvent composition. These results support the hypothesis that air amplifier does not only focus the ions but also helps with the desolvation of the droplets. Additional experiments were performed to support this hypothesis.

Although the air amplifier will not provide overall signal improvement under every condition of utilization, this work showed that it remains a valid approach to increase ions abundance at larger ESI distance. Therefore W.M. Keck FT-ICR MS laboratory is considering using the air amplifier in one of their application that requires larger ESI distances.

REFERENCES

1. Nadja, C. and Christie, E., "Practical Implications of Some Recent Studies in Electrospray Ionization Fundamentals", Mass Spectrometry Reviews, Vol 20, pg 362-387, 2001.
2. Yamashita, M. and Fenn, B, "Electrospray Ion Source. Another Variation on the Free Jet Theme", The Journal of Physical Chemistry, Vol 88, No 20, pg 4451-4459, 1984.
3. Hawkridge, A. M., Zhou, L., Lee, M. L., Muddiman, Analytical performance of a venturi device integrated into an electrospray Ionization Fourier transform ion cyclotron resonance mass spectrometer for analysis of nucleic acids D. C., Anal. Chem. 2004; 76: 14, 4118-4122
4. Yang, P. X.; Cooks, R. G.; Ouyang, Z., Hawkridge, A. M.; Muddiman, D. C., Gentle Protein Ionization Assisted by High-Velocity Gas, Flow Anal. Chem. 2005; 77, (19), 6174-6183
5. Dixon, R.B., Hawkridge, A.M., Muddiman, D.C., Probing the Mechanisms of an Air Amplifier Using a LTQ-FT-ICR-MS and Fluorescence Spectroscopy, J. Am. Soc. Mass Spectrom. 2007; 18: 11, 1909-1913
6. Dixon, R.B., Muddiman, D.C., Quantitative comparison of a flared and a standard heated metal capillary inlet with a voltage-assisted air amplifier on an electrospray ionization linear ion trap mass spectrometer Rapid Commun. Mass Spectrom. 2007; 21: 19, 3207-3212
7. Robichaud G. et al., Design, Modeling, Fabrication, and Evaluation of the Air Amplifier for Improved Detection of Biomolecules by Electrospray Ionization Mass Spectrometry, Int. J. Mass Spectrom. 2010; in press

6 EFFECTS OF VARYING EVAM PARAMETERS ON CHEMICAL TOOL WEAR

Brandon Lane
Graduate Student
Thomas Dow
Professor, Department of Mechanical and Aerospace Engineering
Ronald Scattergood
Professor, Department of Materials Science and Engineering

Studies have shown the benefits of applying micrometer scale vibration motion of a diamond tool during precision diamond turning (DT). Reported benefits include a decrease in machining forces and consequent wear of the diamond tool. Despite more than two decades of elliptical vibration-assisted machining (EVAM) research, few have addressed the relationships between EVAM parameters and tool wear. A chemical tool wear model is further developed in this paper that relates conventional DT tool wear to machining temperatures obtained from finite element modeling (FEM). This temperature dependant wear model is then applied to FE simulations of EVAM that vary workpiece speed, frequency, and ellipse shape. EVAM experiments varying frequency were then conducted and surface finish and tool wear were measured. Optical surface finish was achieved on a low carbon steel workpiece, but tool edge measurements showed comparable wear to conventional DT. Relationships between wear models, FE models, and experiment results are discussed.
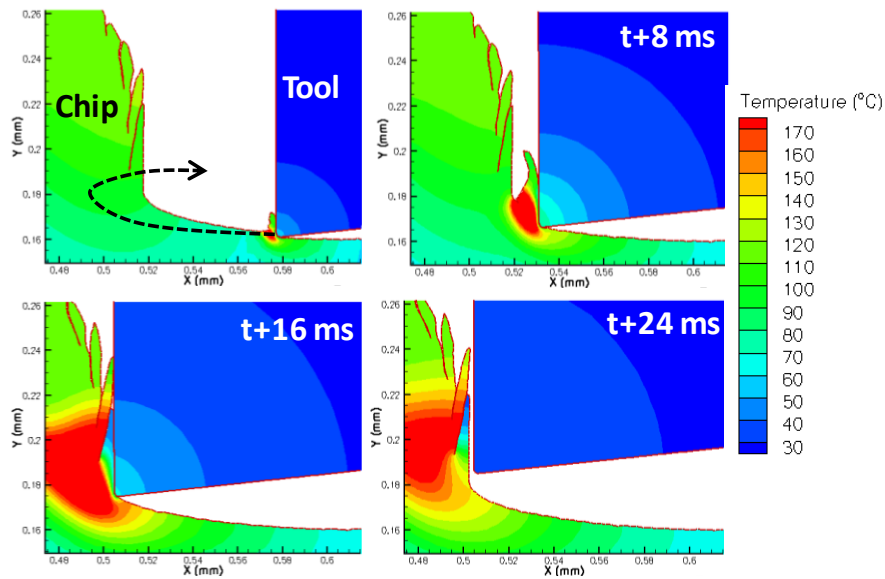
6.1 INTRODUCTION

Studies [1] have shown the benefits of applying micrometer-scale elliptical vibration (EVAM) motion to a tool during diamond turning (DT). In this process, the tool comes out of contact with the workpiece over part of each cycle. Reported benefits include a decrease in machining forces, tool temperatures and wear of the diamond tool. The particular causes for decrease in force and wear using EVAM depend, to some extent, on the general lack of understanding of tool wear mechanics of a normal DT operation. The research discussed here will provide insight into EVAM cutting mechanics and create the necessary foundation for future industrial implementation.

A baseline understanding of tool wear for standard (non-vibration) DT is necessary before proceeding with EVAM wear studies. Correlation of diamond tool wear with standard models allows different workpiece materials or chemical processes to be evaluated. Paul and Evans [2] studied the chemical aspects of diamond tool wear. They theorized that the volumetric wear rate would follow the Arrhenius equation:

$$\frac{dV}{dt} = A \exp\left(\frac{-E_a}{RT}\right) \tag{1}$$

Where V is the worn volume, R is the gas constant (8.3144 J/mol), and T is process temperature (K). A and E_a, the pre-exponential constant and activation energy, are empirical constants specific to the interacting materials. The wear rate dependence on temperature is the same function for chemical reactions or diffusion [2], though individual process contributions are not considered here.

To find the empirical constants, tool wear and tool temperatures must be determined. To measure the tool wear, a process called Electron Beam Induced Deposition (EBID) [3] has been developed and a finite element tool cutting model is used to estimate the tool temperature.

EBID is performed in a scanning electron microscope (SEM) by creating a hydrocarbon line on the diamond tool perpendicular to the cutting edge. This line provides the contrast needed to measure the edge and create a 2D worn profile. If orthogonal cutting is conducted with a straight-edged tool, the worn volume can be estimated as the 2D worn area multiplied by the workpiece width. Because the EBID process requires costly time on the SEM, a technique using a scanning white light interferometer (SWLI) was developed that allows rapid wear land measurements in addition to the more precise EBID measurements [4].

The second input needed is the local tool temperature. Since this is nearly impossible to measure, a finite element (FE) cutting model was used to estimate the tool/workpiece temperatures. AdvantEdge, developed by ThirdWave Systems, provides the forces and temperatures necessary to complete the Arrhenius model for tool wear.

The EVAM cutting process depends on several input parameters. While the effects of varying speed, frequency, and/or ellipse shape on surface finish and tool forces have been studied [5], the potential effects on thermally motivated tool wear have not. An elliptical tool vibration routine was recently added to AdvantEdge to assist in this endeavor. EVAM simulations varying workpiece velocity, tool frequency, and ellipse shape were completed and tool temperatures and forces were measured. The temperatures were then supplied to the Arrhenius wear model. Average wear rates were determined with respect to varying EVAM parameters. This provides relationships between the EVAM parameters; specifically workpiece velocity and tool frequency, and their potential consequences to chemical/diffusive tool wear.

Cutting experiments varying EVAM frequency were conducted and tool wear was measured using the EBID method. EVAM tool wear is compared against those measured from conventional machining experiments and wear vs. frequency results are compared against those found from finite element and chemical wear models. Surface finish is also measured and compared against conventional machining results. Conclusions are drawn regarding the observed rates of wear, their relationship to FE models, and the optical quality surface finish measured after EVAM of steel.

6.2 CONVENTIONAL MACHINING ON ST1215

A previous report [6] gave the results of conventional machining and tool wear experiments on St1215. The machining, wear measuring, and FE modeling process for these experiments resulted in estimated Arrhenius wear coefficients $2.894*10^{11}$ μm^3/sec for the pre-exponential constant A, and the activation energy E_a as 67.973 kJ/mol. These values, however, were determined from 2 data points determined from machining experiments at 2 different machining speeds (1.04 and 4.24 m/s). Another experiment at a 3rd speed was conducted for a better measure of Arrhenius constants and is described in this section.

6.2.1 EXPERIMENTAL SETUP

To create the orthogonal cutting conditions, fins were machined into a 4" diameter cylinder of St1215. The fins were 1.2 mm wide and the straight-edged diamond tool (supplied by Chardon Tool) was 2.1 mm wide. This creates a localized section of wear on the tool, shown in Figure 1. One steel fin was machined at 1 μm depth of cut at 2.12 m/s on a 3-axis Nanoform 300 diamond
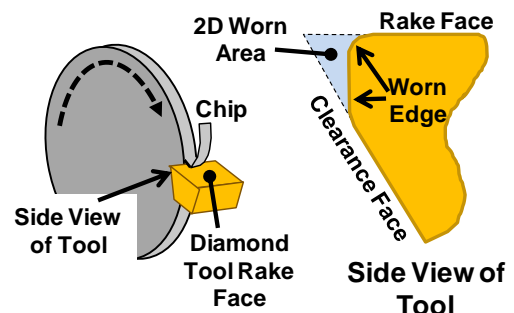

Figure 1. Schematic of orthogonal machining St1215 experiments and measured 2D worn area.

turning machine with a continuous stream of Mobilmet Omicron cutting fluid and compressed air to remove the chips. After machining a certain distance (typically 20 m), the tool was removed and cleaned. A 5% nitric acid solution was used to remove any pickup incurred while machining. The worn edge of the tool was examined via SWLI or a combination of SWLI and EBID [3,4,6]. This process was repeated for successive machining distances, and volumetric wear loss as a function of time was acquired.

Multiple FE simulations of different machining speeds were run when determining the first 2 data points for the Arrhenius wear model [6]. These included a temperature value for the 1 μm depth of cut and 2.12 m/s machine speed conditions conducted to determine the mid-speed data point.

6.2.2 THREE POINT ARRHENIUS WEAR MODEL RESULTS

Wear rates from conventional machining experiments were combined with maximum tool temperatures from FE simulations to create an Arrhenius plot shown in Figure 2. Three points are shown; one for each machining speed. Apart from the least-squares linear fit, a high estimate and low estimate line are shown. Though the three points did not show a linear trend, a range of Arrhenius empirical constants are suggested and given in Table 1.
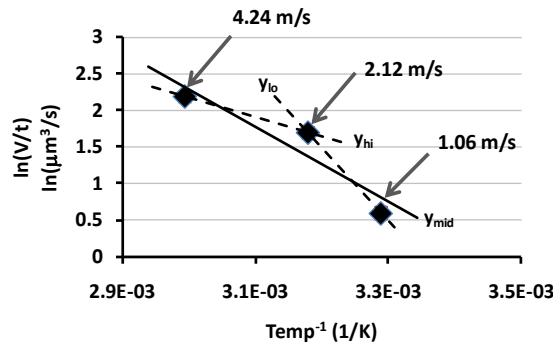
Figure 2. Arrhenius plot of measured diamond tool wear rate and peak tool temperatures from FE simulations at three machining speeds.

Review of several studies [2] indicated activation energy estimates from 80-300 kJ/mol for catalytic metal-on-metal reactions or graphitic carbon diffusion into various metals. The lower E_a determined in Figure 2 and Table 1 is likely a result of constant tool contact with new, untouched workpiece material during the cutting process.

Table 1. Arrhenius constants from slopes in Figure 2.

Line in Figure 2	Activation Energy, E_a	Pre-exponential Constant, A
y_{hi}	83.5 kJ/mol	4.08×10^{14} $\mu m^3/s$
y_{mid}	42.5 kJ/mol	4.5×10^7 $\mu m^3/s$
y_{lo}	22.1 kJ/mol	2.52×10^4 $\mu m^3/s$

56

6.3 EVAM SIMULATIONS

The EVAM machining process is much more complicated than conventional machining. Tool temperatures never fully reach a steady state, but give a cyclic rise and fall while the tool comes in and out of contact with the workpiece. Again, tool temperatures are nearly impossible to measure experimentally for conventional cutting, let alone EVAM, but can be estimated with FE modeling. A new elliptical tool vibration mode in AdvantEdge was developed by ThirdWave to assist this project. Figure 3 shows an example of temperature results from an EVAM simulation. Maximum tool temperature and X (cut) and Y (thrust) components of tool force vs. time can be extracted. Results may show how machining parameters minimize tool wear and optimize surface finish and/or machining speed.

6.3.1 DATA HANDLING AND WEAR CALCULATION

AdvantEdge simulations use a variable time step size in the time integration algorithm. Though total simulation times are small ($< 5x10^{-3}$ sec for EVAM frequencies above 10 kHz), time steps are on the order 10^{-11} sec. This generates tool force and temperature data files in excess of 400 Mb. Normally, AdvantEdge uses TecPlot to plot and observe simulation data. Large data files require TecPlot to interpolate data with a high order polynomial. This allows TecPlot to update plot displays quickly, but detail is lost in the force and temperature data. A Matlab script was created that reads in the AdvantEdge datafile and allows the user to subsample the data at a specified step size. Figure 4 shows a comparison of force data from an AdvantEdge EVAM simulation against the same data plotted in Matlab. The Matlab plot presents much more detail than TecPlot.
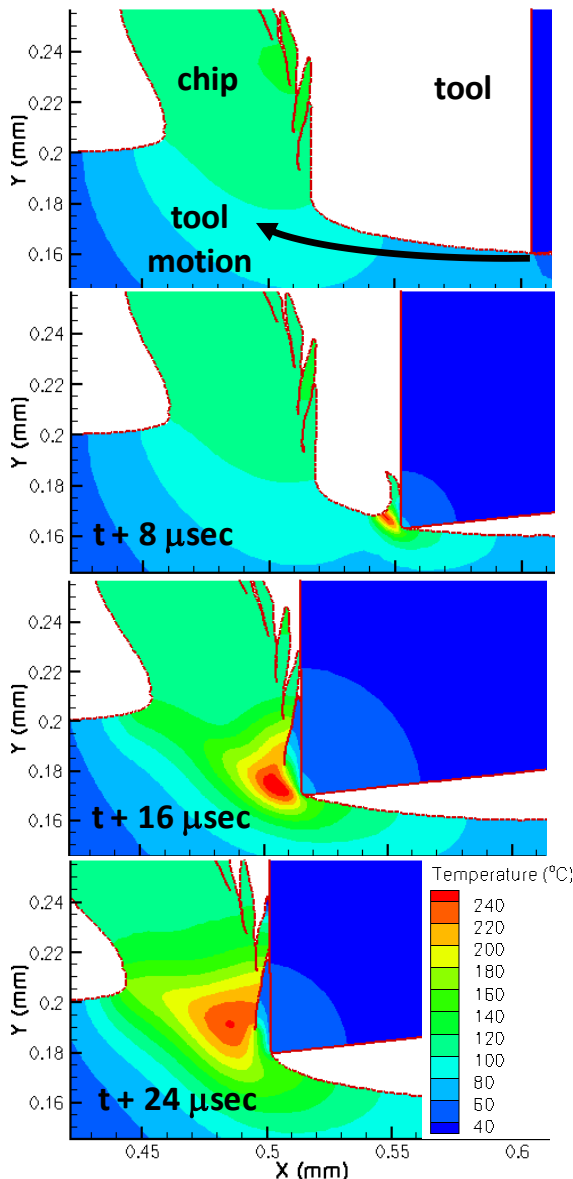

Figure 3. Example of temperature contour results from AdvantEdge EVAM simulation (110x20 μm ellipse, 10 kHz vibration, 20μm DoC, 0.2 m/s workpiece speed, diamond tool on St1118 workpiece)

Figure 4. Top: TecPlot plot of EVAM simulation data with high-order polynomial interpolation. Bottom: Matlab plot of same data with 1000 point subsampling and 10 pt running average.
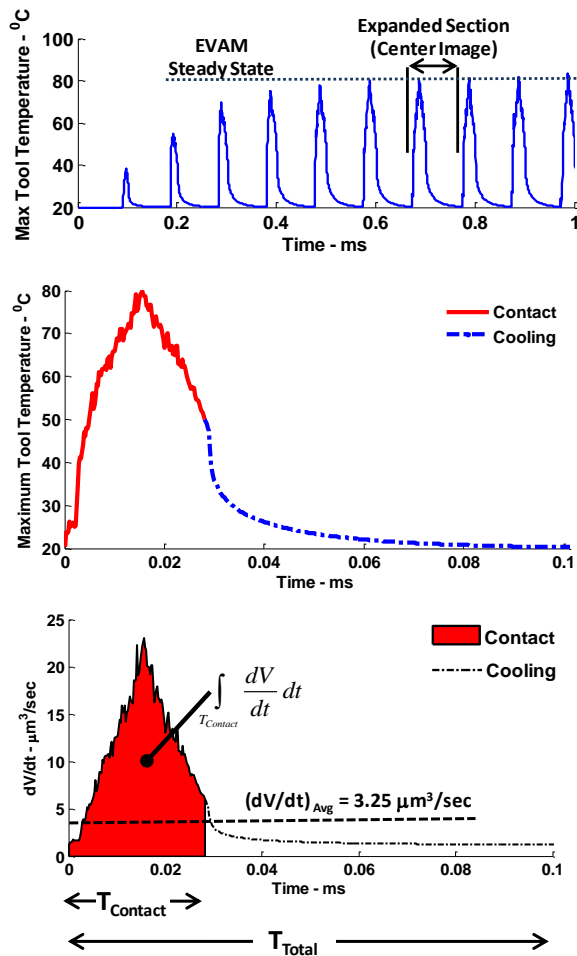
Figure 5. <u>Top</u>: Example temperature results for EVAM simulation (same machining parameters as Figure 3 and Figure 4).
<u>Middle</u>: Expanded temperature profile of one EVAM cycle.
<u>Bottom</u>: Instantaneous wear rate profile determined from center image and Arrhenius wear model.

AdvantEdge data from all EVAM simulations were sub-sampled every 1000 points and stored in a Matlab array. Force data presented noise that was about 10% the peak force value, so was smoothed by a 10 pt running average. Temperature data had noise less than 1% peak values and was not smoothed. Temperature data from EVAM simulations are supplied to the Arrhenius wear model (Equation (1)) using the middle estimated Arrhenius constants from Table 1 (E_a = 42.5 kJ/mol, A = 4.5 x 10^7 μm^3/s).

The process for calculating EVAM wear rates is shown in Figure 5. Since the tool wears only while in contact with the workpiece, the average wear rate is determined by integrating the instantaneous wear rate only over the contact time, but dividing this value by the total cycle period:

$$\left(\frac{dV}{dt}\right)_{Avg.} = \frac{1}{T_{Total}}\left(\int_{T_{Contact}} \frac{dV}{dt}\, dt\right) \qquad (2)$$

Contact time depends on EVAM tool frequency, workpiece velocity, ellipse shape, and depth of cut. If the depth of cut (measured from the workpiece surface to bottom of

58

ellipse) is larger than the vertical axis of the ellipse, the contact time is approximately 25% of the ellipse vibration period. Average wear rates were compared for different temperature spikes of the same EVAM simulation. These calculated wear rates varied less than 3% from spike to spike during steady state, therefore only one steady state temperature spike is used to calculate average EVAM wear rates.

6.3.2 SIMULATIONS VARYING HORIZONTAL SPEED RATIO

In the conventional machining simulations, temperature was shown to increase linearly with workpiece velocity, and logarithmically with depth of cut [6]. In EVAM, the velocity of the vibrating tool exceeds the workpiece velocity, which cause higher peak tool temperatures. Higher workpiece velocities also create larger chips if the EVAM frequency is kept constant, which in turn create higher temperature. The horizontal speed ratio (HSR) relates the peak EVAM ellipse speed to the workpiece velocity. It is typically related to PV surface finish [7], but it also determines the relative EVAM chip size, as shown in Figure 6.

$$HSR = \frac{v_{wkpc}}{a\omega} \tag{3}$$
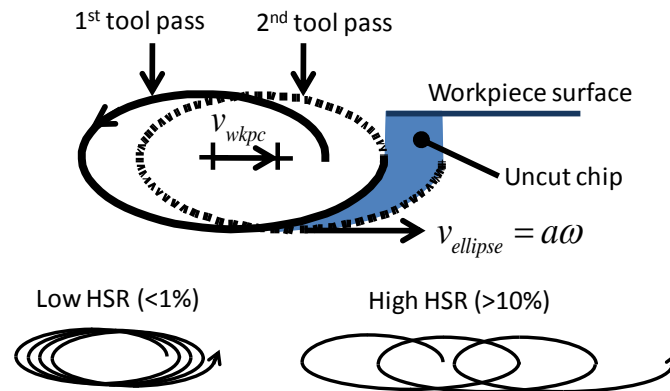
Figure 6. Relation of horizontal speed ratio to EVAM chip size

It is estimated that the dual contribution of speed and chip size to tool temperature creates a nonlinear increase to EVAM tool temperature vs. workpiece velocity (or HSR) for a constant frequency. It's further estimated that this creates a specific HSR in which the average wear rate of the EVAM tool will be greater than if conventional machining were done. To test these hypotheses, EVAM simulations were created in AdvantEdge that varied only workpiece velocity and thereby HSR. Simulation parameters are given in Table 2. Equivalent conventional cutting simulations were also created with the same workpiece velocity and depth of cut for a total of 8 simulations.

Table 2. Simulation parameters for 4 EVAM and 4 conventional cutting simulations

EVAM Frequency	10 kHz
Ellipse Shape	110 x 20 μm
Depth of Cut	40 μm
Workpiece Velocity	0.1, 0.2, 0.6, 1 m/s
Tool Material	Single Crystal Diamond
Workpiece Material	AISI 1118 Steel

FEM Results of Varying Horizontal Speed Ratio

Temperature profiles from the EVAM simulations are shown in Figure 7. Temperature profiles are shifted such that the same time points of the ellipse trajectories are aligned on the X axis. Temperature increases sooner for higher HSRs since the tool enters the workpiece at an earlier point on the ellipse which increases the overall contact time.
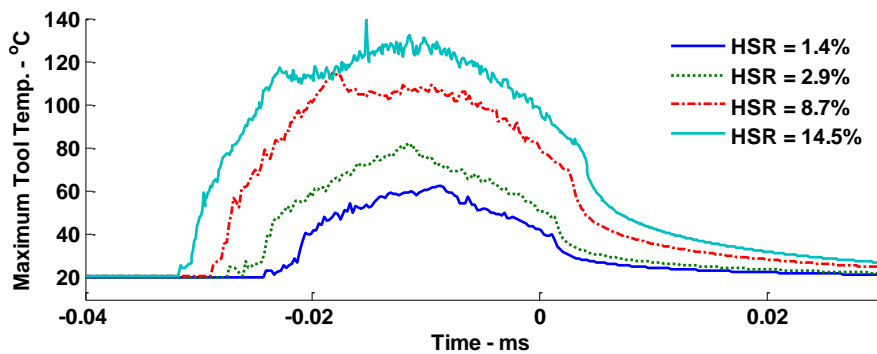
Figure 7. Maximum simulated EVAM tool temperatures for varying horizontal speed ratios.

Peak EVAM tool temperatures were much higher than their conventional machining equivalent due to the increased tool tip velocity. Average EVAM tool temperature was determined by integrating temperature profiles in Figure 7 over one EVAM period (0.1 ms). These average temperatures are compared against steady state non-EVAM tool temperatures, shown in Figure 8. Average EVAM temperatures were higher than conventional temperatures for all but the highest workpiece velocity or HSR.
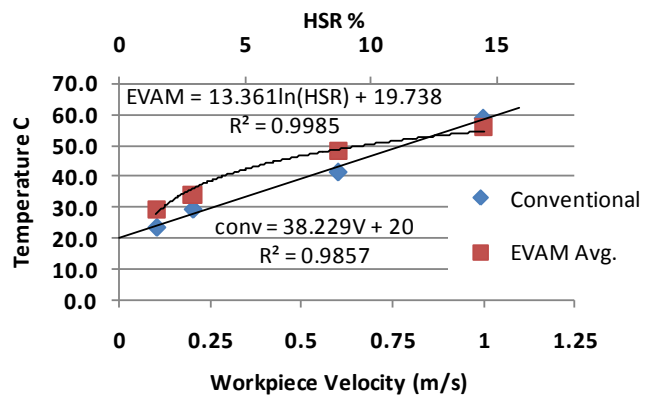
Figure 8. Steady state temperatures from conventional machining simulations and average EVAM too temperatures.

60

Temperature profiles from Figure 7 and steady state temperatures from conventional machining simulations were used with the Arrhenius wear model to calculate average volumetric wear rates, dV/dt. Dividing this value by workpiece velocity gives worn volume per machining distance, shown in Figure 9. The hypothesized crossover point where EVAM wear rate exceeds conventional wear rate occurred at an HSR of 2.0 %.
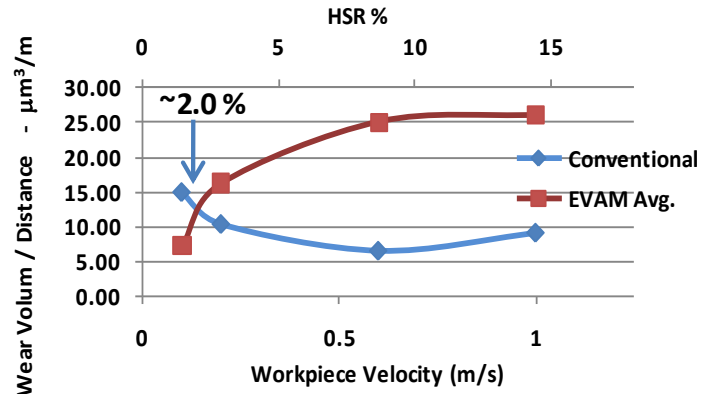
Figure 9 Calculated wear rates for conventional machining and EVAM.**3**

Special note should be taken, however, that the workpiece velocities simulated for conventional cutting are relatively low (<1 m/s) with low resulting temperatures. EVAM workpiece velocity is limited by the vibration frequency to produce a certain surface finish, while conventional machining speeds may be increased substantially before surface finish is affected. If the 1.4% HSR EVAM simulation is compared against the 1 m/s conventional simulation in Figure 9, one sees that wear/distance is less for EVAM.

6.3.3 SIMULATIONS VARYING FREQUENCY

The increase in tool tip velocity with EVAM frequency yields higher temperatures, but another contributor is the residual temperature in the tool as it comes back into contact with the workpiece with each ellipse cycle. The cooling rate of a tool no longer in contact with the workpiece depends on thermal material properties, geometry, and convective or conductive boundary conditions. For each simulation varying EVAM frequency, the tool model is the same in each of these traits; therefore cooling rates (time constants) are the same for each simulation. Simulation parameters are given in Table 4. To ensure that variations in chip size do not affect temperature, the same HSR of 2.9% is used for each simulation by varying the workpiece velocity with the frequency.

Table 4. Simulation parameters for 4 EVAM simulations varying frequency

EVAM Frequencies	10, 20, 30, 40 kHz
Ellipse Shape	110 x 20 μm
Depth of Cut	40 μm
Workpiece Velocity	0.2, 0.4, 0.6, 0.8 m/s
Tool Material	Single Crystal Diamond
Workpiece Material	AISI 1118 Steel

61

The wear of the tool may be exacerbated by the increased residual tool temperature and increased heat flux due to faster tip velocities. Higher frequencies, however, allow faster machine time. Understanding the relationship between wear and frequency will allow for an optimal operation point given the benefits of faster machine time vs. the detriment of higher wear rates.

FEM Results of Varying Frequency

Figure 10 shows the temperature results for the 4 EVAM simulations varying frequency. As expected, higher frequencies resulted in higher peak temperatures. Average temperature was determined by integrating the temperature curves after reaching steady state and dividing by time. Residual temperature was determined by measuring temperature just before the tool makes contact with the workpiece.
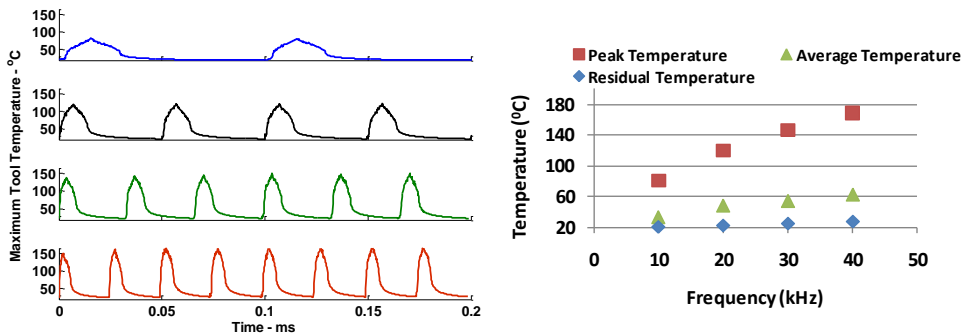
Figure 10. Left: Simulated maximum tool temperature profiles for different EVAM frequencies. Right: Results of different components of the temperature profiles.

Temperature profiles were again supplied to the Arrhenius wear model as done with the HSR simulations, and average wear rate was determined using equation(2). These average wear rate results are shown in Figure 11, left. These values were divided by workpiece velocity to get wear volume per machining distance, shown in Figure 11, right. The wear per time increased with the frequency squared while the wear per distance increased linearly with frequency.
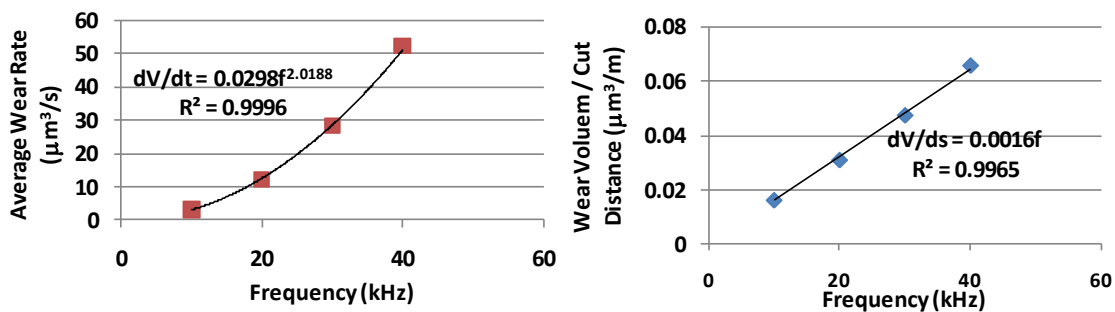
Figure 11. Left: Average wear rate (volume loss per time) for varying frequencies. Right: Wear per machining distance.

6.3.4 SIMULATIONS VARYING ELLIPSE SHAPE

The history of EVAM research includes individual analyses of horizontal, circular, or vertically oriented elliptical toolpaths. Researchers preferring the horizontal ellipse shape (including the PEC) extol the ability to machine at higher speeds while maintaining an adequate surface finish. Proponents of the vertically oriented elliptical cutting claim the upward motion of the tool assists in lifting the chip out from the workpiece, thereby creating a net zero or negative thrust force on the tool and reducing wear [1]. A direct comparison is complicated by the relationships between ellipse shape, workpiece velocity, frequency, surface finish, and uncut chip shape.

In order to observe the effects of varying ellipse shape, some EVAM parameters need to remain constant. Ultimately, the desired result of using EVAM is to maintain an adequate surface finish over the longest machining distance, therefore a constant theoretical surface finish is maintained in the EVAM-FEM models. Theoretical surface using EVAM depends on the machining speed, frequency, and ellipse curvature in the same manner that surface finish in conventional turning depends on cross-feed and tool radius. An approximated calculation of PV surface finish is given:

$$PV \approx \frac{feed}{8R} \approx \frac{b}{8}\left(\frac{v_{wkpc}}{fa}\right)^2 \quad for \quad HSR = \frac{v_{wkpc}}{a\omega} << 1 \quad\quad (4)$$

This equation shows that for an ellipse shape determined by axis amplitudes a and b, the workpiece velocity v_{wkpc} and tool vibration frequency f must change proportionally with one another to maintain a constant PV surface finish. Three other parameters are maintained constant to fully define EVAM simulation: depth of cut, vibration frequency and ellipse included area. Depth of cut is set larger than the largest vertical amplitude so that tool motion in each simulation completely undercuts the workpiece surface.

Table 5. Machining parameters for 3 EVAM-FEM models varying ellipse shape.

EVAM Frequency	20 kHz
Ellipse Shapes, axb	56.6x11.3 µm, 25.3x25.3 µm, 11.3x56.6 µm
Ellipse Aspect Ratio, r = a/b	5.01, 1.00, 0.20
Depth of Cut	60 µm
Workpiece Velocity	0.237, 0.07, 0.02 m/s
Theoretical PV	58 nm
Tool Material	Single Crystal Diamond
Workpiece Material	AISI 1118 Steel

Using these input values, the relative effects of varying ellipse shape are calculated for multiple other machining parameters. These resulting parameters are normalized against the maximum

value in the range to observe the relative effect from ellipse ratio has. Results are shown in Figure 12. It is noteworthy that the sliding distance per upfeed decreases as the ellipse ratio increases. When this ratio is multiplied by the total cutting distance, it gives the total distance over which the tool was in contact with the workpiece. Therefore, horizontally inclined ellipses allow the tool to contact the workpiece less than vertical ellipses for the same total cutting distance.
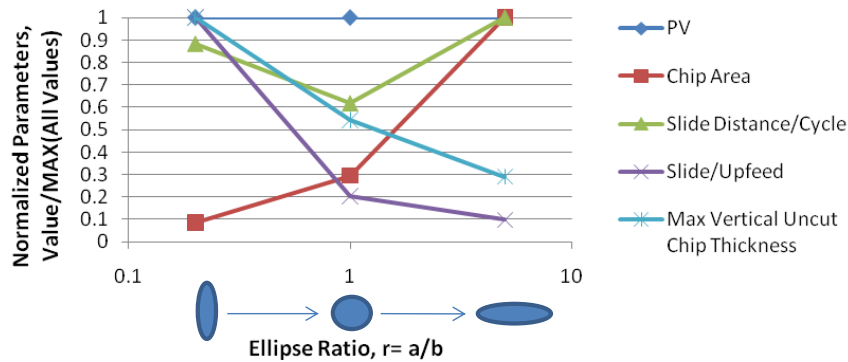
Figure 12. Normalized machining parameters calculated from EVAM input parameters

Based on these calculations, it was estimated that the horizontal ellipse models would result in greater chemical wear per EVAM cycle. Increased chip area, workpiece velocity, and sliding distance per cycle contribute to higher tool temperatures and forces for each EVAM cycle. However, the resulting higher rates of wear per cycle may not necessarily mean greater amounts of wear over the same total machining distance. The higher temperatures ensured by the horizontal ellipse are balanced by the increased machining speed, which allows the tool to be in contact with the workpiece for less total time. Therefore, the effect ellipse shape will have on wear cannot be estimated solely based on kinematic calculations, but require the thermo-mechanical response available through FEM.

FEM Results of Varying Ellipse Shape

Tool forces and temperatures were extracted from the three AdvantEdge simulations using the method described in section 6.3.1. Figure 13 shows the cut and thrust force for the each simulation. Overall forces tended to increase as the ellipse became horizontal; a result of the increasing uncut chip area described in Figure 12.
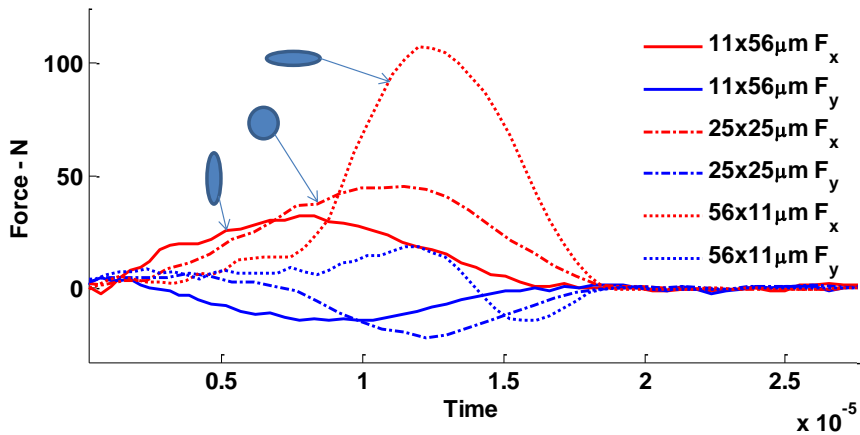
Figure 13. Cut (F_x) and thrust (F_y) forces for varying ellipse shapes over one 20kHz cycle.

The amount of time that the tool experiences negative thrust force was smallest for the horizontal ellipse shape, although all three ellipse shapes exhibited some negative thrust. Thrust forces for the vertical ellipse were negative for almost the entire vibration cycle, indicating a continuous state of 'lifting' the chip from the workpiece. Though this reduces the overall tool force, tool temperature likely has a greater effect on wear, as described in section 6.1. Figure 14 shows results of maximum tool temperature for one EVAM cycle and the estimated wear rate based on these temperatures and the Arrhenius wear model. The horizontal ellipse shape resulted in highest peak temperatures due to the higher tool tip velocity and chip size. Average wear rates were also calculated using Equation(2). Table 6 summarizes these values.
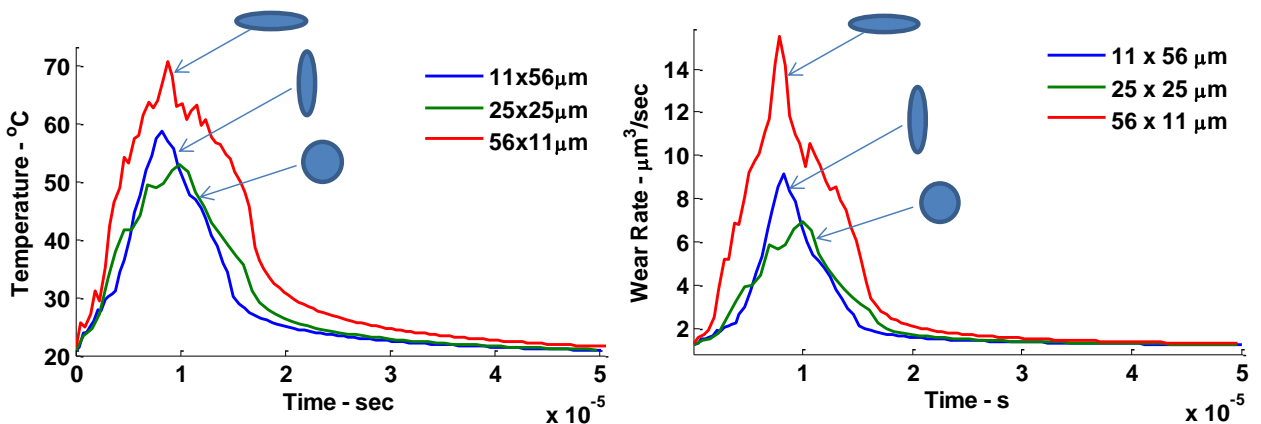
Figure 14. FEM results of maximum tool temperature (left) and calculated wear rate based on Arrhenius model (right) for varying EVAM ellipse shapes.

Table 6. Calculated temperature and estimated Arrhenius wear from EVAM FEM models with varying ellipse shape.

Ellipse Shape, Ratio	Peak Tool Temperature - °C	Average Tool Temperature - °C	Average Wear Rate – $\mu m^3/sec$	Wear Volume / Machining Distance – $\mu m^3/m$
11x56 μm r = 0.2	59.5	28.3	1.30	63.7
25x25 μm, r = 1	52.6	29	1.35	19.29
56x11 μm, r = 5	70.8	34	2.46	10.38

The average wear rate measured in volume of diamond loss per time was greatest for the horizontal ellipse (56x11 μm, r = 5) simulation. As previously mentioned, this indicates a more aggressive cut during each EVAM cycle based on the higher forces and temperature. However, due to the increased machining speed, the total wear volume per machining distance is least for the horizontal ellipse. This shows that the benefit of increased machining speed outweighs the effects of a more aggressive EVAM cutting cycle when surface finish is constant.

## 6.4 EVAM EXPERIMENTS VARYING FREQUENCY

Two of the three EVAM parameters modeled in FEA (frequency and ellipse shape) will also be varied through cutting experiments. The EVAM cutting device at the PEC, called the Ultramill, is capable of operating between 1-4 kHz. Though HSR could be varied experimentally, this would require conventional machining speeds on the order of 2-8 mm/s for a similar comparison to Figure 9. The following gives results of EVAM experiments varying frequency. Further experiments varying ellipse shape are planned for the future.

6.4.1 EXPERIMENT SETUP

The first design of the Ultramill included a ceramic toolholder with two base grooves. These grooves pivoted on ceramic half-cylinders that were attached to piezoelectric stack actuators. Machining with the Ultramill caused compressive stress on the rear groove, forcing the groove to open and form a crack along its length. Also, the half-cylinder / groove contacts were kinematically over constrained, causing potential for contact loss. A new toolholder shown in Figure 15 was designed for the Ultramill that incorporates a thicker base with one groove and flat. Also shown is the relationship between the elliptical toolpath and the kinematic linkage to the piezoelectric stack actuators.
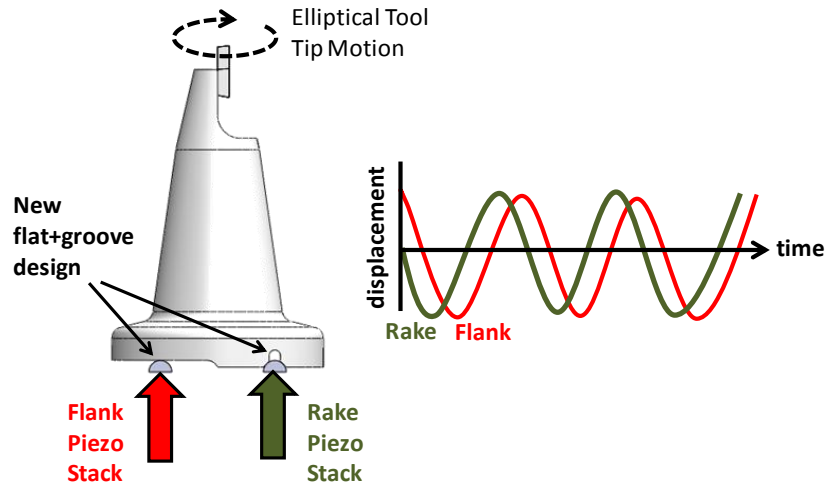
Figure 15. New flat+groove Ultramill toolholder design and kinematic linkage for elliptical toolpaths

Orthogonal cutting geometry was used for the EVAM experiments where the direction of cutting is parallel to the rake face normal. A 0.25mm wide by 41 mm long fin was machined into a piece of AISI1215 steel and a central hole allowed the workpiece to be mounted on a 3-axis piezoelectric load cell. A straight-edged, 0° rake, 6° clearance synthetic diamond tool was mounted to the ceramic Ultramill toolholder. The 2.28 mm width of the tool allowed the workpiece to contact in 4 distinct wear zones, shown in the front view of Figure 16. One zone was utilized to initially machine the surface of the fin so that consequent machining is done on a flat surface and there is no variation in the depth of cut. Three other zones were defined for EVAM machining at 1, 2, and 4 kHz.
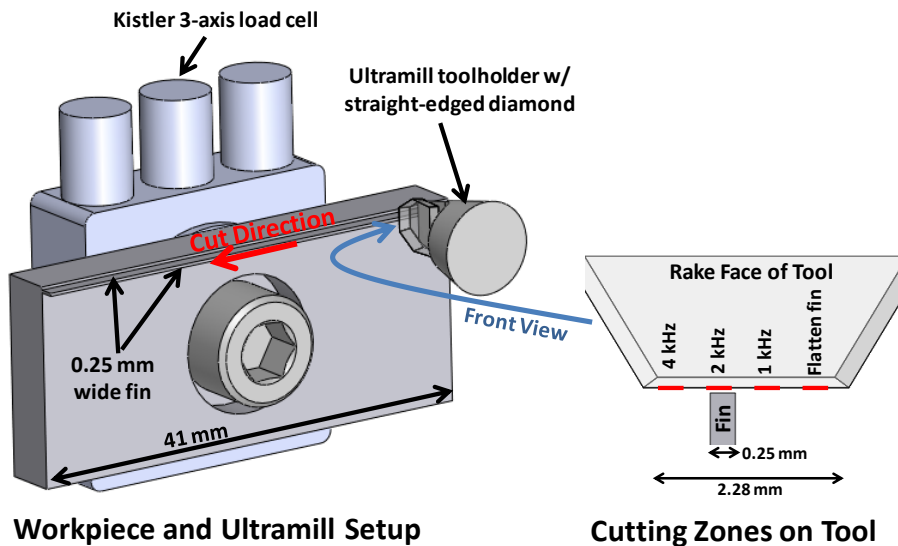
Figure 16. Schematic of AISI 1215 steel fin workpiece, cutting orientation, and wear zones on the tool for EVAM wear experiments varying frequency.

A Lion Precision air bearing LVDT was used to measure the alignment of the workpiece about the center screw and the pitch in the cutting direction. The fin was aligned about the center screw to within 5 μm over the 41 mm fin length. This ensures that the width of the wear zones is nominally the same width as the fin. The pitch of the fin in the cutting direction was measured and compensated for in the CNC program.

The fin was initially cut using the 'flatten fit' section of the tool noted in Figure 16. A constant drip (~1 drop/sec) of Mobilmet Omicron cutting fluid was used so that the cutting region was continuously covered. Touchoff was accomplished by advancing the tool toward the workpiece in 100 nm increments and measuring changes to the force signal from the load cell. After initial touchoff, a CNC program was run that cut the 41 mm length of the fin incrementing down with 2 μm depth of cut. A total of 120 passes were completed for a total machining distance of 5.13 m. Tool forces measured from the load cell were acquired every 20 passes. After the CNC program ended the workpiece was then removed from the machine and surface finish was measured. The cutting and workpiece measuring process was repeated on the same fin for 2 kHz and 4 kHz using the corresponding locations on the tool edge (Figure 16). Similarly to FEM simulations, workpiece velocity was increased to match the EVAM frequency and preserve a constant uncut chip shape. Table 7 gives corresponding velocities and constant parameters defined by the uncut chip shape.

Table 7. EVAM machining parameters for cutting experiments varying frequency

EVAM Frequency	Workpiece Velocity	Total Machining Time (including non-cutting passes)	Total Contact Time
1 kHz	2 mm/s	1 hr 40 min	10 min 47sec
2 kHz	4 mm/s	55 min	5 min 23 sec
4 kHz	8 mm/s	32 min	2 min 42 sec

Constant Parameters:

Ellipse Shape = 11 x 2 μm (horizontal)	Horizontal Speed Ratio = 2.89 %
Upfeed per cycle = 2 μm	Depth of Cut = 2 μm
Theoretical PV Surface Finish = 8 nm	Sliding Distance / Cycle = 13.0 μm
Sliding Distance / Upfeed Ratio = 6.49	Duty Cycle (% contact) = 25.9 %

Two particular parameters of interest are the sliding distance / upfeed ratio and the duty cycle. The sliding distance / upfeed ratio tells how far the tool slides against the workpiece per distance the workpiece travels. Multiplying this ratio by the machining distance (5.13 m) gives you the real distance over which the tool contacts the workpiece (33.30 m). The duty cycle tells what percentage of the EVAM cycle the tool is actually in contact with the workpiece. Multiplying this by the machining distance over workpiece velocity gives the total time the tool is contacting the workpiece.

6.4.1 SURFACE FINISH

After each 5m cut distance, the workpiece fin was observed in a Zygo NewView scanning white light interferometer (SWLI). Figure 17 compares a surface finish measurement from the conventional machining experiments mentioned in Section 6.2 with one obtained from the EVAM experiments. The steel surface after conventional machining was dominated by grooves in the cutting direction likely caused by dragging of hard alloying inclusions through the metal. The EVAM surfaces did not display this dragging, but exhibited inclusions 'stuck' into the surface. The absence of dragging was seen in all of the measured EVAM surfaces, each of which had consistent surface finish of < 15nm Ra.

AISI 1215 Steel, Conventional Machining
40 m machining distance
Ra = 122 nm

AISI 1215 Steel, 1 kHz EVAM
5 m machining distance
Ra = 7 nm
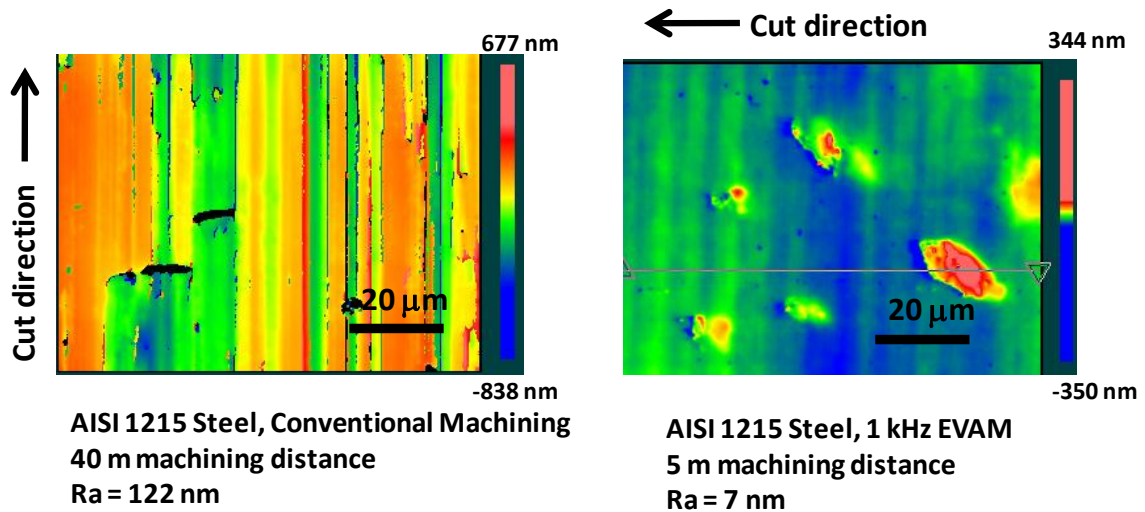
Figure 17. Conventional machining surface finish vs 1kHz EVAM surface finish on AISI 1215 steel.

Figure 18 shows a cross-section slice from the horizontal line of the surface in Figure 17 right. This slice covers one of the alloy inclusions, which has a height of approximately 60 nm. Though visible in the SWLI surface plot, these inclusions contributed little to the overall surface finish due to their relatively small heights.
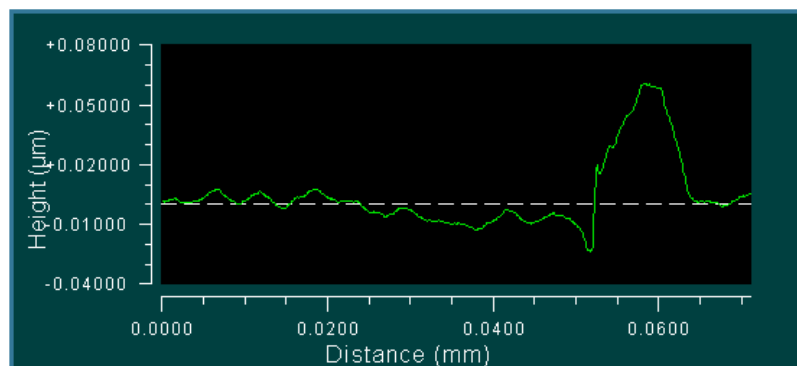
Figure 18. 2D surface slice from horizontal line in Figure 17, right shows height of inclusion.

69

The surface finish of the AISI 1215 steel after EVAM was much improved compared to the conventional machining of the same material (~10 nm Ra compared to >100 nm Ra). The improved surface finish with EVAM is a result of the tool not dragging the alloying inclusions through the surface. Measuring the tool wear will elucidate whether this non-dragging is a result of the unique tool motion, a reduced level of wear, or both.

6.4.2 EVAM TOOL WEAR

Prior to measurement in the SEM, the tool surface was observed in the SWLI with 100x zoom. No metal pickup was observed on the tool edge, whereas the tools observed during the conventional steel machining had noticeable pickup extending several microns from the cutting edge. The effects of pickup on tool wear are unknown. The 1, 2, and 4 kHz wear zones (Figure 16) were measured using the EBID method [3]. Each EBID image was

Table 8. Calculated 2D wear area for 3 EVAM frequencies (5 m distance)

EVAM Frequency	2D Worn Cross-Section Area
1 kHz	$0.873 \pm 0.098 \ \mu m^2$
2 kHz	$0.959 \pm 0.071 \ \mu m^2$
4 kHz	$0.834 \pm 0.067 \ \mu m^2$

measured 10 times with 2σ confidence intervals given in Table 8. The 2D worn cross-section area can be multiplied by the workpiece width (0.25 mm) to approximate total worn volume. Wear varied little with each EVAM frequency. Traces were made from EBID images that match the 2D worn cross-section of the diamond tool are shown in Figure 19. Two tool cross-sections from conventional machining experiments are also shown for reference. After only 5 m machining distance the EVAM tool wear is comparable to conventional machining after 216 m the same workpiece material.

Figure 19. 2D worn tool cross sections for EVAM and conventional machining.

Though machining distance was different for the EVAM experiments and 216 m conventional experiment, the total contact time is comparable. The real contact distance of the EVAM tool was 33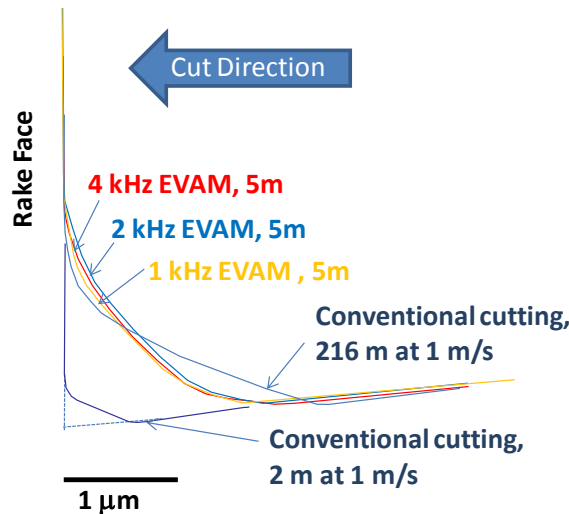.3 m with contact times between 2.7-10.8 min. The 216 m conventional tool had a contact time of 3.6 min, while the 2 m conventional tool only contacted for 2 sec.

6.5 CONCLUSIONS

A chemical wear model was developed based on the Arrhenius equation. Wear measurements made during conventional DT of St1215 were coupled with tool temperatures obtained from FE simulations to construct an Arrhenius plot. The proposed activation energy is in the range of 22-83 kJ/mol. This is relatively low compared to metal-on-metal diffusive processes. The constant removal of diamond in addition to a catalytic relationship between diamond and ferrous workpiece are likely reasons for this low activation energy.

FE simulations of EVAM cutting completed varying horizontal speed ratio, tool vibration frequency, and ellipse shape. Simulated tool temperatures were coupled with the Arrhenius wear model to determine average EVAM wear rates. It was found that at a certain value of HSR, the wear of an EVAM tool with respect to machining distance exceeds that of conventional machining when assuming the Arrhenius model. From simulations varying frequency it was found that increasing the EVAM frequency while maintaining the same HSR causes a linear increase of tool wear per machining distance with increased frequency. Simulations varying ellipse shape showed that horizontally ellipses (aligned with the cutting direction) generate higher forces, temperature, and wear pear each vibration cycle. However, horizontal ellipses allow higher machining speeds to maintain the same theoretical surface finish. This higher machine speed results in less wear per machining distance for the horizontally aligned EVAM ellipse.

EVAM experiments were conduction that varied vibration frequency while maintaining the same HSR. After 5m machining distance, EVAM frequencies at 1, 2, and 4 kHz yielded the same amount of wear. The experiment needs to continue at further machining distances to relate to results found from FE models. The EVAM tool wear at 5 m was comparable to conventional machining at 216 m, and far greater than conventional machining after 2 m. This shows that EVAM did not reduce tool wear over the same machining distance, but does result in a similar amount of wear related to contact time. Despite excessive tool wear, EVAM yielded a dramatically better surface finish. This is primarily due to the absence of particle dragging through the workpiece surface, which dominates the surface structure of conventionally machined steel. Another contribution to surface finish improvement may come from metal pickup on the tool which was observed after conventional machining but not EVAM.

REFERENCES

1. Brehl DE, Dow TA. *Review of Vibration-Assisted Machining*, Precision Engineering. 2008; 32: 153-172.
2. Paul E, Evans CJ, Mangamelli A, McGlauflin ML, Polvani RS, *Chemical Aspects of Tool Wear in Single Point Diamond Turning*, Precision Engineering. 18; 4-19
3. Shi M, Lane B, Mooney CB, Dow TA, Scattergood R, *Diamond Tool Wear Measurement by Electron-beam-induced Deposition*, Precision Engineering. 2010; Article in press.
4. Lane B, *Development of Predictive models for Abrasive and Chemical Wear of Diamond Tools*, MS Thesis, North Carolina State Univesity, 2010
5. Negishi N, *Elliptical Vibration Assisted Machining with Single Crystal Diamond Tools*, MS Thesis, North Carolina State University, 2003.
6. Lane B, Dow TA, Scattergood R, *Diamond Tool Wear Improvements with Elliptical Vibration Assisted Machining*, Precision Engineering Center Annual Report, 2010
7. Cerniway M, *Elliptical Diamond Milling: Kinematics, Force, and Tool Wear*, MS Thesis, North Carolina State University, 2001

7 VISUALIZATION OF CHIP SHAPE AND MACHINING FORCES

Darrell LaBarbera
Graduate Student
Thomas A. Dow
Professor, Mechanical and Aerospace Engineering

The goal is this project was to develop a method to measure the cutting forces at the same time the chip shape was measured. These two tasks have been done separately by a number of investigators, but performing them simultaneously will provide increased understanding of the chip pickup problem. Under certain cutting conditions, the workpiece material becomes attached to the cutting tool resulting in much higher tool forces and poor surface finish. The onset of this phenomenon may be due to lubrication breakdown and/or chemical affinity of the tool and workpiece. The particular emphasis is diamond turning where a single-crystal diamond tool is used to machine different types of steel. Under some conditions it is virtually impossible to machine the surface because of huge changes in the force (factor of 10). Tool cutting and thrust forces and chip shape have been recorded for depths of cut from 7 to 25 μm on aluminum and steel workpieces. Images of the chips at each depth of cut were collected with sufficient visual clarity to see the chip formation. Higher magnification and faster shutter speed will be required to see shear bands or the actual pickup of material on the tool. Machining experiments using 1010 steel were performed at 7 and 10 μm depths of cut with carbide and diamond tools. The diamond tool produced a smooth clean chip while the carbide tool produced a discontinuous chip. The discontinuity of the chip was used to explain the variable forces observed with the carbide tool.

73
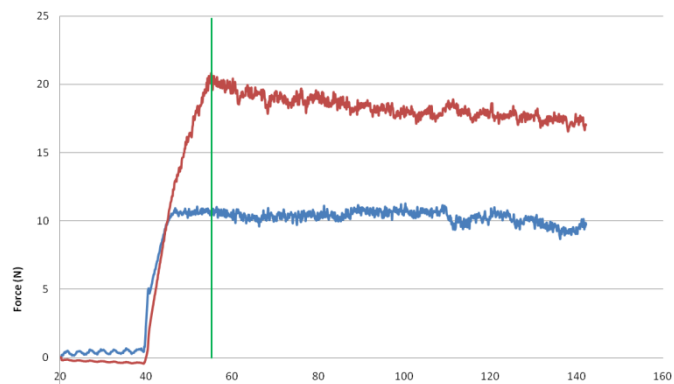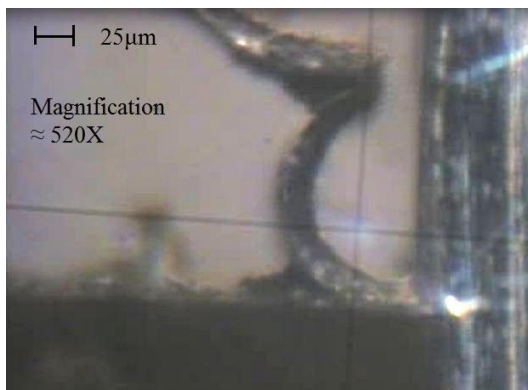
7.1 INTRODUCTION

Precision machining, using a diamond tool or a diamond grinding wheel, can be used to create surfaces with optical quality figure error (< 150 nm) and surface finish less than 5 nm RMS. The detailed shape of the diamond tool or grinding wheel grit has a profound influence on both of these figures of merit. There has been a wealth of information generated by researchers related to the tool shape, the workpiece material, lubrication and the forces in the cutting and thrust direction. For diamond machinable materials (hard copper, brass, aluminum and some ceramic materials), the cutting process is very stable and the chips and forces are constant for long periods of time, sometimes for many days. However, there are other materials that are not typically machined with diamond tools, such as steel, and the cutting process is anything but stable. Knowledge of the material flow and the parameters that influence it are important to improve the shape and surface finish of new materials.

The cutting forces generated during diamond turning are a function of the shape and rake angle of the tool, the depth of cut, the friction on the rake and flank faces and the machining speed. Simulations of the cutting process [1] use a complex material model to predict the flow of material over/under the tool based on yield stress, shear rate, temperature and many other material properties. The result is a picture of the flow, the predicted cutting force (in the cutting direction), thrust force (normal to the cutting direction) as well as temperature in both the tool and the chip.

The goals of this project are to bring together measurements of tool forces, images of chip flow and predictions of temperature and material response in precision machining. This will require measurement of the machining forces, high speed photography as well as thermal modeling and measurement.

7.2 MACHINING EXPERIMENTS

One important issue that the cutting models do not address is the potential of material pickup on the cutting edge of the tool. This phenomenon changes the flow field, the forces and the surface finish of the workpiece. Visualization of the chip has improved the understanding of the pickup process and how it changes with machining conditions and tool geometry [2-4]. The goal of this project is to use equipment available in the PEC to demonstrate the tool forces and chip shape that results in machining steel and aluminium workpieces. This report describes the experimental apparatus, the experiments performed and the results.

7.2.1 EXPERIMENTAL SETUP
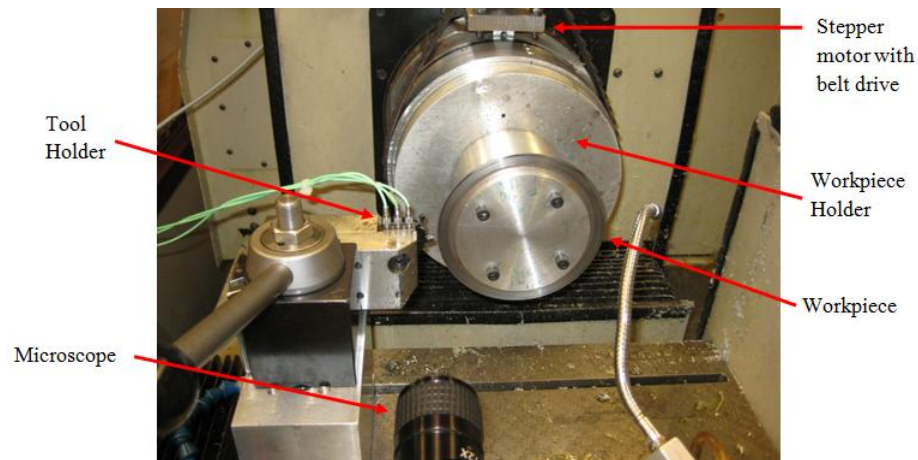
Figure 1: Slow Speed Turning Setup

Figure 1 shows the DTM with the force sensor and visualization system as well as the stepper motor and belt needed for the slow speed required. The stepper motor is attached to the machine frame and the belt drives the OD of the vacuum chuck. This system was capable of turning the lathe vacuum chuck down to 0.05 rpm or approximately 0.33 mm/s at the tool. The tool was fed from left to right and the microscope was mounted on the same slide so it stays focused on the tool.

For the cutting experiments, a flat nose diamond tool was used and the workpiece was narrower than the tool producing orthogonal cutting. For the aluminum tests, the workpiece was a thin circular sheet with a diameter of 129.3 mm and a thickness of 0.77 mm. This sheet was clamped between two cylinders for support and less than 10 mm extended from the clamping cylinders. The cutting experiments using 6061-T6 aluminium are all performed at 0.02 revolutions per second of the stepper motor or 0.16 rpm for the lathe spindle. The linear velocity of the workpiece was 1.08 mm/sec.

The face of the thin workpiece was machined so that it was cylindrical and centered. Then the stepper motor was set to rotate at 0.02 revolutions per second. The tool was then plunged into the workpiece at 0.1 mm/min while the workpiece rotated. Two depths of cut were studied, 10 and 25 μm. With the infeed speed used, the two depths of cut were reached in 6 and 15 seconds, respectively, as shown on the force plots. The cutting time was set not to exceed one revolution of the workpiece or 6 minutes and 15 seconds. Each time the experiment was restarted the workpiece was refaced. The aluminum experiments were designed to show what can be visualized with the microscope and camera available at the PEC.

Proprietary Release subject to the terms and conditions of the Precision Engineering Center Membership Agreement and North Carolina State University Office of Technology Transfer nondisclosure agreements.

The cutting experiments for 1010 steel were all performed at 0.08 rpm for the lathe spindle. The thickness of the steel disk was 0.49 mm and the diameter was 128.2 mm. The linear velocity of the workpiece was 0.54 mm/sec. These experiments began, as with the aluminum material, by facing the cutting surface so that it was circular. Each time the experiment was restarted the workpiece was refaced. Two tools materials were used for the steel machining experiments, carbide and single-crystal diamond.

7.2.2 EXPERIMENTAL RESULTS

ALUMINUM 6061-T6 - 10 μm DEPTH OF CUT
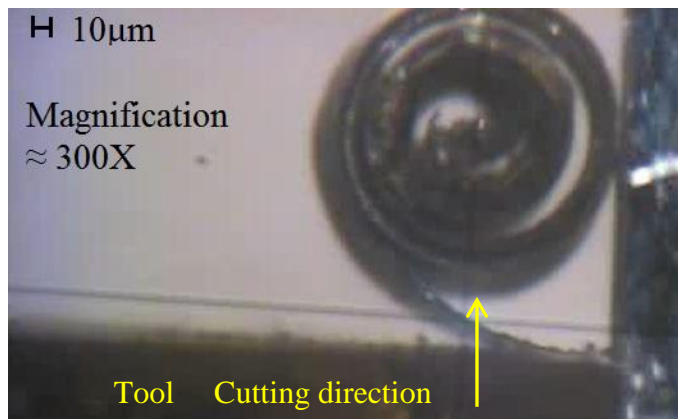
Figure 2: Chip image for 10μm depth of cut

Figure 2 shows the chip generated at a 10μm depth of cut and Figure 3 shows the associated forces. The average cutting force was 8.1 N and the thrust force was 4.7 N. The picture in Figure 2 corresponds to the vertical line on Figure 3 with respect to the time. For constant infeed, the depth of cut increases as time increases until it reaches the desired depth. Figure 3 shows the cutting force (F_z top) and the thrust force (F_x bottom) as a function of the machining time. Both forces increase in a similar manner as the tool moves into contact with the workpiece. As tool moves into the workpiece and a chip is formed, the thrust force reaches an asymptote related to the geometry of the tool and the properties of the workpiece. The thrust force does not change but as the depth of cut continues to increase; the cutting force grows larger until the desired depth of cut is reached. For the 10 μm depth of cut and an infeed rate of 0.1 mm/min, it should take 6 seconds to reach the nominal depth. The dotted line on Figure 3 shows about 6 seconds from the start of cutting to achieve steady-state operation.
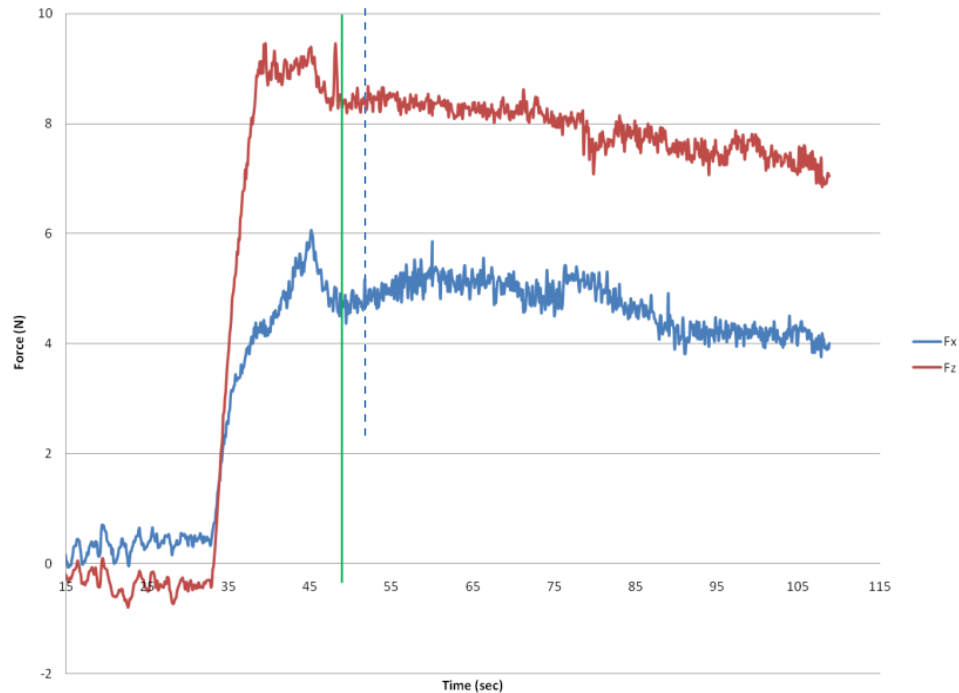
Figure 3: Tool forces machining 6061-T6 aluminum at 10 μm depth of cut

ALUMINUM 6061-T6 - 25μm DEPTH OF CUT
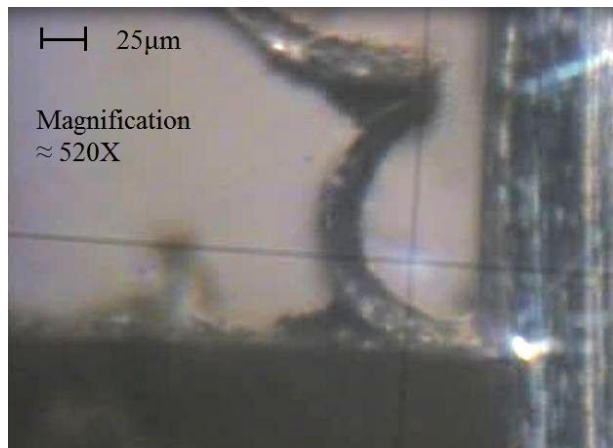
Figure 4: Diamond Tool 25μm Depth of Cut Picture

Figure 4 shows an aluminum workpiece at a 25 μm depth of cut. Figure 5 shows the forces collected during this experiment. This force curve clearly shows the increase in force as the tool plunges into the workpiece at 0.1 mm/sec. As in Figure 3, the thrust force achieves its maximum value before the cutting force. The thrust force is less dependent on the depth of cut and more on the tool geometry. The average cutting force was 18.3 N and the average thrust force was 10.3

N. The picture in Figure 4 is representative of the vertical line at 58 seconds in Figure 5 and shows the forces at that point in time.
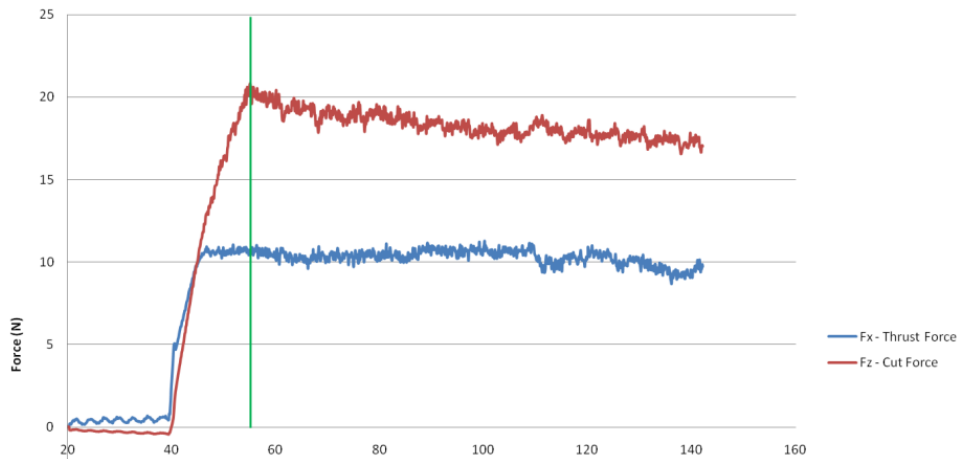
Figure 5: Tool forces when machining 6061-T6 aluminum at 25 μm depth of cut

Figure 6 shows the results for the 10 μm depth of cut performed on 1010 steel. The force data has been filtered to reduce the high-frequency features and show the main fluctuations in force over the experiment. There are two large drops in both the cutting force and the thrust force at 65 and 125 seconds. The chip image shows a kink in the chip that occurs when this drop occurs. It may be pickup of steel on the tool that makes the force rise and then expulsion of that pickup that creates the drop. More experiments are needed to study the pickup process.

7.3 CONCLUSIONS

Cutting experiments using aluminum have been performed for depths of 10μm and 25μm. Images of the chips at each depth of cut were collected with sufficient visual clarity to see the chip formation. Higher magnification of the chip images and higher speed collection will be required to see shear bands or pickup of material on the tool.

Machining experiments using 1010 steel were performed at 7 and 10 μm depths of cut. This steel was machined with carbide and diamond tools. The diamond tool produced a smooth clean chip while the carbide tool produced a discontinuous chip. The discontinuity of the chip explains the fluctuating forces observed with the carbide tool. With higher image magnification, visualizing the cause of these fluctuations with the diamond tool and steel workpiece will be possible. Once the cause can be determined for the diamond tool, the chip images can be compared to a model such as AvantEdge to see the flow and chip thickness.

1010 STEEL 25μm DEPTH OF CUT
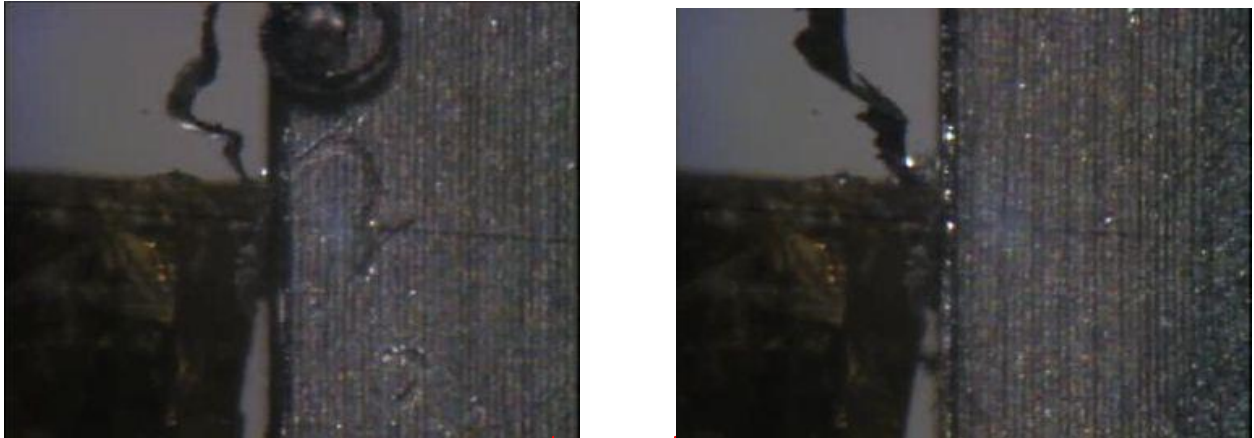
a) Image just after the first drop in force   b) Image just after the second drop in force
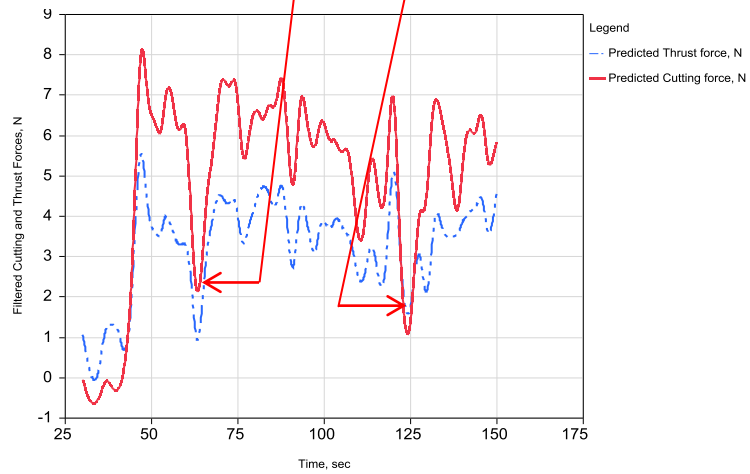
Figure 6: Diamond tool forces for 10μm depth of cut

REFERENCES

1. AvantEdge created by ThirdWave Systems, Inc of Minneapolis, MN

2. A. Koplev, Aa. Lystrup, T. Vorm, The cutting process, chips, and cutting forces in machining CFRP, Composites, Volume 14, Issue 4, October 1983, Pages 371-376.

3. Jiang Hua, Rajiv Shivpuri, Prediction of chip morphology and segmentation during the machining of titanium alloys, Journal of Materials Processing Technology, Volume 150, Issues 1-2, 1 July 2004, Pages 124-133.

4. A. Manna, B. Bhattacharyya, A study on machinability of Al/SiC-MMC, Journal of Materials Processing Technology, Volume 140, Issues 1-3, Proceedings of the 6th Asia Pacific Conference on materials Processing, 22 September 2003, Pages 711-716.

8 ULTRASONIC VIBRATION ASSISTED MACHINING

Neil VonHolle
Undergraduate Student
Brandon Lane
Graduate Student
Thomas A. Dow
Professor, Mechanical and Aerospace Engineering

An ultrasonic elliptical vibration assisted machining (EVAM) device was designed and tested as a summer undergraduate research project. This device utilized piezoelectric actuated resonator called a sonotrode to oscillate a diamond tool. The resonant frequency and vibrational tool path was determined using finite element modeling and the motion was corroborated using an infrared displacement sensor. The vibrating tool was then used to cut 6061-T6 aluminum and C360 brass. The resulting surface finish was poor possibly due to the compliant mounting of the sonotrode base and metal pickup on the tool flank face may have been caused by errors in the desired tool motion.
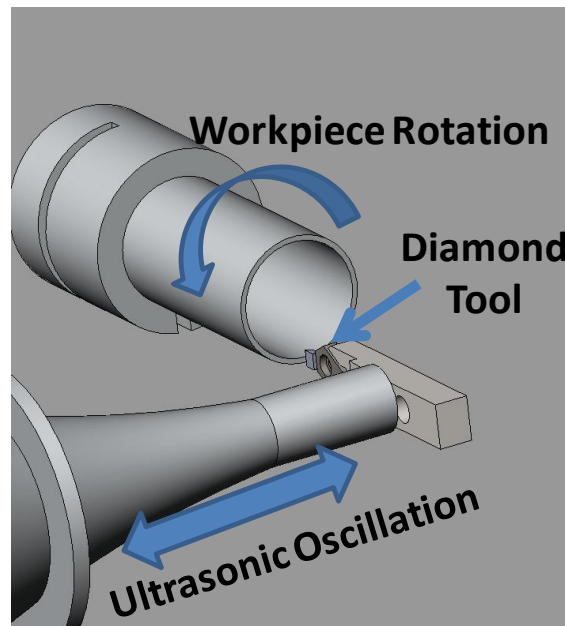
8.1 INTRODUCTION

Elliptical vibration assisted machining, or EVAM, is the process where a tool is vibrated in two orthogonal directions to create an elliptical path while machining a workpiece. The tool moves in the direction of cutting as well as perpendicular to that direction which increases and reduces the depth of cut. Because the tool can come out of contact with the workpiece, it is able to run cooler but at the same time more sliding occurs than for conventional cutting. The reported benefits of EVAM are decreased tool wear resulting in improved surface finish for longer cuts. More details of the research activities in this subject are in Section 6 of this report.

The basic properties that define the motion of the EVAM process are the dimensions of the tool ellipse, its frequency, the upfeed per cycle and the phase difference between the vibration directions. The ellipse dimensions are defined as the amplitudes of vibration in the cutting direction, *a*, and the vibration amplitude in the depth of cut direction, *b*. The upfeed is defined as the horizontal distance the tool moves between consecutive cycles and can be found by dividing the speed of cutting, V, by the frequency of vibration. The phase lag between the different vibration directions dictates the tilt angle of the ellipse where 90° creates an ellipse with amplitudes aligned with the x and z axis.

8.2 SONOTRODE

A sonotrode is an actuator driven at a ultrasonic frequency and includes a horn that amplifies this vibratory energy to perform some activity such as ultrasonic welding or cutting. For an ultrasonic welding or cutting application, the sonotrode gives energy directly to the welding contact area, with little diffraction that could damage surrounding electronic components. In the vibration assisted machining application described here, the sonotrode consists of a large diameter rod that is excited by a piezoelectric actuator. Attached to the end of that rod a section of decreasing cross sectional area whose length is related to the natural frequency of the driver. When the large end of a sonotrode is excited at its natural frequency, the amplitude of the small is amplified as the cross sectional area decreases. The shape and configuration of the sonotrode dictates the amount of amplification. The sonotrode used in this project was designed with an exponentially decreasing diameter from 48mm down to 12mm. It was machined to have a mounting flange at the theoretical node of vibration. A NTK D4427 PZT piezoelectric actuator is shown attached to the sonotrode in Figure 1. The actuator was sandwiched between sonotrode and an additional mass with a preload applied by a bolt. The driver is called a BLT or a Bolted Langvin Transducer.
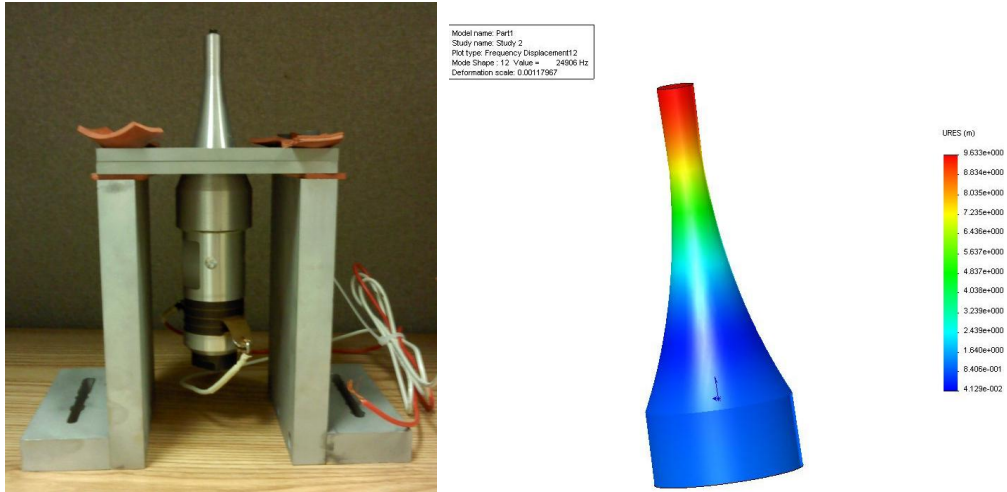
Figure 1. Sonotrode and FEA model

8.2.1 FE MODEL

A solid model of the sonotrode was created in SolidWorks and analyzed using the FE model, Cosmos. The natural frequency for longitudinal vibration predicted by the FEA software was 24,906 Hz. The node, or point at which the vibration amplitude equals zero, was located in the same place as the mounting flange on the sonotrode horn. The finite element displacement results are shown in Figure 1.
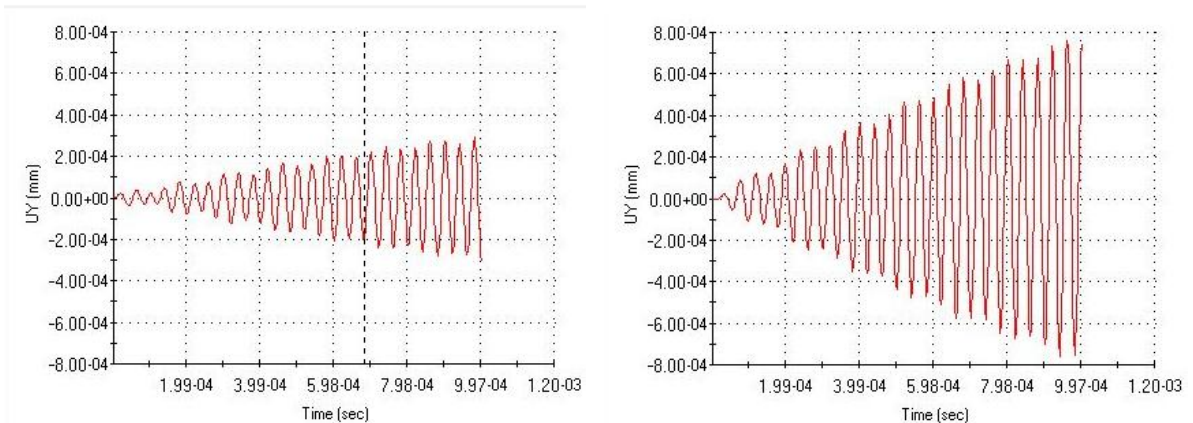
Figure 2. Model of the sonotrode at the piezoelectric actuator (left) and at the end of the reduced section (right)

Figure 2 shows the predicted amplitude of the sonotrode in the X direction from the FEM with a sinusoidal excitation force at its resonant frequency of 10 N. The left image is the displacement of the base or point of excitation and the right image is the amplitude at the small end. Both graphs are on the same scale to emphasize the 2.6x magnification of the vibration amplitude.

The phase difference between the point of excitation and the small end is 180° meaning that as the actuator moves to the right, the small end is moving to the left.

8.2.2 SONOTRODE VIBRATION ANALYSIS

To create both X and Z motion, an off-center mass in the form of a tool and tool holder was placed at the end of the tapered sonotrode. The actuator was excited using a function generator with a 3V output signal and an amplifier was used to magnify the voltage by 100x. The actuator excites the sonotrode at its natural frequency which vibrates the tool in the X direction. The off-center mass of the tool creates a moment at the end of the beam that adds the orthogonal Z motion. An optical sensor was used to measure the motion of the tool in the cutting (X) and depth of cut (Z) directions. The oscilloscope is used to record the input signal from the function generator as well as the output signal from the sensor.

The optical sensor is a light-based displacement sensor developed by Opto Acoustic Sensors that can be used to measure small displacements at frequencies up to 50 KHz. It works by sending near infrared light through a center emitting optical fiber and collecting the light reflecting off the surface by six optical fibers surrounding the emitter. The amount of light received depends on the standoff distance and this light is carried back by the receiving fibers to a photosensor and is converted to an output voltage proportional to the distance to the target.
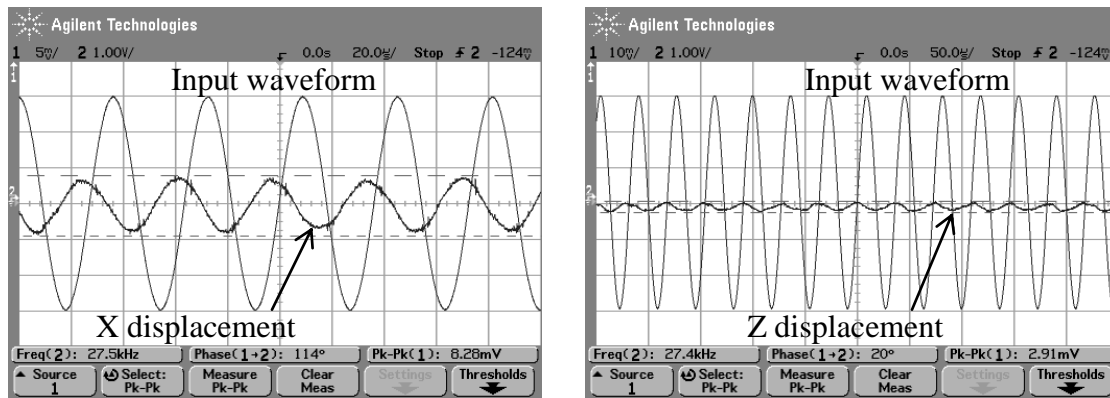
a) X direction motion at 27.5 KHz
b) Z direction motion
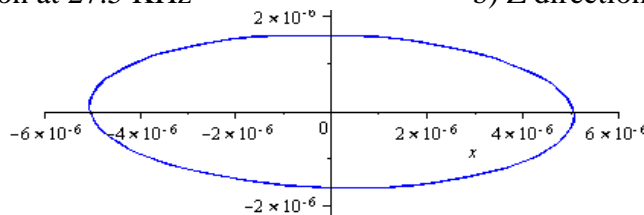
c) Elliptical motion of the tool defined from X and Z motion in a) and b).

Figure 3. X and Z motion of the tool and the combined elliptical path at 27.5 KHz

To determine the shape of the tool motion, two measurements were made of this motion in the X and Z directions; that is, the cutting direction and the direction of the depth of cut, respectively as shown in Figure 3. By measuring the motion in each direction, the tool path can be estimated based on the amplitude of the vibrations and the phase between them. Because the sensor had a single channel, each motion was measured separately and compared to the input signal to the amplifier for a phase measurement. Figure 3 shows the vibration of the tool at 27.5 kHz with a 10.1µm X amplitude, 3.23µm Z amplitude, and a 94° phase difference. Assuming sinusoidal vibrations, the tool motion at 27.5 kHz was plotted to approximate the elliptical vibration shape at the bottom of Figure 3. Sufficient detail was not necessarily available to know that they were pure sine waves and thus the elliptical shape of the tool motion is somewhat idealized.

8.3   CUTTING EXPERIMENTS AND RESULTS

Due to the size of the sonotrode tool and the limited amount of space on the Diamond Turning Machine (DTM), the optimum position of the sonotrode is shown in Figure 4. The actuator was mounted horizontally and parallel to the face of the spindle. The large amplitude of the vibration in Figure 3 will be in the direction of cutting and the smaller vibration will move the tool away from the workpiece. The workpiece was a thin tube with a wall thickness approximately half the thickness of the straight edge of the diamond tool. Figure 4 shows a solid model of this apparatus illustrating the tool, sonotrode, and workpiece mounted on the diamond turning machine as well as a photograph of the system.
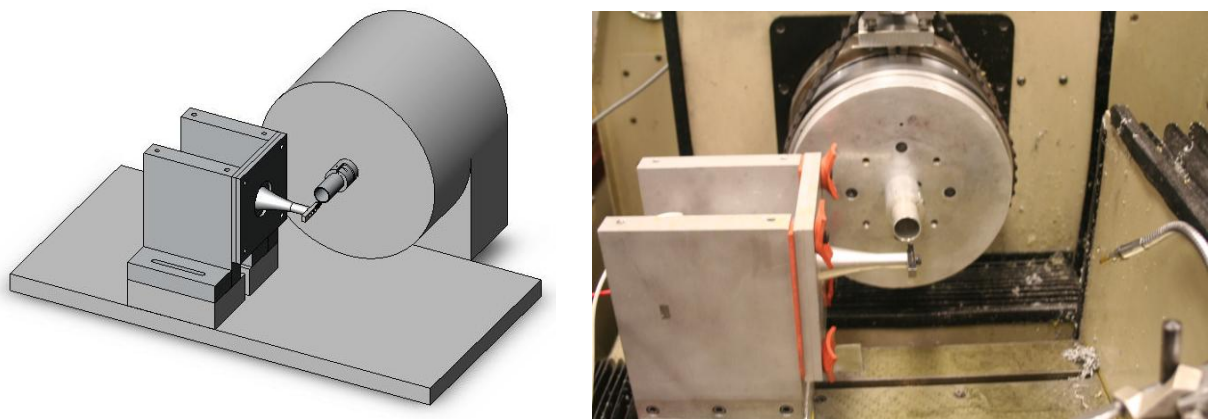
Figure 4. Solid model of the machining experiment and the actual setup on the DTM

For the cutting experiments, the cutting velocity was chosen as 50 mm/s with a 5 µm depth of cut. The system operated at 27.5 KHz frequency with the ellipse dimension shown in Figure 3. The cutting parameters are 1.8 µm upfeed per cycle, maximum chip thickness of 1.2 µm and a theoretical surface finish of 23 nm. To achieve these parameters, the DTM spindle rotated at

0.716 revolutions per second. This is too slow for the main motor so an auxiliary stepper motor was attached to the spindle to provide torque to handle the low turning speed.
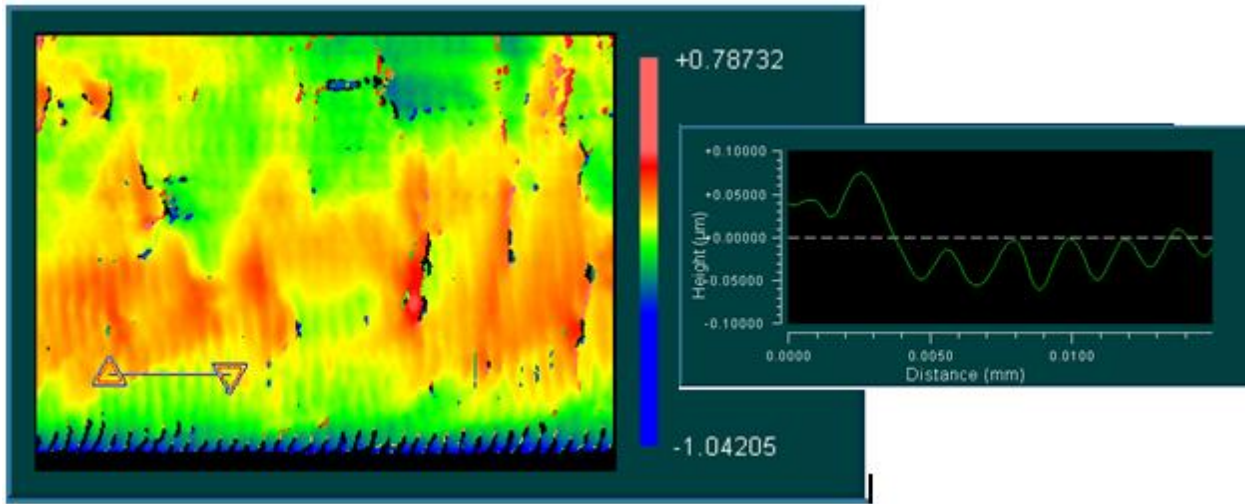
Figure 5. SWLI image of brass surface with features at the upfeed rate of the actuator

For the EVAM testing, two materials were machined; 6061-T6 Aluminum and C360 Brass. A white-light interferometer image of the brass substrate is shown in Figure 5. The main image shows the overall machined surface and the right hand image is a slice from this image marked in the lower left. The expected feature period of 1.8 mm is visible but many other features are also present with magnitudes that were much larger than expected.

8.4   TOOL HOLDER COMPARISON

To explain the magnitude of the surface features, the influence of the tool holder stiffness was evaluated. A pulley system was used to apply 1, 2 and 5 N forces to the tool in the cutting direction and the depth of cut direction. Both the deflection of the sonotrode tool and a standard diamond tool holder was measured. Figure 6 shows the deflection measured for each tool support and the slope of these lines are reported in Table 1.

Table 1. Stiffness for the Sonotrode and Standard tool holder.

Tool Holder	Stiffness, N/μm
Sonotrode Tool X direction	1.5
Sonotrode Tool Z direction	2.7
Standard Tool X direction	5.3
Standard Tool Z direction	8.0

The stiffness of the tool support in the sonotrode is significantly less than with the standard holder. In the X or cutting direction, the standard tool is 3.5 times stiffer and in the depth of cut direction Z, the standard tool is 3 times stiffer. The difference in this static stiffness is due to the compliant mount of the sonotrode in the mount. This may be partly responsible for the poor surface finish. .
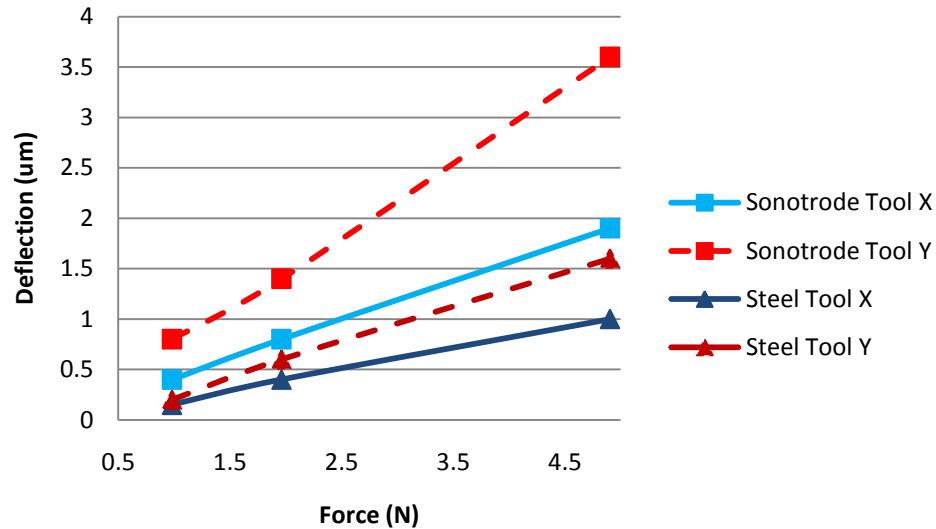
Figure 6. Tool deflection for the sonotrode and standard tool holders.

8.5 CONCLUSIONS

1. An ultrasonic actuator was built to study elliptical vibration assisted machining. The tool holder had a natural frequency of 25 KHz with an elliptical motion of 10 μm in the cutting direction and 3 μm in the depth of cut direction.
2. EVAM experiments were performed at the ultrasonic frequency and the results were encouraging but significant additional effort will be needed to make this design a precision tool.
3. The sonotrode structure was found to have low static stiffness in both the cutting and thrust force directions. This is likely due to the rubber supports that were built into the holder. However, the natural frequency added by these supports should be at a frequency much below the operating frequency and may have little effect on the elliptical shape.
4. Because a two-channel measuring probe was not available for the measurements, the tool motion in each direction had to be measured separately and the tool path was determined by assuming perfect sinusoidal motion at the measured phase angle. This assumption will not produce high-fidelity prediction of tool path.
5. Material buildup on the flank face of the tool may indicate that the tool was not moving in the expected ellipsoidal path. This may be due to an error in the assumed tool path or a

phase error in the direction of the tool motion with respect to the workpiece motion. If the tool was rotating in the wrong direction, the effect would be to have the tool "indent" the workpiece as opposed to "scooping out" the chips. If the latter hypothesis was true, it may be the cause of the tool pickup and poor surface finish.

9 NANOCOINING OF OPTICAL FEATURES

Erik Zdanowicz
Graduate Student
Dr. Thomas A Dow
Duncan Distinguished University Professor
Department of Mechanical and Aerospace Engineering
Dr. Ronald Scattergood
Professor, Department of Material Science and Engineering

The use of non-reflective surfaces in consumer and commercial manufacturing has become increasingly popular. Whether they are used to reduce reflection on a monitor or increase the efficiency of photovoltaic solar cells, the advantages are being recognized and the demand is increasing. The limitation of these non-reflective surfaces is the length of time required to produce a useable quantity, usually by deposition techniques. This paper describes an approach to creating non-reflective optical features with a high throughput.

The goal of this research is to create non-reflective surfaces through a process of nanocoining. Nanocoining using a nanostructured diamond die to imprint the non-reflective structure on to a mold surface. This type of manufacturing requires the design of an ultrasonic actuator (50 kHz) to produce the indentations at a high rate. The physical process of the nano-indentation is investigated to understand how material behaves at the nano-scale. A functional system will be produced by creating experimental indents and comparing them to FEA results while simultaneously designing a resonant structure capable of achieving the required displacements at ultrasonic speeds. The ultrasonic actuator along with the ability to create nanostructured features are the key elements to producing optical quality non-reflective surfaces efficiently.
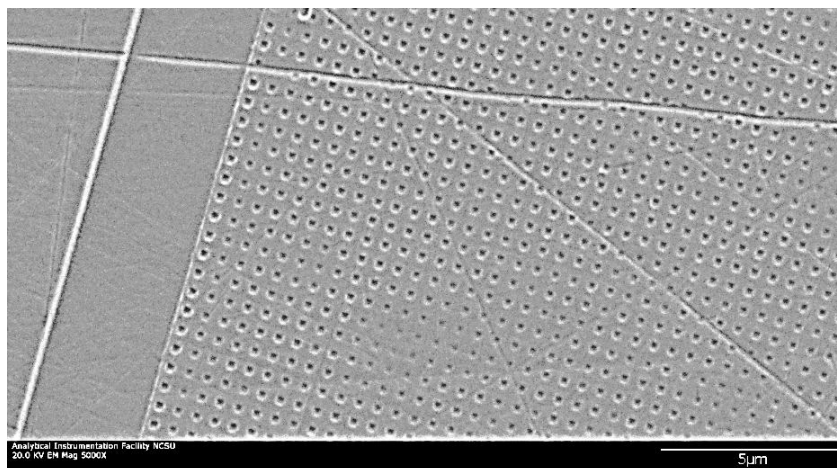
9.1 INTRODUCTION

The use of bio-inspired moth eye structures to decrease reflectivity of a surface has been achieved with a variety of feature shapes, sizes, and orientations. In order to define the surface that will be created by the nanocoining process, it is important to understand how these parameters interact to create an antireflective surface. Through the study of naturally occurring nano-features in certain insects, and the optical modeling of moth eye features, both naturally occurring and man-made, it is possible to define the desired coined surface for antireflection. This paper will review the optical theory and resulting constraints required for reduced reflectivity on the nanocoined surface.

9.1.1 BIO-INSPIRED OPTICAL FEATURES

The model for the features that will be created by the nanocoining process comes from the naturally occurring features present in the eyes of some insect species. These features, known as corneal nipples, are commonly found in nocturnal moths and diurnal butterflies. Corneal nipples are protuberances on the outer surface of the eye that have been found in a variety of shapes and sizes. They are typically hexagonally arrayed, but similar to grain orientation in materials, the orientation of the features is not perfectly consistent across the surface. Figure 1 shows the features and orientation shifts found on a typical moth eye surface [1].
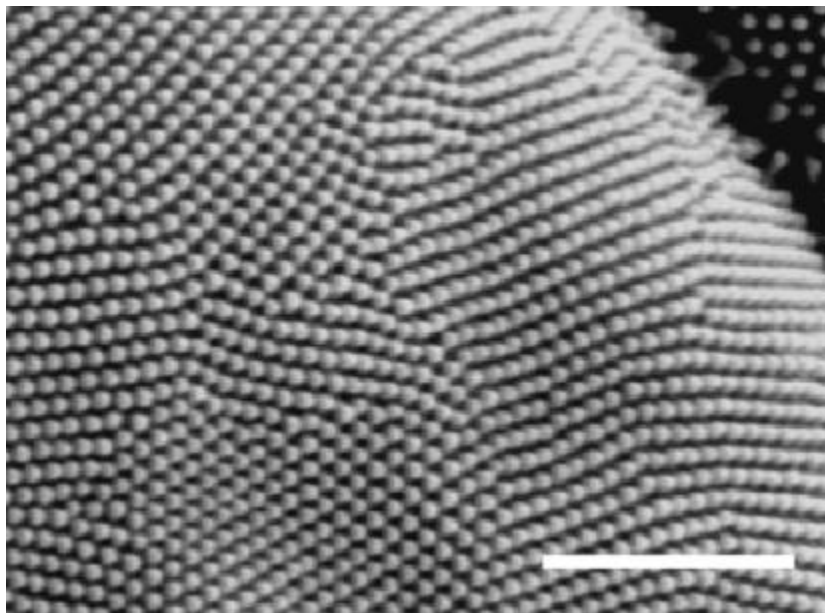
Figure 1. Corneal Nipple Array of Peacock Butterfly SEM image (Scale bar is 2 micrometers) [1]

Corneal nipples are usually found with maximum heights, h, around 250nm. The spacing between features, d, is generally between 175nm and 250nm. Stavenga [1] published simulations showing different feature profiles and heights, and the impact on reflectivity over the wavelength, λ, range of visible light, $300 - 700$nm.

This study uses the theory that the moth eye features create an optical layer where the ratio of material to air varies with distance from the top of the features to the base of the features. This ratio of air to material is directly related to the index of refraction. As a result, the index of refraction changes over the optical layer from that of air, 1, to that of the substrate material gradually through the optical layer [2]. This can be modeled based on the geometry of the features and the spacing of the features by taking the optical surface and dissecting it into many sublayers. An average index of refraction can be calculated for each sublayer and then the optical surface can be treated as stacked layers of thin film. Figure 2 shows how the optical surface can be divided into these sublayers.

Air

Substrate
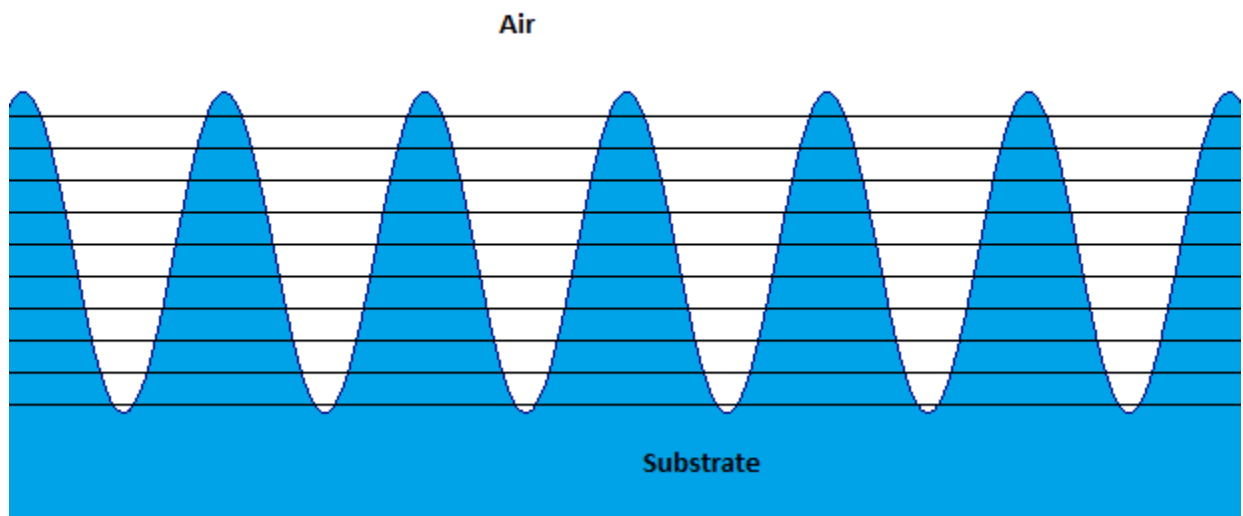
Figure 2. Cross section of optical layer dissected into thin sublayers for analysis

This analysis shows that taller features reduce reflectivity in moth eyes from around 4% (for 50 nm tall features) to less than 1% (for 250 nm tall features) across the entire visible light spectrum for all feature shapes examined [1].

Another study performed by Hutley and Wilson describes the dimension requirements of the optical layer for reduced reflectivity [2]. Theoretically, since each sublayer has a different index of refraction, the reflected light has a different phase at each depth. If the height of the optical

layer is at least half the size of the wavelength of the incident light, then all phases occur and destructive interference causes the reflectivity to drop to zero. The geometry of the feature, parabolic, cone, pyramidal or Gaussian profile, does contribute to this effect, but the minimum reflectance consistently occurs when the feature height is close to half the wavelength of the incident light [1]. This is shown in Equation (1).

$$h \geq 0.5\lambda_{max} \tag{1}$$

The feature spacing has a direct effect on diffusion of incident light at normal and oblique incidence. If the array is too widely spaced, then the optical layer will act as a diffraction grating. If the spacing, d, is small enough then the reflectivity will be minimized and the transmissivity maximized. Equation (2) describes how the wavelength of incident light, λ, and index of refraction of the substrate, n, affect the feature spacing, d.

$$d \leq \frac{\lambda_{min}}{2n} \tag{2}$$

Using this theory, the parameters for the target nanocoined surface are defined. The goal of this project is to make an antireflective moth eye surface for incident light in the visible spectrum. The minimum wavelength to be transmitted, λ_{min}, is 380 nm. The maximum wavelength to be transmitted, λ_{max}, is 780 nm. As a result the features in the optical layer should have a target height, h, of 390 nm and target feature spacing, d, of 190 nm.

9.2 DETAILS OF THE PROJECT

There are many considerations to account for to reach a functional system. Material effects such as strain rate and grain size must be discussed. Creating nano-featured indents and comparing the results to FEA simulations will provide a method to predict forces and material displacements caused by dies with different geometries. The indentation process itself is a challenging task. The die must imprint on a moving surface which means unless some kind of compensation is implemented, the imprints could smear. To avoid smear the actuator must not only be ultrasonic, but produce displacements in more than one direction. This is a very difficult task considering the required displacements of the die. These challenges have all been diligently addressed and the results will be discussed in the following sections.

9.2.1 EFFECT OF STRAIN RATE ON HARDNESS IN NANOCOINING

The rate of the die indentation proposed for nanocoining is on the order of 40 kHz. This means that the effective strain rate for making an indentation would be very high compared to conventional indentation testing. An estimate of the rate effect is appropriate to see if the rate has a large influence on the indentation forces. If it does, this would have to be taken into account in the design of the die actuator.

For spherical indentation the hardness H is related to the yield stress σ by the by the constraint factor c

$$H = c\sigma \tag{3}$$

$c \approx 3$ when the plastic zone fully encloses the indenter up to the free surface. It is between 1 and 3 when the plastic zone is constrained to the subsurface [2].

The strain rate effect in uniaxial tension or compression relates the yield stress to the strain rate $d\varepsilon/dt = \dot{\varepsilon}$

$$\sigma = A\dot{\varepsilon}^m \tag{4}$$

The constant A and the strain rate sensitivity m depend on the material and its condition (alloy content, cold working, grain size, etc.). An effective uniaxial indentation strain for spherical indentation is given by the ratio of the diameter d of the indentation projected on the free surface to the diameter D of the indenter [2]. For a fixed value of $\varepsilon = d/D$ in nanocoining, the effective indentation strain rate would then be

$$\dot{\varepsilon} = \frac{\varepsilon}{\Delta t} = \epsilon v \tag{5}$$

Δt is the mean time needed to produce an indent, which is $1/v$ where v is the nanocoining frequency. Combining these relations and assuming that the constraint factor c is a constant independent of indentation rate,

$$\frac{H}{H_o} = \frac{\sigma}{\sigma_o} = \left(\frac{\dot{\varepsilon}}{\dot{\varepsilon}_o}\right)^m = \left(\frac{v}{v_o}\right)^m \tag{6}$$

The subscript "o" denotes values for a conventional hardness test with respect to values for nanocoining. Taking $v_o = 1$ s^{-1} and $v = 40000$ s^{-1} for a comparison, ie., nanocoining at 40 kHz, the relative strain rate induced hardness increase for nanocoining would be $(40000)^m$ where m is the strain rate sensitivity in uniaxial compression or tension.

As a simple approximation of the material response, the value of m for large grain size pure copper is about 0.005 (grain size on the order of 10 to 20 μm or larger). The value of m increases with decreasing grain size and m would be about 0.015 for nano grain size copper, for example, electroplate copper. Using these values, the ratio H/H_o would increase from about 1.05 to 1.15 as the grain size of Cu decreases to the nanoscale. At the largest m value considered, this is only a 15% increase in hardness for nanocoining. This would not have a significant impact on the indentation forces during a nanocoining operation.

Figure 3 shows experimental data for compression tests on 150 nm grain size pure copper. The tests at the lower strain rates (solid points) were obtained from uniaxial compression tests and the values at higher strain rates (open points) were obtained using the Hopkinson split bar technique [4]. A yield stress increase of about 33% is obtained at the highest-to-lowest strain rate ratio of 1.1×10^7. This is consistent with an average m value of 0.0176 for the copper, in agreement with the approximate analysis presented in this section.
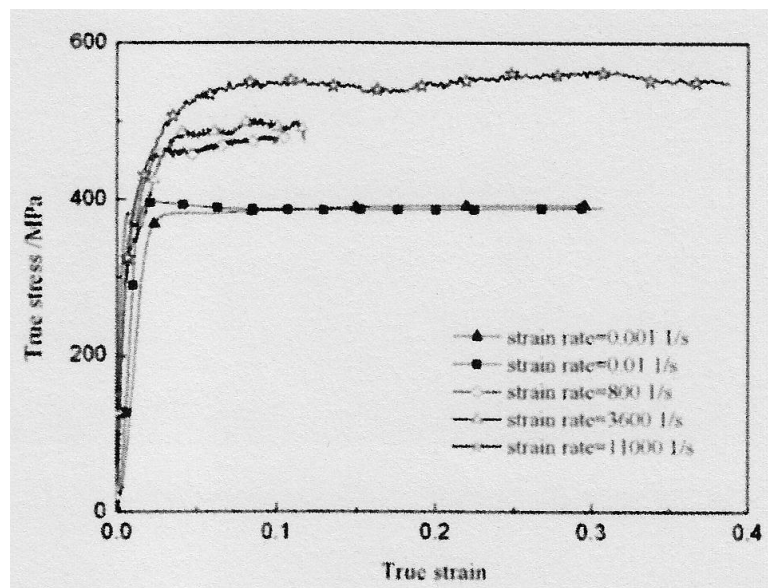
Figure 3. Compression tests (filled data points) and Hopkinson bar test (open data points) for tests done at 293 K on pure copper with an average grain size of 150 nm [4].

9.2.2 EXPERIMENTAL INDENTATIONS

Real indents were created for comparison with an FEA model. The goal is to have confidence that a die producing indents with attractive material deformation can be designed using FEA software (ANSYS). This is essential since the dies are constructed by use of Focused Ion Beam (FIB) machining diamond blanks. As a first step, a Rockwell indenter was used.

Rockwell Indenter Tests

A Rockwell indenter was chosen as a starting point because of they are inexpensive, readily available and have a simple geometry. Although a Rockwell indenter may look like a cone, there is a 200 μm radius spherical tip. It is this part of the geometry that was used for the experiments and models. Using only the spherical tip of the Rockwell indenter (limited by force) several indents were made on a sample of 6061 Al.

A displacement based model was created in ANSYS to compare load vs. indention depth. This implies that the indenter geometry was displaced a certain amount and the resulting forces from the contacting faces were calculated. This process was repeated until a certain depth was reached, after which the indenter was removed from the material leaving a plastically deformed indent. A bilinear isotropic material model was used to capture the effects of plasticity and strain hardening. The model which exploits the symmetry of the geometry can be seen in Figure 4.
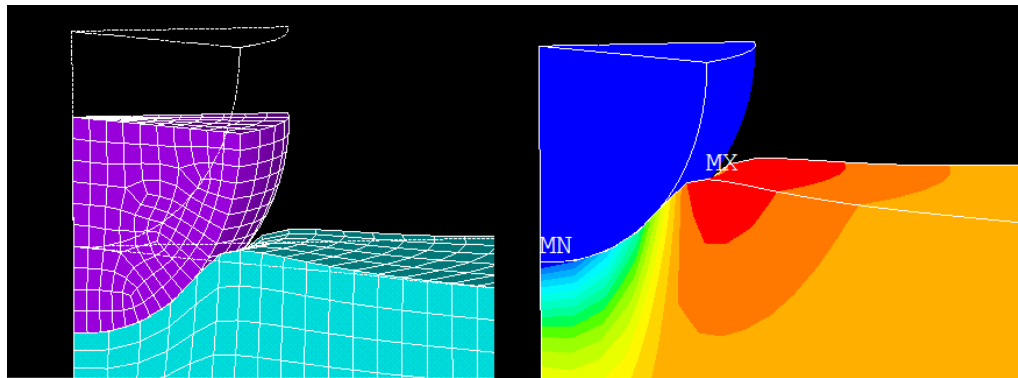
Figure 4. ANSYS simulation results of indentation using spherical portion of a Rockwell hardness indenter.

The experimental indents were measured with the Zygo Scanning White Light Interferometer (SWLI) and the results compared with the FEA simulations can be seen in Table 1.

Table 1. Results of Rockwell indents and FEA simulation.

Mass (kg)	ANSYS (μm)	Experimental (μm)
0.2	1.5	1.4
0.4	2.8	2.9
0.52	3.4	3.2
0.62	3.6	3.9

Table 1 shows that, for the Rockwell indenter, the ANSYS model correlates well. The next step was to scale down to a more applicable indenter size.

3M Flat Die Indents

The next set of indents was created using a diamond die with a 100 x 100 μm flat, square face. This tool was essentially a blank and provided for practice before using a nanostructured die which has time and effort invested. A rendering of the tool and tool holder can be seen in Figure 5.
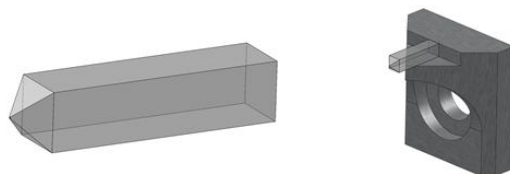
Figure 5. Flat diamond die and holder provided by 3M.

Indents would be created using the Nanoform 4-axis precision machine. The Nanoform has 3 translational axes (x, y, and z) and a rotational axis (not used for indents). An electroplated copper sample was used as a work-piece because of the small grain size. The work-piece was mounted to a block fixed to the x-axis. A load cell was placed between the work-piece and mounting block so indentation forces could be measured. The diamond tool was then attached to the y-axis tower of the Nanoform. The y-axis tower resides on the z-axis of the Nanoform. The z-axis was used to move the die into the work-piece and the x and y axes where used to move the die to a new indentation position. Figure 6 shows the experimental setup on the Nanoform.
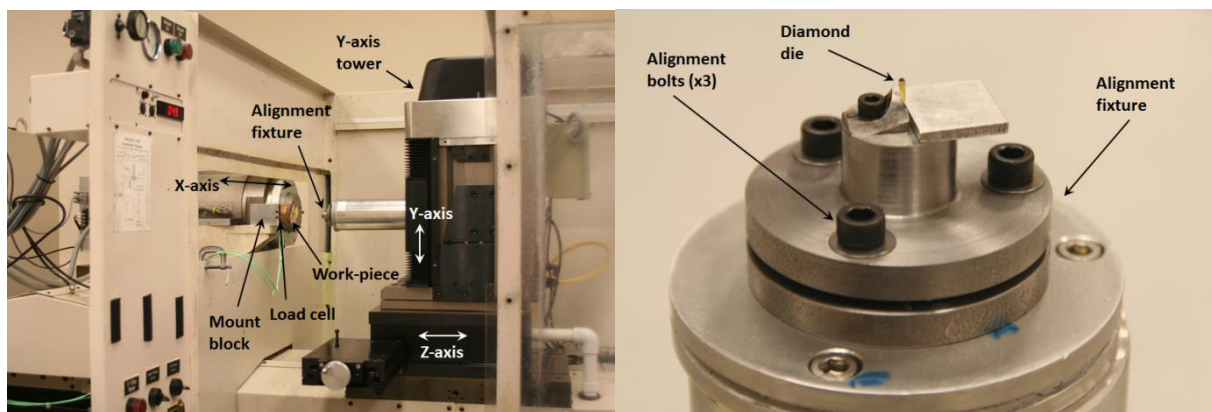
Figure 6. Experimental indentation setup on Nanoform (left) and alignment fixture (right).

Figure 6 also shows an alignment fixture that allows rotational adjustments of the die. This feature is required to ensure the flat face of the die is parallel to the flat work-piece face. If the

work-piece and die are not parallel, one side of die will be pressed in further than the other. This is an issue because the indentation depths are very small (hundreds of nanometers) compared with the length of the die (100 µm). For example, if the die had nanostructured features with a height of 250 nm and was 100 µm long, an angle of 0.14^{o} between the work-piece and die would be large enough to make some features on the die not touch the surface of the work-piece.

Adjusting the alignment fixture so that the die was parallel to the work-piece was a complicated task that took a few iterations to develop a procedure that would ensure aligned indents. The alignment procedure begins after the alignment fixture is bolted to the y-axis of the Nanoform and the load cell is calibrated. The first step is to attach an LVDT gage to the cylindrical piece holding the alignment fixture. The LVDT is then swept in the x and y directions across the face of the work-piece. This process provides the angles θ_{xz} and θ_{yz} which are the tilt angles in the x-z plane and y-z plane respectively. The LVDT is then attached to the mount block and swept across the flat measurement surface on the alignment fixture. The point of this step was to impose the tilt angles of the work-piece on to the alignment fixture. If the angles did not match, the alignment bolts on the fixture were adjusted accordingly.

With the die aligned, indents were made by manually jogging the z-axis until a certain force was produced on the load cell (22 N). This is a tedious task because the edges of the die face are not parallel to the motion of the Nanoform axis which means the sine and cosine errors from this offset angle must be accounted for. An automated program was developed to create a large (10 x 10) array of indents. The load cell cannot be used as feedback because the operating software on the Nanoform runs independent of the data acquisition computer that reads the force from the load cell. A MATLAB program was written to account for the die rotational misalignment (approximately 8°) and the tilt angles of the work-piece. A starting indent was created by jogging the z-axis until a certain force was reached. At this point, the x, y, and z coordinates were recorded. These coordinates were input to the MATLAB program which calculated commands to create a square array of indents in G-code (machine code). The G-code file was then executed on the Nanoform and the results can be seen in Figure 7.
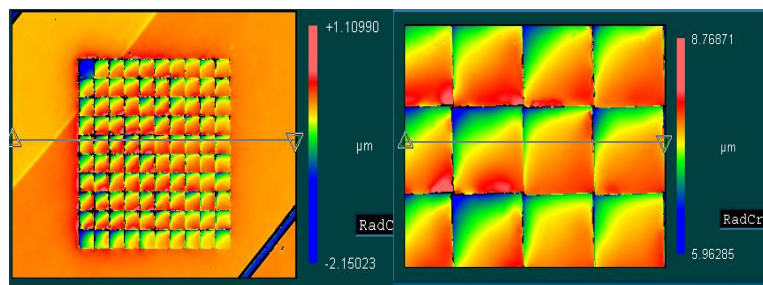
Figure 7. 10x10 square array of indents using the 100 µm square flat die (left) and a magnification (right).

97

The 1mm square block of 100 indents is aligned well in the plane of the page but there is a tilt of the die relative to the work-piece. It should be noted that this block was created before the final alignment procedure was developed. An unexpected feature observed upon measurement of the indents is that there was a significantly larger amount of plastic deformation around the edge of the indents. This additional plastic deformation can be seen in Figure 8 which is a trace of the right hand image in Figure 7. The additional edge deformation is from the stress concentration caused by the sharp corner at the edge of the die. This will be discussed more in the nanostructured die indents section.
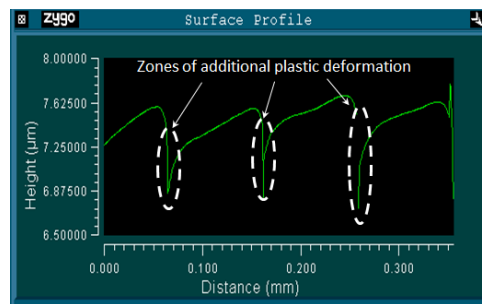
Figure 8. Trace of right measurement in Figure 7 depicting additional deformation at edge of indent.

3M Nanostructured Die Indents

The experience gained from the experiments with the flat die provided confidence that indents could be made using a nanostructured die. Once again, 3M provided the diamond die, this time with features created on the face using a Focused Ion Beam (FIB). Scanning Electron Microscope (SEM) images of the die are shown in Figure 9.
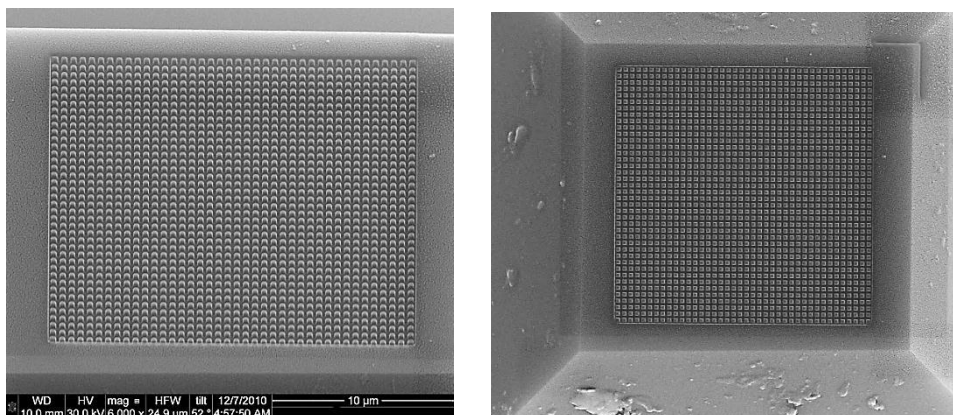
Figure 9. SEM images of nanostructured die provided by 3M Corporation.

The left image in Figure 9 shows a closer, slightly tilted view of the nanostructured die. The die consists of a square inner region containing a 40x40 array of square features. Each feature is approximately 300 x 300 nm in cross section and 250 nm in height. Spacing between features is 200 nm. The right image in Figure 9 is orthogonal to the die face and shows a square boarder around the inner region containing the nano-features. The outside dimensions of the boarder are approximately 25x25 nm. The surface of this boarder is the same height as the tips of nano-features and is used as an alignment indicator when measuring with the Zygo SWLI. The same procedure used to create the array of flat indents was used to create an 11x10 array of nanostructured indents. One of the indents in the array measured by an SEM can be seen at different magnifications in Figure 10.
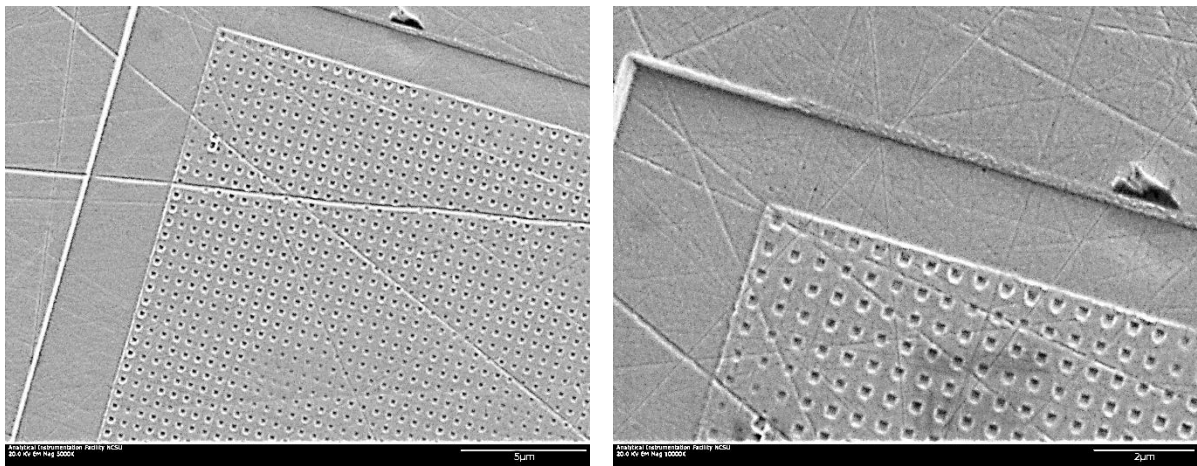
Figure 10. Single nanostructured indent measured with SEM at 5000x (left) and 10000x (right).

Figure 10 is an SEM image of a single indent in a corner of the array. The material above and to the left of the boarder is a non-indented surface. The SEM images show the border and nano-features clearly although depth dimensions cannot be determined. The most significant piece of information the image provides is the presence of the additional plastic deformation at the edge. This can be seen by examining the two scratches that cross each other in the left image of Figure 10. The scratches were present on the surface before the indent so it has been pushed down with the rest of the surface. However the scratch seems to disappear at the edge of the border and un-deformed material. This is because the material has been deformed more at this edge from the sharp edge stress concentration. Fabrication of future dies will have to compensate for the uneven contact stress created by flat dies. A way to compensate for this is discussed in the next section.

99

While SEM imaging is an effective way to measure 2-D features, the nanostructures are three dimensional and all three dimensions are important when considering the criteria for a non-reflective surface. A way to measure all three dimensions at once is by using an Atomic Force Microscope (AFM). An AFM is essentially a nano-scale profilometer that rasters over an area of a surface. Figure 11 is an AFM measurement of 1.5x1.5 µm patch located in the nanostructured area of the indent shown in Figure 10.
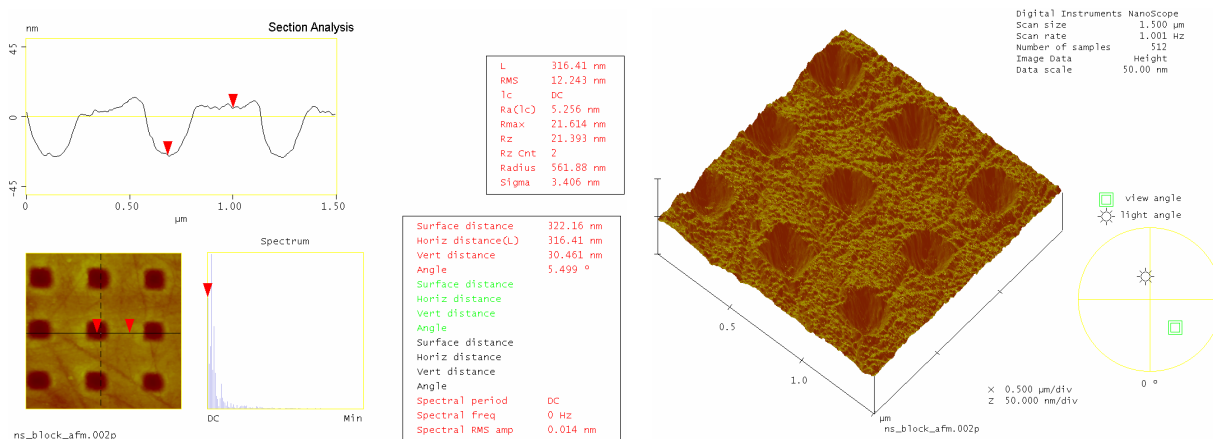
Figure 11. AFM measurement of nanostructure features (left) and 3-D rendering (right).

The left image in Figure 11 is a profile trace across the pockets created by the nano-features on the die. The data from the trace indicates that a depth of approximately 30 nm was reached. This was far from the total height of the nano-features so future indents will have to be performed to ensure the die has been indented to full depth.

9.2.3 FEA SIMULATIONS OF NANOSTRUCTURED DIE INDENTS

One of the goals of this research is to develop an accurate FEA model of the indentation process. This will provide a better understanding of how the material will deform and what can be done to influence material behavior. An example of material behavior that requires attention is the additional plastic deformation observed at the edge of the indents. Before compensation techniques can be applied a simulation must be developed to accurately model the nanostructured die indents.

The FEA model was created in ANSYS using 2-D geometry for computational purposes. The model takes advantage of geometrical symmetry so only half of the indenter and work-piece were modeled. Material properties for diamond and electroplated copper were used for the indenter and work-piece respectively. A bilinear isotropic material model which included strain

hardening was used for the copper work-piece. This plasticity model uses an elastic modulus for the elastic region of deformation and a tangential modulus for the plastic region. These two properties are the slopes for the two lines (bilinear) modeling elastic-plastic material behavior. Four node 2-D plane elements supporting contact and target assignment where used for both the indenter and work-piece. When the simulation is run, the work-piece is held while the nodes on the top surface of the indenter where displaced downward in increments of 10 nm until the desired depth was reached. The nodes on the top of the indenter where then moved upward revealing a plastically deformed work-piece surface. The total depth of the indent was chosen based on an experimental indent measured with the Zygo SWLI. The measurement and simulation results are shown in Figure 12.
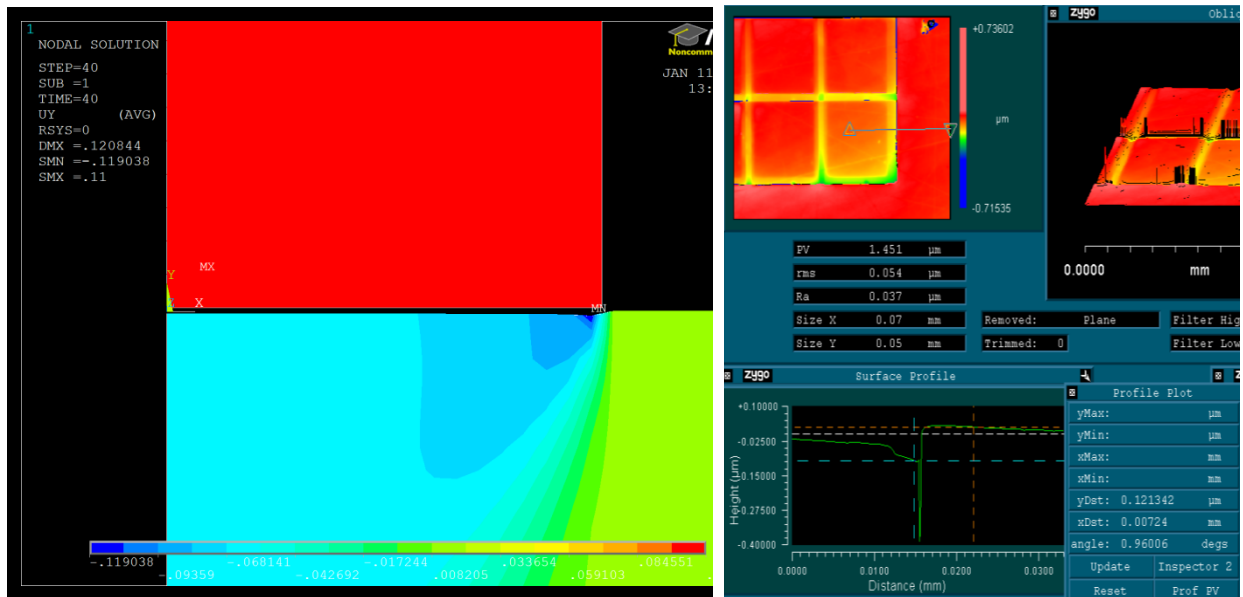
Figure 12. FEA simulation of nanostructured die indent (left) and experimental indent (right).

Although it may be difficult to determine the scale in the simulation results shown in Figure 12, deformation near the center and at the edge replicates the measurement data. Both see a deformation near the center and edge of the die of approximately 55 nm and 120 nm respectively. Alterations could now be made to the geometry of the die with confidence that the simulation results will be accurate.

The high concentration of stress at the edges of the die is a behavior detailed in many plasticity textbooks. The most intuitive way to relieve this concentration is to replace the sharp corner with a radius. FEA simulations proved this is an effective way to distribute the contact stress from the corner. A slope in the plastic deformation was still observed so another radius, this one much larger, was created over the entire surface of die. The combination of the small radius at

the edge and large radius over the entire face produced a nearly uniform contact pressure under the face of the die as shown in Figure 13.
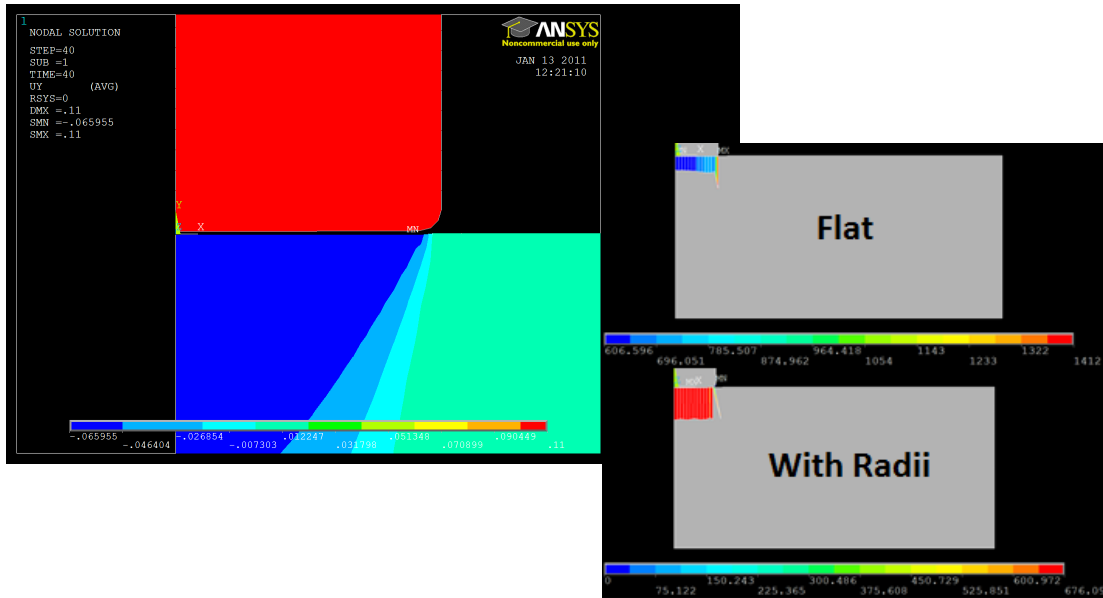
Figure 13. FEA displacement of multiple radii die (left), comparison of contact stress (right).

Figure 13 shows the results of the simulation run with a die that has two radii. The solution method is the same as for the flat die but the results are much more uniform due to the near linear contact stress across the face of the die. The top right image of Figure 13shows the contact stress of the flat die. The stress near the center and edge are 606 MPa and 1412 MPa respectively. The stress at the edge is more than twice the stress at the center. The contact stress of the die with multiple radii (shown in lower right of Figure 13) has a maximum stress of 676 MPa. The variation is not distinguishable because range of the color bar. This is evidence that altering the face of the die by adding two radii will produce a more favorable indent. The FEA simulation allowed this problem to be addressed by trying potential die shapes.

9.2.4 CHARACTERIZATION OF TOOL MOTION

The objective of this research is to develop an indentation system that will not only produce features with optical fidelity but do so at a high rate. To accomplish this task the work-piece must travel at a constant velocity. This implies that a die stroke orthogonal to the work-piece will not work because of the difference in velocities between the die and work-piece at the time

of contact (die not moving in direction of work-piece). A difference in velocities when there is contact for some amount of time, $\varDelta t$, will cause smear as shown in Figure 14 where V_{xDie} is the horizontal velocity of the die and $V_{xWork-piece}$ is the horizontal velocity of the work-piece.
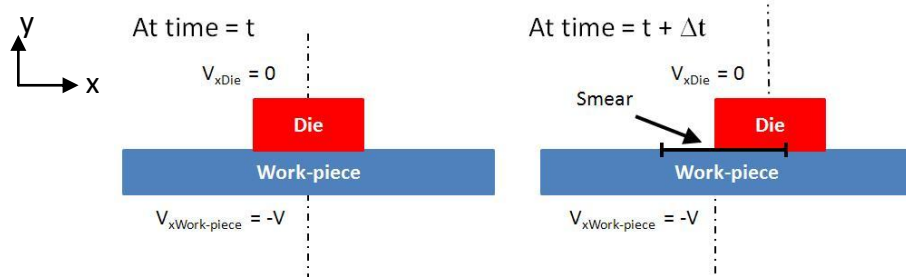
Figure 14. Smear caused by orthogonal die actuation.

To accommodate for the velocity difference the die must travel in the *x*-direction to match speed with the work-piece. The die must also be able to change direction and travel back to its origin so there is no over-lap or gap between successive indentations. With these stipulations in mind the ideal shape is an ellipse where the maximum velocity in the *x*-direction matches the work-piece velocity. Figure 15 shows the die's velocity as it moves through one elliptical cycle.
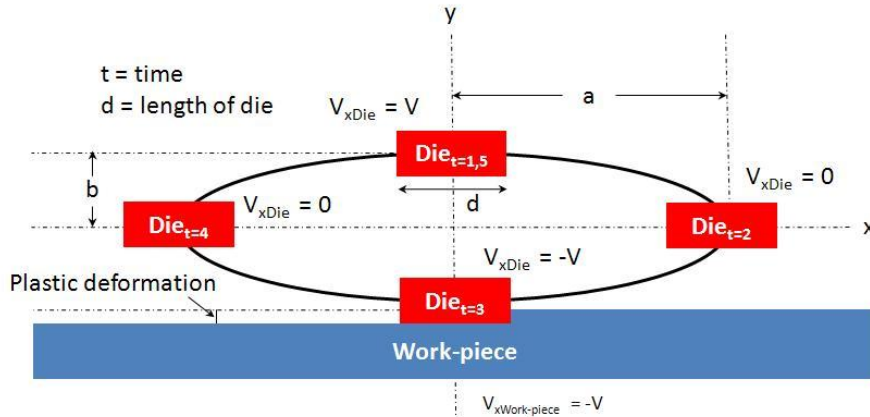
Figure 15. Elliptical motion of die for one cycle.

The motion of the die along the path must be well choreographed with the speed of the work-piece in order to minimize smear and produce equally spaced features. Therefore, relationships between the die and work-piece's position and velocity must be established

A model of the die motion with respect to the work-piece was developed to gain an understanding of which properties of the motion affect the overall performance. The *x* and *y* positions of the die where modeled by

103

$$x(t) = a\sin(\omega t) \tag{7}$$

$$y(t) = b\sin\left(\omega t + \frac{\pi}{2}\right) \tag{8}$$

where ω is the frequency of oscillation, t is time, a is the amplitude of the ellipse in the x-direction and b is the amplitude of the ellipse in the y-direction (Figure 15). Equations 7 and 8 can be used to relate the position and velocities of the die and work-piece. The result is a model with three defining variables which are the length of the die, frequency of indentation and velocity of the work-piece. A change in any one of these variables will cause the other two to change for a system were the indentations are sequentially aligned. Figure 16 shows a simulation of the system as a function of the die length, frequency and work-piece velocity.
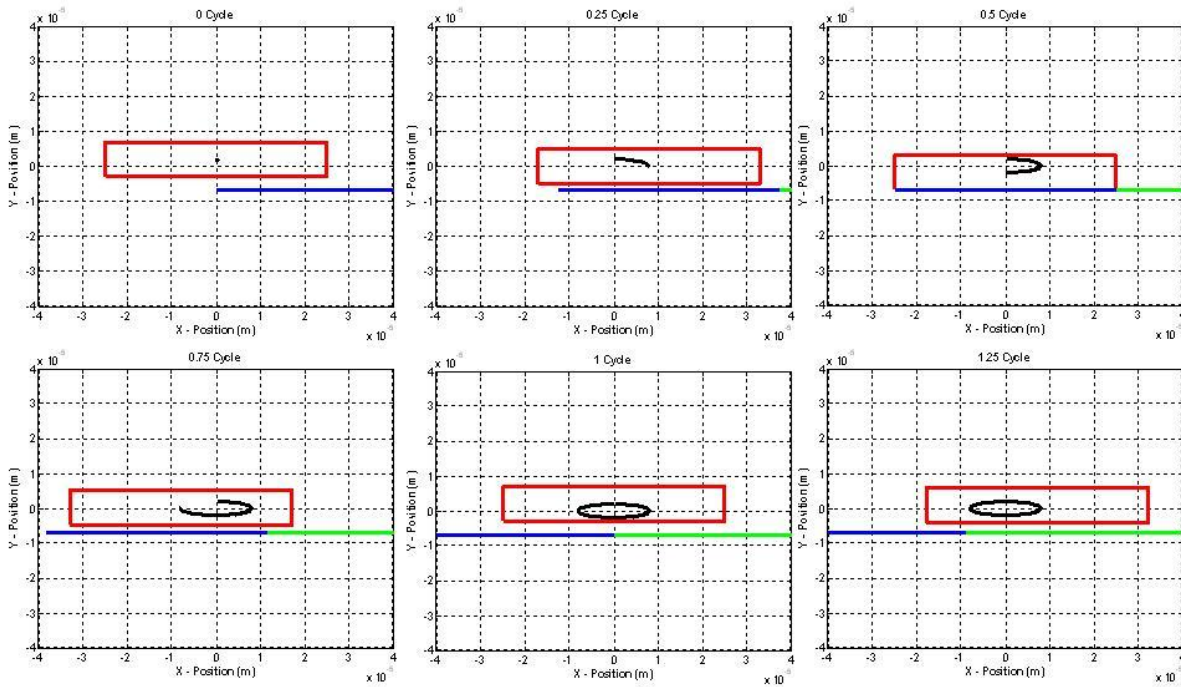
Figure 16. Simulation of elliptical path while indenting work-piece moving at constant velocity.

The different color line segments of the work-piece in Figure 16 represent successive indentations (which equal the length of the die). When the simulation is run at speed, the red box (die) will contact the work-piece at each line segment, one per cycle, meaning no overlap or gaps. The simulation also implies that the dimension, a, is fixed for a given die geometry and frequency. The dimension, b, is free to be adjusted which will be seen when error is examined. Future work includes developing and actuator that is capable of producing the desired elliptical shape.

Smear Error Relationship between Ellipse Dimensions

Figure 16 shows a 'long' tool path which implies the 'a' dimension of the ellipse is larger than the 'b' dimension (if $a = b$ then the path is a circle). Even though the tool is moving in an elliptical path there will still be some amount of smear since the die will come into contact with the work-piece before the die reaches its maximum x-direction velocity (refer to Figure 15 for variable definitions). Initially it was assumed that the long ellipse would be the best tool path shape. Error analysis was performed by simply calculating the difference in die and work-piece velocity when the two are in contact. This error analysis was performed for different dimensions of b since a is a fixed dimension. The results showed that a 'tall' ellipse (where the b dimension is larger than the a dimension) produces less error than the long elliptical tool path. This property can be easily understood if the x-velocity and total cycle time are considered in Figure 15. The x-velocity in the long ellipse takes longer to reach maximum velocity (work-piece velocity) than a tall ellipse. This implies that for a tall ellipse, the die accelerates faster and is in contact less amount of time than the long ellipse. The relationship on how the b dimension influences the error is shown in Figure 17.
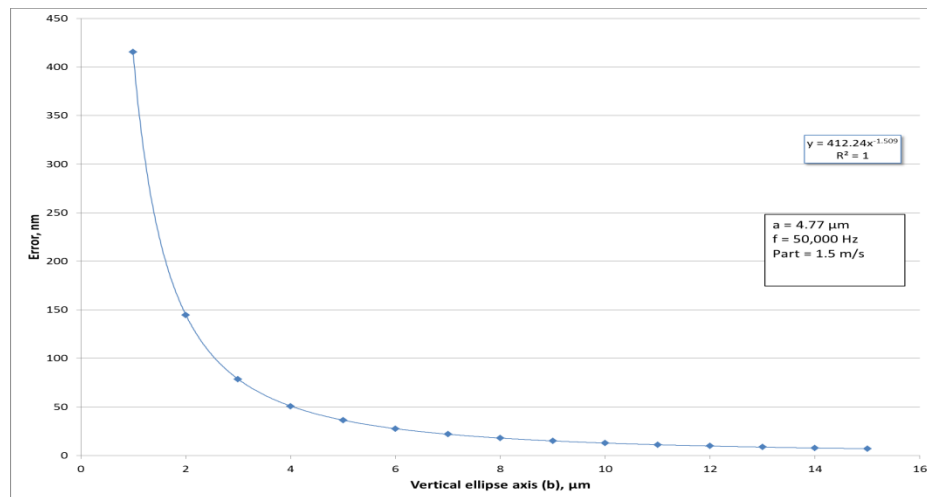
Figure 17. Smear error (nm) vs. the vertical ellipse dimension, b.

Figure 17 shows that as the b dimension increases, the error decreases. The b dimension cannot be very large however since these amplitudes are difficult to achieve at a 50 kHz actuation frequency. Therefore, vertical amplitude of 8 μm was chosen for 4.77 μm horizontal amplitude. To achieve these large amplitudes (relative to operating frequency) in two directions, an ultrasonic actuator has to be designed that can generate this motion without tilting the die and creating misalignment.

9.3.5 ULTRASONIC ACTUATOR DESIGN

The actuator for the nanocoining process must operate at 50 kHz and produce motion in two directions. The choice of actuator types is limited at such high frequencies so an ultrasonic resonant piezoelectric actuator was selected. This type of actuator uses piezoelectric material (PZT) to vibrate a structure at its resonant frequency. PZT material has a very high bandwidth and operating at resonance will produce amplification in displacement that is required by the specified tool path. After developing different models and simulating their response to a PZT actuation, a challenge arose in every design. The challenge is how to keep the die from rotating during actuation. Referring to Figure 15, the desired motion of the tool is rigid body translation in two directions. Any type of rigid body rotation of the die could generate misaligned indents. The initial actuators were designed to use two mode shapes to generate the motion amplification in two directions. These mode shapes were a longitudinal and bending. The first design (Figure 18) is a combination of three ultrasonic horns connected at a center tool holder.
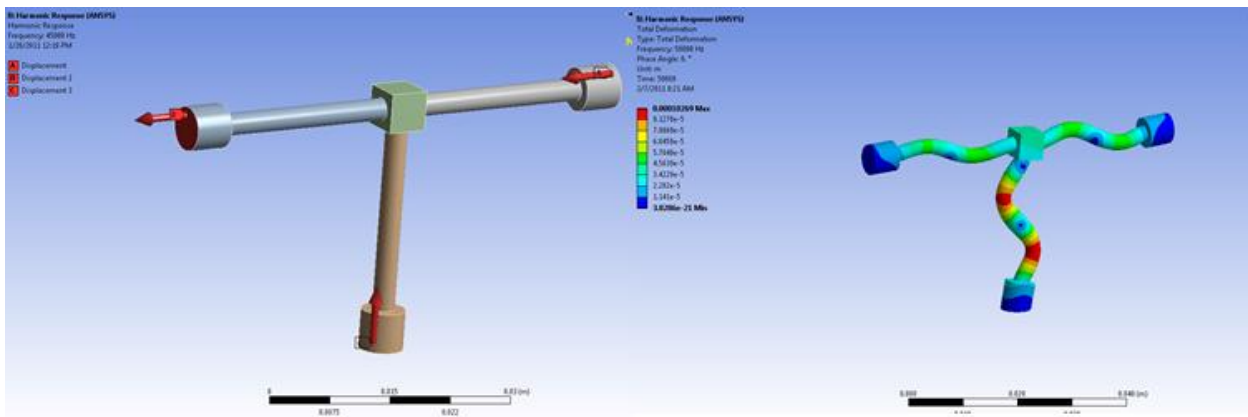
Figure 18. Three ultrasonic horn actuator design and response.

The ultrasonic horn shown in Figure 18 is a type of mechanical amplifier used to achieve large displacements. The amplification is a function in the change in radius from the base to the tip. The right image of Figure 18 shows the harmonic response to a sine wave at 50 kHz. This actuator will generate the desired displacements although there is some tilt when the actuator is not in the indentation part of its cycle. The indent would have to take place precisely at the right point to have an acceptable result. This actuator will produce the displacement necessary for the required indents but because of the additional rotation, other options will be considered.

Another design for the ultrasonic actuator was inspired by former Precision Engineering Center student Markus Bauer. Bauer created an actuator out of a solid piece of piezoelectric material. By poling the material correctly and placing electrodes (locations of actuation) at correct

positions, he was able to actuate the structure at a longitudinal and bending mode simultaneously. Using the same concept, an actuator for the nanocoining application was designed by first starting with a beam with fixed supports at each end. The dimensions of the beam were chosen based on the material properties and desired frequencies. The model shown in Figure 19 was the result.
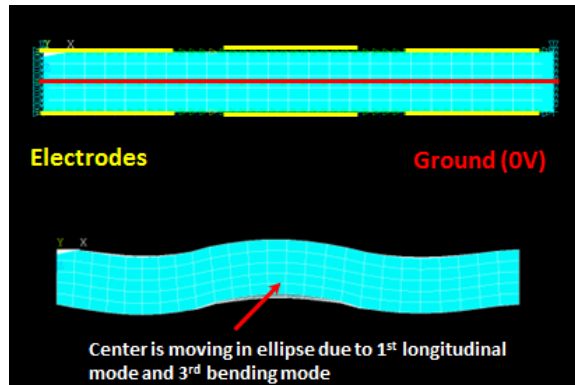
Figure 19. Model and simulation response of resonant PZT beam actuator.

The beam is modeled as if two PZT layers were epoxied together. An electrode runs down the center of the beam and functions as a ground. Six electrodes, three on the top and three on the bottom, are placed on the outside of the beam. The center of the beam can then be actuated in an elliptical path by applying voltages at these electrodes and varying the phase. The disadvantage of this approach is that the displacements are too small. The advantage of the beam is that its frequencies are well characterized and this feature was used to develop another concept.

The previous model used a longitudinal and bending mode of a beam with fixed ends to produce elliptical motion. A variation on this design uses a beam with a square cross section fixed at both ends. The length and cross section were chosen so the first bending mode was at 50 kHz. Since the cross section is square there are two bending modes at 50 kHz whose directions of displacement are orthogonal. Actuating the beam in both directions causes the center of the beam to move in an elliptical path.

A source of actuation that has been researched is through a Bolted Langevian Transducer (BLT). A BLT is composed of two masses with PZT material between them. A bolt is then used to clamp the two masses together compressing the PZT material. The resulting structure is in essence a spring-mass system whose natural frequency is based on the masses and bolt/PZT material. An image of a BLT can be seen in Figure 20.

Figure 20. Image of BLT. Two aluminum masses bolted together with PZT material between.

A BLT such as the one shown in Figure 20 can be used to actuate the beam with 50 kHz resonant frequency. There has to be an interface/fixture connecting the beam to the BLT which supports the beam as specified in the model and remains stiff enough not to add additional modal influences. The system shown in Figure 21 was designed so that the beam is embedded in the end of the fixture. This fixture is then bolted to the BLT and the entire assembly is supported by a flange. The flange is located at one of the nodes of the 50 kHz mode shapes so as not to influence the dynamics.
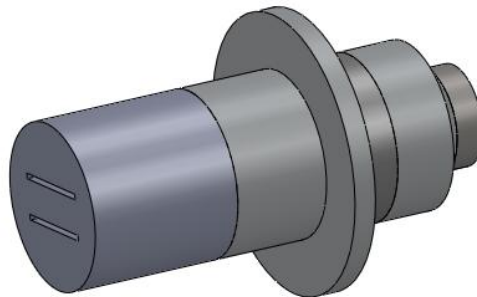
Figure 21. BLT with beam fixture attached and support flange at node location.

The actuation of the assembly in Figure 21 has not yet been fully designed as most BLTs are actuated in one direction. However, it is known that BLTs have been created with PZT material poled off axis. Actuating these types of PZT rings generate motion in two directions which is required for the nanocoining application. Further investigation into these PZT rings is ongoing.

9.3 CONCLUSIONS

The creation of non-reflective surfaces with high fidelity features at a rapid rate is emerging area of research. These non-reflective sheets have a variety of applications and the ability to produce

108

them in mass quantities will broaden their use. Nanocoining non-reflective surfaces are an alternative method to the deposition techniques that are currently being used. Nanocoining surfaces are possible by using a ultrasonic 50 kHz resonant actuator to indent a diamond die into a mold material. Experiments have shown that indenting nano-features into a copper work-piece is possible and an experimental procedure for aligning the indents has been established. FEA models have been developed that accurately model the experimental indents and will be used to optimize the die geometry for uniform indents. FEA is also being used to simulate how different actuator designs perform at resonance. Future research includes examining how subsequent indents affect each other as well as how to produce desired motion from the actuator designs.

REFERENCES

1. Stavenga, G. C., S. Foletti, G. Palasantzas and K. Arikawa, *Light on the Moth-Eye Corneal Nipple Array of Butterflies,* Proceedings of the Royal Society B, vol. 273 no. 1587, 661-667, (2006).

2. Wilson, S. J. and M. C. Hutley, *Optical Properties of 'Moth Eye' Antireflection Surfaces*, Journal of Modern Optics, 29:7, 993-1009, (1982).

3. Johnson K L, "Contact Mechanics", Cambridge University Press 1985.

4. Tau S, Yu-Long L, Kui X, Feng Z, Ke-Shi Z, Qiong D, "Experimental investigation on strain rate sensitivity of ultra-fine grained copper at elevated temperatures", submitted to Mech. of Matls. 2010.

FACULTY

THOMAS A. DOW

Director, Precision Engineering Center
Dean F. Duncan Distinguished University Professor in Mechanical Engineering
Professor, Department of Mechanical and Aerospace Engineering

BS, Mechanical Engineering, Virginia Polytechnical Institute, 1966
MS, Engineering Design, Case Institute of Technology, 1968
PhD, Mechanical Engineering, Northwestern University, 1972

After receiving his PhD degree from Northwestern University in 1972, Dr. Dow joined the Tribology Section of Battelle Columbus Laboratories and worked there for ten years. His research interests were in the areas of friction and wear and included studies on a wide variety of topics from lubrication of cold-rolling mills using oil-in-water emulsions to wet braking effectiveness of bicycle brakes to elastohydrodynamic lubricant film generation in ball and roller bearings. He developed experimental apparatuses, established analytical models, and corroborated those analyses with experimental measurements. Dr. Dow joined the faculty at North Carolina State University in 1982 and was instrumental in developing the academic and research program in precision engineering. His current research interests include the design of precision machining systems, real-time control, and metrology. He was one of the founders of the American Society for Precision Engineering and currently acts as the Executive Director.

JEFFREY W. EISCHEN

Associate Professor
Department of Mechanical and Aerospace Engineering

BS, Mechanical Engineering, UCLA, 1978
MS, Mechanical Engineering, Stanford University, 1981
PhD, Mechanical Engineering, Stanford University, 1986

Dr. Eischen has been with North Carolina State University since 1986 and his research areas of interest include: linear and nonlinear finite element analysis, multi-body kinematics/dynamics/control, fabric mechanics, and stress analysis in microelectronic devices. He teaches undergraduate courses in strength of mechanical components and mechanical design. His graduate courses include fracture mechanics and advanced machine design. He has collaborated with colleagues in the Precision Engineering Center for several years on computer simulation related projects dealing with precision shape control of disk drive read/write heads, stress and deformation analysis of high energy physics equipment, and contact lens mechanics.

RONALD O. SCATTERGOOD

Professor
Materials Science and Engineering Department

BS, Metallurgical Engineering, Lehigh University, 1961
MS, Metallurgy, Massachusetts Institute of Technology, 1963
PhD, Metallurgy, Massachusetts Institute of Technology, 1968

R.O. Scattergood is a Professor in the Department of Materials Science and Engineering. He received BS degrees in Mining Engineering and Metallurgical Engineering from Lehigh University. His MS and PhD degrees were obtained in Metallurgy from M.I.T. In 1968 he became a member of the basic research staff in the Materials Science Division at the Argonne National Laboratory. In 1981, he joined the faculty as a Professor of Materials Engineering at North Carolina State University.

Professor Scattergood's major research interests have been focused on the mechanical behavior of solids. He has worked in the areas of strengthening mechanisms in solids, mechanical testing, fracture, tribology, nanocrystaline materials and precision machining processes. He has published over 200 technical papers, books and reports.

STAFF

KENNETH P. GARRARD

Senior Research Associate
Precision Engineering Center

BS, Computer Science, North Carolina State University, 1979
MS, Computer Studies, North Carolina State University, 1983

As a full-time staff researcher at the Precision Engineering Center, Mr. Garrard's interests and duties have included the development of high performance control systems for ultra-precision machines and software development for custom, multiprocessor computer systems. He participated in the development of the original PEC fast tool servo as well as three other fast tool servo systems that have been delivered to commercial and government sponsors. One of these systems was built specifically for the on-axis turning of off-axis segments of conic surfaces of revolution and another is being used for the fabrication of inertial confinement fusion target mandrels. He has performed numerous prototype fabrication projects that required unique machine configurations and controller software. Mr. Garrard also has a long standing interest in the analysis of scientific data, programming language structures, sorting and searching algorithms, multiprocessor computer architecture and the design and implementation of hard real-time systems.

ALEXANDER SOHN

Research Assistant/Lecturer
Precision Engineering Center

B.S., Physics, University of Texas at Arlington, 1992
M.S., Physics, University of Texas at Arlington, 1994

Mr. Sohn joined the Precision Engineering Center in August, 1997 as a member of the technical staff. His current research interests range from machine design and metrology to the design and fabrication of nonimaging optics. Mr. Sohn's varied research activities began in microwave optics and atomic physics as a student at the University of Texas at Arlington and later progressed to precision machine design, design and fabrication of plastic optics as well as automation and machine vision at Fresnel Technologies, Inc. in Fort Worth, Texas.

MONICA RAMANATH

Administrative Assistant
Precision Engineering Center

BS, Accounting / North Carolina State University, 2001

Ms. Ramanath joined the PEC in September 2009. Previously, Ms. Ramanath worked as an Accounting Technician in the College of Education; book-keeper for 11 branches of the YMCA.

CONSULTANTS

KARL FALTER

Consulting Engineer

BS, Mechanical Engineering, North Carolina State University, 1987
MS, Mechanical Engineering, North Carolina State University, 1989
PhD, Mechanical Engineering, North Carolina State University, 1992

Prior to working as an independent consultant, Dr. Falter was a senior development engineer with Eastman Kodak from 1997 to 2003. He designed and developed electrical and control systems for custom precision machine tools. Dr. Falter also worked for Rank Pneumo from 1994 to 1997.

GRADUATE STUDENTS

BRANDON LANE joined the PEC in the June, 2008 after graduating with a B.S. in Mechanical Engineering from University of Nevada, Reno. In Reno, he gained engineering experience working as an intern for the Robotics R&D division of Hamilton Company, designing components and technical drawings for automated fluid handling workstations. He also worked as an undergraduate researcher for the UNR Nanocomposites lab where he researched fabrication techniques for carbon nanofiber and nanotube composites. These experiences in R&D sparked his interest in a career that continues higher levels of engineering learning and understanding. His schedule as a graduate student is supplemented by distance running, fishing, and mountain hiking in his free time.

ERIK ZDANOWICZ was raised in Hendersonville, NC. After receiving his BS in mechanical engineering from NCSU in May of 2007, Erik began his MSME degree and worked as a teaching assistant for Statics and Dynamics. Erik joined the PEC in January of 2008 as a research assistant for the redesign of the first generation Fast Long Range Actuator. Erik completed his MS degree in July of 2009 and went to work with Harris Corporation in Melbourne, FL. At Harris, Erik performed environmental analysis on the GOES-R weather satellite as well as quality engineering tasks for the Joint Strike Fighter (JSF F-35) team. Erik returned to the PEC in August of 2010 to pursue his PhD in ME and currently conducts research on nanocoining of optical features. He enjoys soccer, outdoors, robotics and programming microcontrollers.

GUILLAUME ROBICHAUD grew up in Alma, a small town in northern Québec, Canada. Guillaume received his engineering degree at École Polytechnique de Montréal in 2003 and joined GE as an engineer installing hydroelectric systems at locations around the world. In 2009, he began an MS at NC State where he designed, fabricated and tested an aerodynamic focusing device to improve signal in electrospray ionization for mass spectroscopy, in collaboration with Dr. Muddiman. Guillaume is now beginning a Ph.D. in Mech. Engr. with a minor in Chemistry.

ZACHARY MARSTON Zack is originally from Charlotte, NC. He received his BS in mechanical engineering from NCSU in December 2010. He began pursuing his MS degree and joined the PEC in January 2011. He gained product design/manufacture and CNC operation knowledge at GreenWave Scientific, Inc. in Raleigh through an internship. His research at the PEC involves the design of a compact package for aligning hemispherical parts on vacuum chucks. His interests include playing guitar, reading, biking, and kayaking.

GRADUATES OF THE PRECISION ENGINEERING CENTER

Student	Degree	Date	Company/Location
Jeffrey Abler	PhD	December 1994	Lexmark, Inc, Lexington, KY
William Allen	PhD	December 1994	North Carolina State Univ. Raleigh, NC
Kelly Allred	MS	June 1988	
Christopher Arcona	PhD	May 1993	Norton Worcester, MA
Bradford Austin	MS	June 2000	IBM Corporation Fishkill, NY
Markus Bauer	PhD	December 2001	QED, Inc, Rochester, NY
Tom Bifano	PhD	June 1988	Photonics Center, Boston University, Boston, MA
Scott Blackley	MS	May 1990	Motorola Austin, TX
Peter Blake	PhD	December 1988	NASA Goddard Greenbelt, MD
Dave Brehl	PhD	December 2008	Tessera North America Charlotte, NC
Brett Brocato	MS	June 2005	Tessera North America Charlotte, NC
Nathan Buescher	MS	May 2005	Consolidated Diesel Rocky Mount, NC
Mark Cagle	MS	June 1986	NASA-Langley Norfolk, VA

John Carroll	PhD	January 1986	Cummins Engine Co. Columbus, IN
Matthew Cerniway	MS	October 2001	Naval Surface Warfare Ctr West Bethesda, MD
Qunyi Chen	PhD	December 2009	
Damon Christenbury	MS	June 1985	Michelin Tire Co. Spartanburg, SC
Stuart Clayton	MS	May 2003	Naval Depot Cherry Point
James Cuttino	PhD	December 1994	UNC – Charlotte Charlotte, NC
Bob Day	PhD	July 1998	Los Alamos National Lab Los Alamos, NM
Joseph Drescher	PhD	May 1992	Pratt & Whitney East Hartford, CT
William Enloe	MS	December 1988	ITT Roanoke, VA
Karl Falter	MS	December 1989	Eastman Kodak Company Raleigh, NC
Peter Falter	PhD	May 1990	Lockheed-Martin Orlando, Florida
John Fasick	MS	May 1998	Kodak Rochester, NY
Steven Fawcett	PhD	June 1991	MicroE Natick, MA
Karalyn Folkert	MS	May 2005	Consolidated Diesel Rocky Mount, NC
Andre Fredette	PhD	May 1993	IBM Research Triangle Park, NC

Karl Freitag	MS	August 2004	Northrop Grumman Baltimore, MD
Stephen Furst	MS	December 2008	NCSU Raleigh, NC
David Gill	PhD	August 2002	Sandia National Laboratories Albuquerque, NM
Jim Gleeson	MS	June 1986	Battelle Columbus Labs Columbus, OH
Mary Smith Golding	MS	May 1990	Harris Corporation Melbourne, FL
David Grigg	PhD	August 1992	Zygo Corporation Middlefield, CT
Hector Gutierrez	PhD	October 1997	Florida Inst. Of Tech. Melbourne, FL.
Christian Haeuber	MS	December 1996	Harris Corporation Melbourne, FL
Simon Halbur	MS	December 2004	
Matias Heinrich	MS	July 2001	Vistakon Jacksonville, FL
Gary Hiatt	PhD	May 1992	Caterpillar Zebulon, NC
David Hood	MS	May 2003	
Peter Hubbel	MS	December 1991	Delco Electronics Kokomo, IN
Konrad Jarausch	PhD	December 1999	Intel Corporation San Jose, CA
Bradley Jared	PhD	December 1999	Sandia National Laboratories Albuquerque, NM

David Kametz	MS	August 2002	Naval Air Warfare Center Aircraft Division Patuxent River, MD
Jerry Kannel	PhD	June 1986	Battelle Columbus Labs Columbus, OH
Tim Kennedy	PhD	May 2008	US Patent and Trademark Office, Washington, DC
Byron Knight	MS	May 1990	US Air Force Washington, DC
Lucas Lamonds	MS	July 2008	Micron Technology Boise, ID
Mark Landy	MS	June 1986	Battelle Columbus Labs Columbus, OH
Brandon Lane	MS	August 2010	
Mike Loewenthal	MS	December 1988	SVG Norwalk, CT
Michael Long	PhD	June 2000	Eastman Kodak Rochester, NY
Bryan Love	MS	May 2001	Virginia Tech
Michael Hung-Tai Luh	MS	June 1989	Proctor and Gamble Cincinnati, OH
Dan Luttrell	MS	1987	Moore Tool, Inc New Britain, CT
Edward Marino	MS	September 1999	Pratt Whitney Hartford, CT
Edward Miller	MS	December 2000	General Electric Greenville, SC
Michele Miller	PhD	December 1994	Michigan Tech. University Houghton, MI

Paul Minor	MS	September 1998	Hartford, CT
Gary Mitchum	MS	June 1987	Harris Corporation Melbourne, FL
Charles Mooney	MS	December 1994	AIF – NC State University Raleigh, NC
Patrick Morrissey	MS	May 2003	
Larry Mosley	PhD	June 1987	Intel Corporation Chandler, AZ
Patrick Moyer	PhD	May 1993	UNC-Charlotte Charlotte, NC
Nobuhiko Negishi	MS	August 2003	
Ayodele Oyewole	MS	October 1997	Pratt and Whitney East Hartford, CT
Hakan Ozisik	PhD	December 1989	
Witoon Panusittikorn	PhD	December 2004	Fabrinet Kookot, Lumlookka Thailand
John Pellerin	MS	May 1990	Sematech Austin, TX
Travis Randall	MS	August 2004	MBA student NCSU
Ganesh Rao	MS	December 1994	Oak Ridge National Lab Oak Ridge, TN
John Richards	MS	September 1997	Intel Corporation San Jose, CA
Guillaume Robichaud	MS	2010	
Walter Rosenberger	MS	May 1993	The East Group Kinston, NC

Alex Ruxton	MS	December 1996	Pratt &Whitney Palm Beach, Florida
Anthony Santavy	MS	August 1996	Ford Dearborn, MI
Keith Sharp	PhD	May 1998	Morgan Crucible Dunn, NC
Gordon Shedd	PhD	March 1991	Corning , Inc Corning, NY
Wonbo Shim	PhD	May 2000	Seagate Inc. Oklahoma City, OK
Robert Skolnick	MS	September 1997	San Diego, CA
Denise Skroch	MS	May 1989	IBM Corporation Raleigh, NC
Elizabeth Smith	MS	April 1989	
Stanley Smith	PhD	May 1993	
Ronald Sparks	PhD	May 1991	Alcoa Corporation Pittsburg, PA
Brent Stancil	MS	December 1996	Harris Corporation Melbourne, FL
Gene Storz	MS	May 1994	
Anand Tanikella	PhD	August 1996	Norton Industrial Ceramics Northboro, MA
Donna Thaus	MS	May 1996	Northern Telecom Research Triangle Park, NC
John Thornton	MS	December 1993	Digital Instruments Santa Barbara, CA
Michael Tidwell	MS	December 1991	

John Tyner	MS	June 1995	Patuxent Naval Air Station Patuxent River, MD
Nadim Wanna	MS	December 2006	ExxonMobil Corporation Houston, TX
Robert Woodside	MS	December 2006	Harris Corporation Melbourne, FL
Tao Wu	PhD	December 2003	
Yanbo Yin	PhD	October 2007	
Erik Zdanowicz	MS	May 2009	

ACADEMIC PROGRAMS

Problems and limitations associated with precision manufacturing can originate in the machine, the process, or the material. In fact, most problems will probably be caused by a combination of these factors. Therefore, improvement of current processes and development of new manufacturing methods will require knowledge of a multi-disciplinary array of subjects. The educational goal of the Precision Engineering Center is to develop an academic program which will educate scientists and engineers in metrology, control, materials, and the manufacturing methods of precision engineering.

The graduate students involved in the Precision Engineering Center have an annual stipend as research assistants. They can take up to 3 classes each semester while spending about 20 hours per week on their research projects. These students also work in the Center full-time during the summer months.

The Precision Engineering Center began in 1982 with an emphasis on the mechanical engineering problems associated with precision engineering. As a result, the original academic program proposed was biased toward courses related to mechanical design and analysis. However, as the research program has developed, the need for complementary research in sensors, materials, and computers has become obvious. A graduate student capable of making valuable contributions in the computer area, for example, will require a significantly different academic program than in mechanical engineering. For this reason, the Center faculty has set a core curriculum and each student in the program is required to take at least 3 of these core courses. The remainder of the courses for the MS or the PhD degree are determined by the university or department requirements and the faculty committee of the student.

The required courses are:

- MAE   545 Metrology in Precision Manufacturing
- PY   516 Physical Optics
- MAT   700 Modern Concepts in Materials Science
- CSC (ECE)   714 Real Time Computer Systems

PhD DEGREE PROGRAM

The PhD program in Precision Engineering has been set up as a multi-disciplinary program, drawing upon courses throughout the University to provide background and expertise for the students. It should contain required courses to insure solid grounding in the fundamentals plus electives to prepare the student in his area of specialization. Because Precision Engineering is concerned with an integrated manufacturing process, students interested in computer control, materials, machine structure, and measurement and actuation systems are involved in the program. Student research projects include the wide variety of topics addressed in this report. Each student's thesis should have an experimental component because Precision Engineering is basically a hands-on technology.

MS DEGREE PROGRAM

The Master of Science degree will have a higher percentage of application courses than the PhD degree. The emphasis will be to develop the foundation for involvement in precision engineering research and development. A total of 30 credits, including 6 credits for the MS thesis, are required. The thesis, while less comprehensive than the PhD dissertation, will be directed at important problems in Precision Engineering. Typically, the MS program will take four semesters plus one summer.

UNDERGRADUATE PROGRAM

The undergraduate degree broadly prepares an engineering student for industrial activities ranging from product design and engineering sales to production implementation. Because a large share of engineers only have the BS degree, these will be the people who must implement the new technology developed in research programs like the Precision Engineering Center. Therefore, a way must be found to acquaint engineers at the BS level with the techniques, problems, and potential of precision manufacturing.

In most undergraduate degree programs only limited time is available for technical electives. However, these electives offer the student the opportunity to expand his knowledge in many different directions. Beginning graduate courses (such as metrology) can be used as undergraduate electives.

Undergraduate projects and summer employment have also been utilized to include undergraduate students into the research program of the Center. During the 1998-1999 academic year, four undergraduate students in Mechanical Engineering were involved various projects at the PEC.

STUDY PLANS

Study plans for several example students are given below both for the MS and the PhD degree. Because of the breadth of the field and the wide range of thesis topics, few if any study plans will be exactly the same. The plan will depend upon the student's background, his interests, his thesis topic, the department, and the chairman and members of his committee.

PhD PROGRAM IN MECHANICAL ENGINEERING

Major Courses:

*   MAE 740   Advanced Machine Design I
*   MAE 741   Advanced Machine Design II
*   MAE 706   Heat Transfer Theory & Applications
*   MAE 713   Principles of Structural Vibration
*   MAE 760   Computational Fluid Mechanics and Heat Transfer
*   MAE 545   Metrology in Precision Manufacturing
*   MAE 715   Nonlinear Vibrations
*   MAE 716   Random Vibration
*   MAE 714   Analytical Methods in Structural Vibration
*   MAE 742   Mechanical Design for Automated Assembly
*   MAE 895   Doctoral Dissertation Research

Minor Courses:

*   MA   511   Advanced Calculus I
*   MA   775   Mathematical Methods in the Physical Sciences I
*   CSC   780   Numerical Analysis II
*   PY   516   Physical Optics
*   ECE   716   System Control Engineering
*   MAT   700   Modern Concepts in Materials Science
*   ECE   726   Advanced Feedback Control
*   ECE   764   Digital Image Processing

PhD PROGRAM IN MATERIALS ENGINEERING

Major Courses:

- MAT   710   Elements of Crystallography and Diffraction
- MAT   700   Modern Concepts in Materials Science
- MAT   556   Composite Materials
- MAT   715   Transmission Electron Microscopy
- MAT   795   Defect Analysis/Advanced Materials Experiments
- MAT   753   Advanced Mechanical Properties of Materials
- MAT   712   Scanning Electron Microscopy
- MAT   895   Doctoral Dissertation Research

Minor Courses:

- PY   414   Electromagnetism I
- ST   502   Experimental Statistics for Engineers I
- MAE   740   Advanced Machine Design I
- MAE   741   Advanced Machine Design II
- MAE   545   Metrology in Precision Manufacturing
- PY   516   Physical Optics
- MA   401   Applied Differential Equations II

PhD PROGRAM IN ME (FOR STUDENT WITH MS DEGREE)

- ECE   716   System Control Engineering
- ECE   791   Gate Array Design
- MAT   700   Modern Concepts in Materials Science
- PY   516   Physical Optics
- MA   502   Advanced Mathematics for Engineers and Scientists II
- MA   775   Mathematical Methods in the Physical Sciences I
- MA   780   Numerical Analysis II
- MAE   732   Fundamentals of Metal Machining Theory
- MAE   740   Advanced Machine Design I
- MAE   741   Advanced Machine Design II

- MAE 545   Metrology in Precision Manufacturing
- MAE 716   Random Vibration

MS PROGRAM FOR ME STUDENT

- MAE 713   Principles of Structural Vibration
- MAE 740   Advanced Machine Design I
- MAE 545   Metrology in Precision Manufacturing
- MAT 700   Modern Concepts in Materials Science
- PY   516   Physical Optics
- MA   501   Advanced Math for Engineers and Scientists I
- MA   502   Advanced Math for Engineers and Scientists II
- MAE 695   Master's Thesis Research

MS PROGRAM FOR COMPUTER SCIENCE STUDENT

- CSC   501   Operating Systems Principles
- CSC   506   Architecture of Parallel Computers
- CSC   512   Compiler Construction
- ECE   521   Computer Design and Technology
- CSC   715   Concurrent Software Systems
- MAE 545   Metrology for Precision Manufacturing
- MAE 789   Digital Control Systems
- ECE   764   Digital Image Processing

MS PROGRAM FOR MATERIALS SCIENCE STUDENT

- MAT 700   Modern Concepts in Material Science
- MAT 710   Elements of Crystallography and Diffraction
- MAT 715   Transmission Electron Microscopy
- MAT 712   Scanning Electron Microscopy
- MAT 722   Advanced Scanning Electron Microscopy and Surface Analysis
- MAE 545   Metrology for Precision Manufacturing
- PY   516   Physical Optics
- ECE   738   IC Technology and Fabrication
- MAT 695   Master's Thesis Research

MS PROGRAM FOR PHYSICS STUDENT

- PY 516 Physical Optics
- PY 552 Introduction to Structure of Solids I
- PY 753 Introduction to Structure of Solids II
- PY 781 Quantum Mechanics I
- PY 782 Quantum Mechanics II
- PY 783 Advanced Classical Mechanics
- PY 785 Advanced Electricity and Magnetism I
- PY 786 Advanced Electricity and Magnetism II
- MAT 700 Modern Concepts in Material Science
- MAE 545 Metrology for Precision Manufacturing
- PY 695 Master's Thesis Research

SHORT COURSES AND TV COURSES

Six graduate level courses: Scanning Electron Microscopy (MAT 712), Advanced SEM Surface Analysis (MAT 722), Modern Concepts in Material Science (MAT 700), Mechanical Properties of Materials (MAT 705), and Metrology (MAE 545) have been offered as video courses nationwide via National Technological University. In a typical year, approximately 120 students from industry and national laboratories participate in these courses. Future plans call for a MS program in Precision Engineering to be offered via the television network.

TECHNICAL REPORTS

Volume 1 - 1983	December 1983	136 pages
Volume 2 - 1984	January 1985	168 pages
Volume 3 - 1985	January 1986	294 pages
Volume 4 - 1986	January 1987	255 pages
Volume 5 - 1987	December 1987	336 pages
Volume 6 - 1988	December 1988	362 pages
Volume 7 - 1989	March 1990	357 pages
Volume 8 - 1990	March 1991	385 pages
Volume 9 - 1991	March 1992	382 pages
Volume 10 - 1992	March 1993	289 pages
Volume 11 - 1993	March 1994	316 pages
Volume 12 - 1994	March 1995	268 pages
Volume 13 - 1995	January 1996	251 pages

Volume 14 - 1996	January 1997	232 pages
Volume 15 - 1997	January 1998	298 pages
Volume 16 – 1998	January 1999	258 pages
Volume 17 – 1999	January 2000	232 pages
Volume 18 – 2000	January 2001	274 pages
Volume 19 – 2001	January 2002	201 pages
Volume 20 – 2002	January 2003	328 pages
Volume 21 - 2003	January 2004	208 pages
Volume 22 – 2004	February 2005	207 pages
Volume 23 – 2005	February 2006	264 pages
Volume 24 – 2006	March 2007	274 pages
Volume 25 – 2007	March 2008	192 pages
Volume 26 – 2008	March 2009	209 pages
Volume 27 – 2009	March 2010	192 pages

PUBLICATIONS IN 2010

1. G. Robichaud, R. Dixon, A. Potturi, J. Edwards, A. Sohn, T. Dow, D. Muddiman, *Design, Fabrication and Testing of a High Precision Piezo-actuated Air Amplifier as an Ion Focusing Device in Mass Spectrometry.* Proceedings of the ASPE 2010 Annual Meeting, Atlanta, GA, Oct. 31 – Nov. 4, 2010.

2. K. Garrard, A. Sohn, *Integrated Prescan Optics for Laser Printers*. Proceedings of the ASPE 2010 Annual Meeting, Atlanta, GA, Oct. 31 – Nov. 4, 2010.

3. B. Lane, T. Dow, R. Scattergood, *Diamond Tool Wear Reduction Mechanisms in Elliptical Vibration Assisted Machining.* Proceedings of the ASPE 2010 Annual Meeting, Atlanta, GA, Oct. 31 – Nov. 4, 2010.

4. M. Shi, B. Lane, T. Dow, R. Scattergood, *Thermo-chemical Wear Study on Orthogonal Diamond Turning of Steel and Stainless Steel.* Proceedings of the ASPE 2010 Annual Meeting, Atlanta, GA, Oct. 31 – Nov. 4, 2010.